Quantum Photonics with Hexagonal Boron Nitride Quantum Emitters

by

Simon J. U. White

Under the supervision of

Assoc. Prof. Alexander Solntsev

A dissertation submitted in fulfillment
of the requirements for the degree of

Doctor of Philosophy

UNIVERSITY OF TECHNOLOGY SYDNEY
SCHOOL OF MATHEMATICAL AND PHYSICAL SCIENCES
NEW SOUTH WALES
AUSTRALIA

AUGUST, 2022

CERTIFICATE OF ORIGINAL AUTHORSHIP

I, Simon J. U. White, declare that this thesis is submitted in fulfilment of the requirements for the award of Doctor of Philosophy, in the School of Mathematical and Physical Sciences at the University of Technology Sydney.

This thesis is wholly my own work unless otherwise referenced or acknowledged. In addition, I certify that all information sources and literature used are indicated in the thesis.

This document has not been submitted for qualifications at any other academic institution.

This research is supported by the Australian Government Research Training Program.

Production Note:
Signature removed prior to publication.

February 21, 2023

Abstract

Controlling and manipulating individual quantum systems underpins the development of scalable quantum technologies. These new technologies enable more precise and sensitive metrology and have the potential to revolutionise computing, enabling functionality inconceivable using classical technologies. Hexagonal boron nitride (hBN) is emerging as an exceptional platform for applications in quantum photonics. Defects within hBN's two-dimensional crystalline lattice can form an atom-like two-level system, which when excited can only release one photon at a time. The quantum emission from defects in this material is promising as single photons are ideal candidates for information carriers, flying qubits, integral to the future of advanced quantum technologies. Furthermore, due to the interaction between these defects and their local environments, they can be excellent quantum sensors on an atomic scale.

The focus of this thesis is to control, manipulate, and study hBN quantum emitters to understand their applicability today and their potential in future quantum technologies. Beginning with a proof of principle demonstration of quantum random number generation, it is shown that the room temperature quantum emission from a single hBN defect can be coupled to an integrated photonic circuit. By measuring the collapse of a single photon at the output of the photonic circuit, we demonstrate a scalable architecture for quantum random number generation.

The next sections of the thesis uncover how these defects are applicable more broadly in future quantum technologies. Aware of the requirements for the ideal single photon emitter (SPE), we detail the cryogenic properties of hBN quantum emitters, specifically under resonant excitation. Using this technique, we study the control and manipulation of these emitters under optical and electrical fields, as well as quantify how the emitters couple to their environments. Here, it is shown that the emission from these defects can be significantly enhanced under a co-excitation regime, and the mechanism behind the increased photoluminescence is explained by studying the temporal photophysics of the defect. To further detail the interaction between hBN single photon emitters and their local environment we uncover the dominant broadening mechanisms using resonant photoluminescence excitation (PLE). It is found that hBN emitters suffer from spectral diffusion and, interestingly, suffer homogeneous broadening even at 5 K. Finally, we take advantage of the two-dimensional nature of hBN crystals and fabricate a >100 nm thick van der Waals heterostructure device. Using this device, we show that the photoluminescence from hBN emitters can be electrically modulated; the emission can be gated on and off, the brightness can be controlled, and the wavelength can be tuned. These findings demonstrate that hBN is an exceptional platform for developing photonic quantum technologies and further show that hBN quantum emitters have applications from advanced sensing to quantum communication and information processing.

Publications

THESIS WORKS

1. White, S.J.U., Yang, T., Dontschuk, N., Li, C., Xu, Z.Q., Kianinia, M., Stacey, A., Toth, M. and Aharonovich, I., 2022. Electrical control of quantum emitters in a Van der Waals heterostructure. Light: Science & Applications, 11(1), pp.1-9.[1]

2. White, S.J.U., Stewart, C., Solntsev, A.S., Li, C., Toth, M., Kianinia, M. and Aharonovich, I., 2021. Phonon dephasing and spectral diffusion of quantum emitters in hexagonal boron nitride. Optica, 8(9), pp.1153-1158.[2]

3. White, S.J.U., Duong, N.M.H., Solntsev, A.S., Kim, J.H., Kianinia, M. and Aharonovich, I., 2020. Optical repumping of resonantly excited quantum emitters in hexagonal boron nitride. Physical Review Applied, 14(4), p.044017.[3]

4. White, S.J.U., Klauck, F., Tran, T.T., Schmitt, N., Kianinia, M., Steinfurth, A., Heinrich, M., Toth, M., Szameit, A., Aharonovich, I. and Solntsev, A.S., 2020. Quantum random number generation using a hexagonal boron nitride single photon emitter. Journal of Optics, 23(1), p.01LT01.[4]

NON-THESIS AND CONTRIBUTED WORKS

5. White, S.J.U., Wang, K., Solntsev, A. S., Szameit, A., and Sukhorukov, A. A., 2022. Demonstration of Lossy Linear Transformations and Two-Photon Interference on a Photonic Chip (In preparation).

6. White, S.J.U., Aharonovich, I, and Solntsev, A. S., 2022. Anderson Localisation with Photons from a Single-Photon Emitter (In preparation).

7. Zhigulin, I., Horder, J., Ivady, V., White, S.J.U., Gale, A., Li, C., Lobo, C.J., Toth, M., Aharonovich, I. and Kianinia, M., 2022. Stark effect of quantum blue emitters in hBN. arXiv preprint arXiv:2208.00600.[5]

8. Horder, J., White, S.J.U., Gale, A., Li, C., Watanabe, K., Taniguchi, T., Kianinia, M., Aharonovich, I. and Toth, M., 2022. Coherence properties of electron beam activated emitters in hexagonal boron nitride under resonant excitation. Physical Review Applied, 18(6), 064021.[6]

9. Chen, Y. White, S.J.U., Ekimov, E. A., Bracdac, C., Toth, M, Aharonovich, I, and Tran, T. T., 2022. Ultralow-power cryogenic thermometry based on optical-transition broadening of a two-level system in diamond. ACS Photonics. (Just accepted 2023).

10. Tran, T.N., Kim, S., White, S.J.U., Nguyen, M.A.P., Xiao, L., Strauf, S., Yang, T., Aharonovich, I. and Xu, Z.Q., 2021. Enhanced Emission from Interlayer Excitons Coupled to Plasmonic Gap Cavities. Small, 17(45), p.2103994.[7]

11. Chen, Y., Westerhausen, M.T., Li, C., White, S.J.U., Bradac, C., Bendavid, A., Toth, M., Aharonovich, I. and Tran, T.T., 2021. Solvent-Exfoliated Hexagonal Boron Nitride Nanoflakes for Quantum Emitters. ACS Applied Nano Materials, 4(10), pp.10449-10457.[8]

12. Chen, Y., Li, C., White, S.J.U., Nonahal, M., Xu, Z.Q., Watanabe, K., Taniguchi, T., Toth, M., Tran, T.T. and Aharonovich, I., 2021. Generation of High-Density Quantum Emitters in High-Quality, Exfoliated Hexagonal Boron Nitride. ACS Applied Materials & Interfaces, 13(39), pp.47283-47292.[9]

13. Nonahal, M., White, S.J.U., Regan, B., Li, C., Trycz, A., Kim, S., Aharonovich, I. and Kianinia, M., 2021. Bottom-Up Synthesis of Single Crystal Diamond Pyramids Containing Germanium Vacancy Centers. Advanced Quantum Technologies, 4(7), p.2100037.[10]

14. Damaso, N.J., White, S.J.U., and Kim, S., 2021. Analysis of anapole resonators in low index materials. Journal of Optics, 23(3), p.034003.[11]

15. Bernhardt, N., Kim, S., Fröch, J.E., White, S.J.U., Duong, N.M.H., He, Z., Chen, B., Liu, J., Aharonovich, I. and Solntsev, A.S., 2021. Large few-layer hexagonal boron nitride flakes for nonlinear optics. Optics Letters, 46(3), pp.564-567.[12]

16. Kianinia, M., White, S.J.U., Fröch, J.E., Bradac, C. and Aharonovich, I., 2020. Generation of spin defects in hexagonal boron nitride. ACS photonics, 7(8), pp.2147-2152.[13]

17. Bernhardt, N., Koshelev, K., White, S.J.U., Meng, K.W.C., Froch, J.E., Kim, S., Tran, T.T., Choi, D.Y., Kivshar, Y. and Solntsev, A.S., 2020. Quasi-BIC resonant enhancement of second-harmonic generation in WS2 monolayers. Nano Letters, 20(7), pp.5309-5314.[14]

Conference Proceedings

1. White, S.J.U., Wang, K., Szameit, A., Sukhorukov, A.A. and Solntsev, A.S., 2021, June. Demonstration of Lossy Linear Transformations and Two-Photon Interference via Singular Value Decomposition. In European Quantum Electronics Conference (p. ea_7_3). Optical Society of America.

2. Kianinia, M., White, S.J.U., Fröch, J.E., Bradac, C. and Aharonovich, I., 2021, May. Engineering of Room Temperature Spin Defects in Hexagonal Boron Nitride. In 2021 Conference on Lasers and Electro-Optics (CLEO) (pp. 1-2). IEEE.

3. White, S.J.U., Duong, N.M.H., Solntsev, A.S., Kim, J.H., Kianinia, M. and Aharonovich, I., 2021, May. Coherent Excitation of Hexagonal Boron Nitride Single Photon Emitters via Optical Repumping. In CLEO: QELS_Fundamental Science (pp. FW4I-7). Optical Society of America.

4. Bernhardt, N., Koshelev, K., White, S.J.U., Meng, K.W.C., Fröch, J.E., Kim, S., Tran, T.T., Choi, D.Y., Kivshar, Y. and Solntsev, A.S., 2020, August. Observation of Extraordinary SHG from WS2 Monolayers Boosted by Optical Bound States in the Continuum. In Conference on Lasers and Electro-Optics/Pacific Rim (p. C7B_1). Optical Society of America.

5. White, S.J.U., Klauck, F., Schmitt, N., Tran, T.T., Kianinia, M., Steinfurth, A., Aharonovich, I., Szameit, A. and Solntsev, A.S., 2019, December. Quantum random number generation using a solid state single photon source. In AOS Australian Conference on Optical Fibre Technology

(ACOFT) and Australian Conference on Optics, Lasers, and Spectroscopy (ACOLS) 2019 (Vol. 11200, pp. 67-68). SPIE.

6. White, S.J.U., Wang, K., Tran, T.T., Kianinia, M., Titchener, J., Gräfe, M., Fischbach, S., Rodt, S., Song, J.D., Reitzenstein, S. and Aharonovich, I., 2019, June. Tomography of quantum dots in a non-hermitian photonic chip. In European Quantum Electronics Conference (p. eb_p_6). Optical Society of America.

Contents

Listing of figures

Acknowledgments

The work of this thesis is the culmination of many stimulating discussions, broad scientific collaboration, great support, and an uncomfortable amount of hours spent in a cold dark room.

I want to thank my supervisor A/Prof. Alexander Solntsev for his unwavering support, enthusiasm, and freedom to explore. Our discussions had me appreciating your ardour and kindness, and always rejuvenated my passion for research. I would also like to thank Prof. Igor Aharonovich and Prof. Milos Toth for the opportunity to be a part of such an inclusive group working in such an exciting field.

I want to thank my co-supervisors who have guided me throughout my post-graduate studies, in particular, Mehran Kianina for always having time to discuss projects, advising me experimentally, and reluctantly enduring my endless barrage of questions. Toan Trong Tran, thanks for always helping me to consider the deeper phenomena and helping me navigate research more broadly.

I want to thank all my collaborators, including but not limited to Rike, Nora, Andrea, Dr Heinrich, Prof. Szameit and the rest of the team at the University of Rostock; Dr Nikolai Dontschuk and Dr Alastair Stacey at Melbourne University and RMIT University; Dr Kai Wang and Prof. Andrey Sukhorukov at Stanford and the Australian National University; and A/Prof Je-Hyung Kim at UNIST.

A huge thanks must be made to all my fellow students at UTS. In particular thanks to Caleb Estherby and Minh Nguyen for the moral support and productive lunches. Huge thanks to Jake for reviewing this text; I wish you all the best in taking over my lab! And a special thanks to Chi, Teishan, Yongliang, Vanya, Lesley, Ritika, Milad, Thinh, Helen, Hanh, Connor, Blake, Mika, Noah, Johannes, John, Seejeong, Zaiquan and Carlo; the experience of working together has been a pleasure, and I hope such a supportive group continues to prosper.

I want to thank my parents and family for always looking out for me. Fiona and David, you have always encouraged my sibling and I; this achievement is a reflection of your own character and success.

And finally, I wholeheartedly want to thank my partner in life, Elise. A good friend once advised that "I shan't let go of that kite". I couldn't agree more and realise I am very lucky to have met you. I hope we always continue to find joy and happiness together. Cheers to our next adventure!

"Jedenfalls bin ich überzeugt, daß der nicht würfelt."

I, at any rate, am convinced that He (god) does not throw dice.

Einstein to Bohr, 1926

0

Introduction

0.1 Preamble

The pursuit of understanding is a desire rooted in human inquiry. As time progresses, the generation of knowledge quickly outpaces one's ability to gain complete universal understanding and instead we look to simplify problems such that solutions become conceivable. This simplification is integral to the scientific method, and many thought the accumulation of scientific knowledge would yield all nature's secrets, but in the late 19th / early 20th century our fundamental understanding of the nature of reality was being questioned. The concept that the electric field exists in quantised energy levels was first introduced by Plank in 1900.[15] This theory was used to explain black body radiation and states that the energy radiating from atomic systems is separated into discrete energy levels, with energy E proportional to the product of the frequency ν of emitted quanta of light and a constant h (Planks constant):

$$E = h\nu \tag{1}$$

This theory was used by Einstein who postulated light was indeed made of individual quantum particles and used this quantisation to explain the photoelectric effect in 1905.[16,17] In 1923 Compton also postulated light must be made of quantised particles to explain the energy loss of low-intensity X-rays due to scattering off an electron.[18] The term to describe this quantised packet of the electric field is the now ubiquitous "photon", introduced by Lewis in 1926.[19] Meanwhile in the mid-1920s de Broglie considered how matter also has a wavelike nature, equating wavelength λ and momentum p with $\lambda = h/p$.[20] Around the same time Schrödinger derived the wave-equation used to govern quantum mechanical systems,[21], and Heisenberg introduced the complementarity between energy E and time t such that their combined uncertainty is always greater than or equal to Planks constant $\Delta E \Delta t \geq h$.[22] Soon after in 1927 the complete formal quantisation of the electric field was presented by Dirac.[23,24]

It is safe to say that this period was one of the most exciting periods of academic discovery and our understanding of quantum phenomena has had profound consequences across all disciplines and for the nature of reality itself. The interpretation of these quantum phenomena, i.e. what is meant by the nature of wave-particle duality, the probabilistic behaviour of wavefunction collapse, and the concept of quantum entanglement, are still matters of debate throughout the physics community. It is thought Einstein himself also wrangled with accepting quantum mechanics and wrote in a letter between him and Max Born;

> *Die Quantenmechanik ist sehr achtung-gebietend. Aber eine innere Stimme sagt mir, daß das doch nicht der wahre Jakob ist. Die Theorie liefert viel, aber dem Geheimnis des Alten bringt sie uns kaum näher. Jedenfalls bin ich überzeugt, daß der nicht würfelt.*
>
> Albert Einstein, 1926

> *Quantum mechanics is certainly imposing. But an inner voice tells me that it is not yet the real thing. The theory says a lot, but does not really bring us any closer to the secret of the "old one." I, at any rate, am convinced that He does not throw dice.*
>
> God does not throw dice.

Regardless of the interpretations, these discoveries formed the foundation for much of the quantum research undertaken today. This period was the birthplace of all quantum technologies, including the fields of quantum information processing (QIP), quantum communication, and quantum metrology. Here instead of relying on the determinism provided by classical information processing, it has been shown it is possible to secure advantages in all of these fields using quantum mechanics. The difficulty in realising these technologies, for the most part, originates from the fragility of quantum systems. To get down to the level where these quantum effects dominate the use of large complex apparatus is often required. Thus there is a large amount of research invested into understanding new materials which may enable applications in quantum technologies.

Herein lies the topics of this thesis. Defects in the Van der Waals material hexagonal boron nitride (hBN) have recently been shown to host quantum emitters, i.e. the defects can be used as sources of single photons. These single photons can be manipulated to store and transmit quantum information, opening a host of possible quantum applications discussed further below. Furthermore, the defects themselves exist in a near-two-dimensional (2D) material, thus they can be exceptionally sensitive to their local environment. This also opens a host of applications for sensing and metrology. As these defects are only recently discovered much is still unknown about how they interact with their environment, and demonstration of how these sources may be used is also limited.

0.2 STRUCTURE

This thesis is structured as the following.

In this chapter (Chapter 0) I begin with a background in applications allowed by quantum technologies, specifically related to those enabled through quantum photonics. I introduce the concept of the single-photon source and outline how it may be used to carry quantum information. I then introduce the material studied throughout the thesis, hexagonal boron nitride, as well as some of the characterisation techniques used to gain further information about hBN defects.

In Chapter 1, I show an application for hBN single-photon emitters by demonstrating quantum random number generation. This is achieved by coupling the emission from an hBN defect to an integrated photonic circuit and measuring the position of single photons in a superposition of multiple waveguides. This chapter is based on my own peer-reviewed literature, and much of the content is copied verbatim from *"Quantum random number generation using a hexagonal boron nitride single-photon emitter"*, **White, S.J.U.,** Klauck, F., Tran, T.T., Schmitt, N., Kianinia, M., Steinfurth, A., Heinrich, M., Toth, M., Szameit, A., Aharonovich, I. and Solntsev, A.S., 2020. Journal of Optics, 23(1), p.01LT01.[4]

Up to here, I have only commented on the behaviour of hBN emitters at room temperature. As discussed further below, the majority of quantum applications for single-photon emitters require that the emitted photons are indistinguishable. This is a major challenge for hBN, and the following chapters document my work toward understanding the emission from hBN defects, quantifying how these emitters couple to their environments, and presenting how one may modulate their environment to enhance quantum emission, all with a global goal of working towards coherent emission from hBN.

In chapter 2, I introduce resonant excitation of hBN emitters and show how a co-excitation scheme can enhance the photoluminescence from the emitters. This chapter is based on my own peer-reviewed literature, and much of the content is copied verbatim from *"Optical repumping of resonantly excited quantum emitters in hexagonal boron nitride."* **White, S.J.U.,** Duong, N.M.H., Solntsev, A.S., Kim, J.H., Kianinia, M. and Aharonovich, I., 2020. Physical Review Applied, 14(4), p.044017.[3]

Chapter 3 deals explicitly with the coupling of hBN defects to their native local environments. I quantify the broadening mechanisms dominant in the emission of hBN, in particular, those due to heat and local field fluctuations (spectral diffusion). This chapter is based on my own peer-reviewed literature, and much of the content is copied verbatim from *"Phonon dephasing and spectral diffusion of quantum emitters in hexagonal boron nitride."* **White, S.J.U.,** Stewart, C., Solntsev, A.S., Li, C., Toth, M., Kianinia, M. and Aharonovich, I., 2021. Optica, 8(9), pp.1153-1158.[2]

In chapter 4 I present a way to modulate the environment of hBN emitters and show the majority of emitters in hBN flakes are not active without a DC electric field. I show how we can use an applied field to electrically modulate the emission and develop a heuristic model to explain the mechanisms behind the emitter activation. This chapter is based on my own peer-reviewed literature, and much of the content is copied verbatim from *"Electrical control of quantum emitters in a Van der Waals heterostructure."* **White, S.J.U.,** Yang, T., Dontschuk, N., Li, C., Xu, Z.Q., Kianinia, M., Stacey, A., Toth, M. and Aharonovich, I., 2022. Light: Science & Applications, 11(1), pp.1-9.[1]

Finally, in chapter 5 I conclude my findings and comment on future works that may grant hBN single-photon emitters access to applications in a plethora of quantum technologies.

0.3 Quantum Technologies

The vast majority of technologies today are founded upon the principle that information should be stored as a bit. That is, information is stored in the binary state of a transistor and is either represented by 0 or 1. Over the last 40 years, this idea has been challenged, and it has been proposed significant advantages may be gained by making use of the quantum mechanical framework that underpins our understanding of the natural world.[25,26] These alternative quantum technologies make use of the principles of superposition and entanglement to realise a fundamental performance advantage over classical technologies. Superposition is used to describe the concept that the complete state of a quantum particle $|\Upsilon\rangle$ must be represented as a linear combination of two states:

$$|\Upsilon\rangle = \alpha|0\rangle + \beta|1\rangle \tag{2}$$

Where α and β are complex probability amplitudes, $|\alpha|^2$ is probability of $|\psi\rangle = |0\rangle$ and $|\alpha|^2 + |\beta|^2 = 1$. Entanglement is used to describe the phenomena where the quantum state of one quantum particle becomes correlated with the state of one, or more, other quantum particles. To fully describe the state of this *entangled* particles we must describe the state of each particle with reference to the other. Consider we have two particles a and b that can each exist in states $|0\rangle$ and $|1\rangle$. If these particles become entangled their combined state can be described as;

$$|\Upsilon_{a,b}\rangle = \frac{1}{\sqrt{2}}\left(|0_a, 0_b\rangle + |1_a, 1_b\rangle\right) \tag{3}$$

with a positive correlation, or;

$$|\Upsilon_{a,b}\rangle = \frac{1}{\sqrt{2}}\left(|0_a, 1_b\rangle + |1_a, 0_b\rangle\right) \tag{4}$$

for a negative correlation. For example, for the entangles particles with a negative correlation, for a measurement of particle giving $|\Upsilon_a\rangle = |0\rangle$ we know, with certainty, particle b will exist in the state $|\Upsilon_b\rangle = |1\rangle$. The entanglement state between two particles is sometimes referred to as a Bell state and was the focal point of much discussion in the mid-20th century, including Schrodingers famed cat paradox.[27,28,29,30,31]

Quantum technologies have many potential and some already realised advantages in three main areas:

1. Quantum Communication

2. Quantum Metrology and Sensing

3. Quantum Information Processing (QIP)

0.3.1 Quantum Communication

Quantum communication entails the transmission of a quantum state between two parties.[32] Conventionally these two parties are given the names Alice and Bob, and often we also consider the information gained by an eavesdropper, Eve. Quantum key distribution (QKD) uses superposition, entanglement, and the no-cloning theorem, which simply states one cannot clone an unknown quantum state, to enable fundamentally secure communication.[33,34,32] Further from QKD there is interest in distributed quantum networks that would have the ability to connect quantum nodes.[35,36] Photons are the dominant quantum information carrier due to their weak interaction with their environment and the speed at which they can be transmitted, thus huge research interest is in place on photon sources that will enable these technologies.[37,38,39]

0.3.2 Quantum Metrology and Sensing

Quantum metrology refers to a field where the measurement or discrimination of an unknown quantity is enhanced through the use of quantum phenomena.[40,41] The measurement of an unknown parameter is always susceptible to some uncertainty, conventionally given as the standard deviation $\Delta\sigma$. We perform n multiple measurements to reduce this uncertainty but classically this uncertainty scales with $\Delta\sigma/\sqrt{n}$. This $n^{-1/2}$ scaling is referred to as the standard quantum limit (SQL). It is possible to beat the SQL and increase that scaling to n^{-1}, approaching the Heisenburg limit, by entangling the measurements and read-out probes before a measurement.[42,43,44] One incredibly successful example of this technology is that used in the Laser Interferometer Gravitational-Wave Observatory (LIGO). To enhance the sensitivity further than possible due to classical limitations at LIGO they make use of squeezed quantum states, which allow them to decrease uncertainty in one parameter whilst increasing the uncertainty in another. Though out of the scope of this thesis, such squeezed states of light drive a huge amount of research interest.[45,46]) Furthermore, the ability to beat the standard quantum limit with entangled photon states (known as a NOON state) has also been proposed and may be one of the first promising applications for the entanglement of single photons from hexagonal boron nitride (introduced below).[47,48]

The other side of this field is described by those relating to quantum sensing. Here I refer to the use of point defects in solid-state crystals that can be influenced by their environments. Two such examples are seen with the nitrogen-vacancy in diamond and the negatively charge boron vacancy in hexagonal boron nitride, which can be used as nanoscale sensors by monitoring the spin state of an electron.[49,50,51,52,53]

0.3.3 Quantum Information Processing (Quantum Computing)

Finally, and arguably most significantly, is the field of Quantum Information Processing (QIP).[54,55] Simply put, QIP is the alternative computational architecture that is based on entanglement and superposition, as opposed to binary units (bits). Although not universally advantageous,[56] it has been shown that some computational problems unfeasible with classical computing due to time/hardware scaling constraints can remain feasible with a quantum architecture.[57,58] The most well-known application for a universal quantum computer is a factoring algorithm developed by Peter Shor in 1999.[59,60] Most classical security and cryptography schemes are based on the factoring of prime numbers; Shor showed that QIP can provide an exponential speed-up for factoring the products of primes, giving QIP the ability to break cryptographic keys. Although a universal quantum computer is still decades away, there have already been a number of demonstrations of compiled versions of Shor's algorithm which aim to determine the prime factors of a predefined number.[61,62,63] There is significant progress toward realising a universal quantum computer, but so far research in the field is still distributed among a number of competing architectures, including superconducting quantum interference devices, atomic qubits, and photonic qubits, and again the only long-distance interconnect between any of these architectures is based on photonic qubits.[64] Thus photonic quantum information processing remains a huge topic of research interest.[38,65,37]

0.4 Single-Photon Sources

Having introduced photons withing within the broad umbrella of quantum technologies, this section introduces light as an optical wave and the concept of frequency distribution, with respect to Maxwell's equations. Next, I introduce what is meant by a single-photon source, how this differs from other light sources, and how to measure this difference. I then introduce defects in hexagonal boron nitride (hBN) as a source of single photons.

0.4.1 The Electromagnetic field: Maxwell's Equations

The classical formulation by James Clerk Maxwell that electric and magnetic fields are actually different manifestations of the same phenomenon was the second ”great unification” in physics and the understanding of the universe. Maxwell's equations are fundamental, and it is from this description of light, as a perturbation of electromagnetism fields, that much of physics today operates upon. This section will introduce a description of light as a wave which also forms the foundation for much of the analysis throughout this thesis and is based on the Mark Fox textbook ”Quantum Optics: An Introduction”.[66]

The equations Maxwell used to describe the electromagnetic response of a medium are given by:

$$\nabla \cdot \mathbf{D} = \rho \tag{5}$$

$$\nabla \cdot \mathbf{B} = 0 \tag{6}$$

$$\nabla \times \mathbf{E} = -\frac{\partial \mathbf{B}}{\partial t} \tag{7}$$

$$\nabla \times \mathbf{H} = \mathbf{j} + \frac{\partial \mathbf{D}}{\partial t} \tag{8}$$

where ρ, and j, are free charge, and current density, respectively. The electric and magnetic fields are given by **E** and **B**, and can be related to **D** and **H** by;

$$\mathbf{D} = \varepsilon_0 \varepsilon_r \mathbf{E} \tag{9}$$

$$\mathbf{B} = \mu_0 \mu_r \mathbf{H} \tag{10}$$

where ε_0 is the electric permittivity of free space, ε_r is the relative permittivity of the medium, μ_0 is the magnetic permeability of the vacuum, and μ_r is the relative permittivity of the medium (for free space usually assumed to be 1).

ELECTROMAGNETIC WAVES

The concept of electromagnetic waves can be easily established as a solution from these equations. We begin with eqn: 8 in terms of **E** and **B** with no free charges ($\rho = 0$) or currents ($\mathbf{j} = 0$), giving:

$$\nabla \times \mathbf{B} = \mu_0 \varepsilon_0 \varepsilon_r \frac{\partial \mathbf{E}}{\partial t} \tag{11}$$

Using the curl of equation 7, we find:

$$\nabla \times \nabla \times \mathbf{E} = -\nabla \times \frac{\partial \mathbf{B}}{\partial t} \tag{12}$$

and by using the vector identity:

$$\nabla \times (\nabla \times \mathbf{E}) = \nabla(\nabla \cdot \mathbf{E}) - \nabla^2 \mathbf{E} \tag{13}$$

we find:

$$\nabla(\nabla \cdot \mathbf{E}) - \nabla^2 \mathbf{E} = -\nabla \times \frac{\partial \mathbf{B}}{\partial t} \tag{14}$$

We then substitute this into eqn: 11, noting $\nabla \cdot \mathbf{E} = 0$, and finally obtain:

$$\nabla^2 \mathbf{E} = \mu_0 \varepsilon_0 \varepsilon_r \frac{\partial \mathbf{E}}{\partial t} \tag{15}$$

This equation describes an electromagnetic field propagating in an arbitrary direction with speed v.

$$\frac{1}{v^2} = \mu_0 \varepsilon_0 \varepsilon_r \tag{16}$$

And in free space where $\varepsilon_r = 1$, we find v describes the speed of light c:

$$c = \frac{1}{\sqrt{\mu_0 \varepsilon_0}} = 2.998 \times 10^8 \text{ m s}^{-1} \tag{17}$$

Of course, this is not always the case, and in a dielectric medium the speed of the wave is given by the ratio with respect to the mediums refractive index n:

$$v = \frac{c}{\sqrt{\varepsilon_r}} \equiv \frac{c}{n} \tag{18}$$

In general, it is most useful to consider the solution to Maxwell's equations in an arbitrary frame such that a wave of angular frequency ω propagates only along the z-direction. The electric and magnetic fields are orthogonal to one another, with the electric field amplitude only along the x-axis, i.e. polarised along x, the magnetic field will oscillate along y. In this case, the amplitude of the electric $E_y = E_y = 0$ and magnetic fields $B_x = E_z = 0$, such that eqns: 7 and 11 reduce to:

$$\begin{aligned} \frac{\partial E_x}{\partial z} &= -\frac{\partial B_y}{\partial t} && (19) \\ -\frac{\partial B_y}{\partial z} &= \mu_0 \varepsilon_0 \varepsilon_r \frac{\partial E_x}{\partial t} && (20) \end{aligned}$$

Which have solutions:

$$\begin{aligned} E_x(z,t) &= E_{x0}\, cos(kz - \omega t + \varphi) &= E_{x0}\, e^{i(kz-\omega t+\varphi)} && (21) \\ B_y(z,t) &= B_{y0}\, cos(kz - \omega t + \varphi) &= B_{y0}\, e^{i(kz-\omega t+\varphi)} && (22) \end{aligned}$$

Where φ is the optical phase shift, and k is the wavevector, which is related to the angular frequency ω and the optical wavelength λ by:

$$k = \frac{2\pi}{\lambda} = \frac{\omega}{v} = \frac{n\omega}{c} \tag{23}$$

INTERFERENCE

The next important concept to introduce is that of interference between optical waves. This is most simply observed through a Michelson interferometer, where a monochromatic wave, in one spatial mode, is split and then re-combined using a beamsplitter (Figure 1(a)). On the output path of the interferometer, the intensity of the wave is monitored, and oscillations between constructive or destructive interference are observed, based on the path length difference of the interferometer. This can simply be computed using:

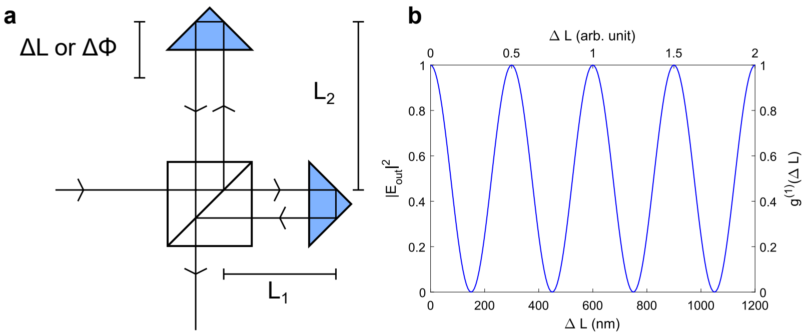

Figure 1: (a) Schematic for a Michelson interferometer. With cube 50:50 beamsplitter and retro-reflectors. (b) Interference for a monochromatic wave.

$$E_{out} = E_1 + E_2 = \frac{1}{2}E_0 e^{i2kL_1} + \frac{1}{2}E_0 e^{i2kL_2} \tag{24}$$

$$= \frac{1}{2}E_0 e^{i2kL_1}(1 + \frac{1}{2}E_0 e^{i2k\Delta L}) \tag{25}$$

Which when plot with respect to ΔL has maxima and minima at $\Delta L = \frac{m\lambda}{2}$ and $\Delta L = \frac{(2m+1)\lambda}{2}$, where m is an integer, as seen in Figure 1(b).

Coherence

Until this point, we have only considered a monochromatic wave, i.e. $\Delta\omega = 0$. For an exceptionally narrow laser, such as a Ti:Sapphire cavity laser with a linewidth $\sim$ 50 kHz, this effectively is the case and can be treated as such for aligning and calibrating such an interferometer in the lab. This assumption breaks down when considering exceptionally large interferometers, such as those found in LIGO (the Laser Interferometer Gravitational-Wave Observatory) whose arm lengths span kilometres, which, instead, make use of quantum metrology to enhance sensitivity, as discussed above (0.3.2).[45,46]

The conventional way to quantify the spectral stability of an optical wave is to calculate the length the wave will interfere with itself. This length is known as the coherence length L_c and is analogous to the coherence time τ_c, through the relation $L_c = c\tau_c$. Experimental determination of the coherence length is performed using a Michelson interferometer (Fig: 1(a)) to measure the first-order correlation function $g^{(1)}(\tau)$, given by:

$$g^{(1)}(\tau) = \frac{\langle E^*(t)E(t+\tau)\rangle}{\langle |E(t)|^2\rangle} \tag{26}$$

Where τ is the delay time induced via one arm ($\tau = \frac{\Delta L}{c}$), and $\langle ... \rangle$ refers to the integral over a large time. When passing a monochromatic wave of frequency ω_0 (given by $E(t) = E_0 e^{(-i\omega_0 t)} e^{(-i\varphi(t))}$) through the Michelson interferometer (eqn. 26) we find:

$$g^{(1)}(\tau) = e^{-i\omega_0 t} \langle e^{-i\,[\varphi(t+\tau)-\varphi(t)]} \rangle \tag{27}$$

Thus the first-order correlation for a wave with a delta distribution shows a sinusoidal oscillation without any damping, as shown above in Fig. 1(b). This of course assumes there is no dephasing of the wave, i.e. we only see the oscillations when $\varphi(t+\tau) = \varphi(t)$. As τ approaches τ_c the amplitude of these oscillations reduce and as $\tau >> \tau_c$ the first-order correlation drops to $\left|g^{(1)}(\tau)\right| \to 0$.

This effect is analogous to the effect seen for a wave packet with a distribution of angular frequencies $\Delta\omega$. Consider a Gaussian pulse of the electromagnetic field as shown in Figure 2(a). This pulse is defined such that it has centre frequency $\omega = 2\pi c/600\ nm$, coherence length of 5 optical periods $\tau_c = \lambda/c = 10 fs$ and thus full-width at half-maximum (FWHM) $\Delta\omega = \sqrt{8\pi \log 2}/\tau_c$. Simply by taking the fast Fourier transform (FFT) and converting the frequency axis to units of nm, we can observe such a pulse is actually just the sum over a broad distribution of wavelengths, in this case, $\Delta\lambda \sim 80\ nm$ (Fig. 2(b)). The idea that a single photon can exist as the sum over a number of frequencies is integral to understanding their behaviour in interferometric experiments and is fundamental to all quantum interference experiments. To study the frequency distribution of such a pulse, we can simply pass this wave through the Michelson interferometer as described above, and we will observe intensity fluctuations given by:

$$g^{(1)}(\tau) = e^{-i\omega_0 t} \exp\left\{-\frac{\pi}{2}\left(\frac{\tau}{\tau_c}\right)^2\right\} \tag{28}$$

as shown in Figure 2(c). Due to the Gaussian intensity distribution of the pulse in time, we note the frequency distribution and the first-order correlation distributions also follow a Gaussian line shape.

The next most common distribution of a photon envelope in time is given by an exponential decay. Figure 3(a) shows the magnitude of the electric field decaying with lifetime of $\tau_c = 1/\Delta\omega = 1/(2\pi\Delta v) =$

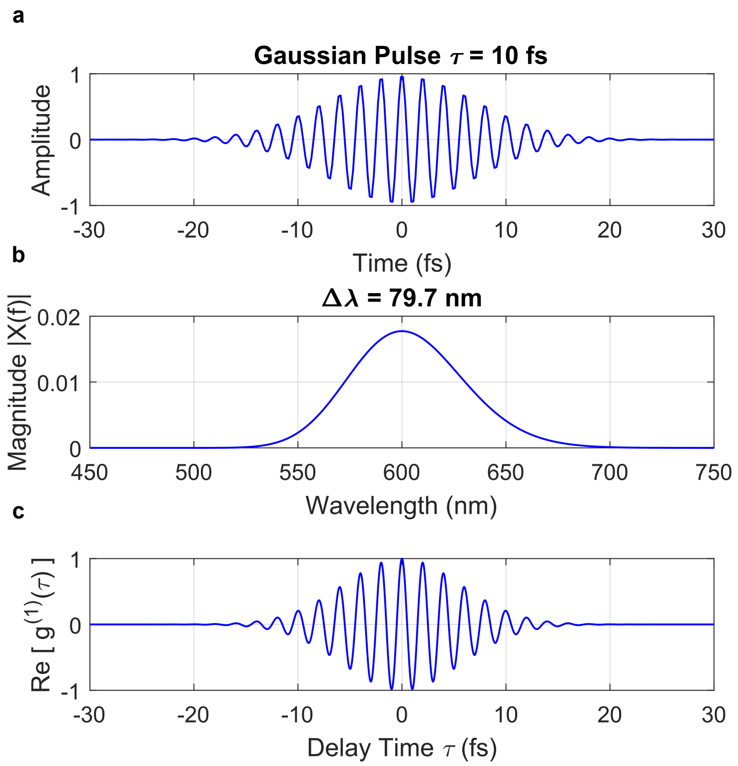

Figure 2: Interference with a Gaussian Pulse (a) Oscillation of the electric field for a Gaussian pulse with width $\sigma = 10$ fs at 600 nm. (b) The fast Fourier transform is used to show the pulse's frequency distribution, which is then converted to show wavelength distribution in nm. The pulse has $\Delta\lambda \sim 80nm$ (c) First-order correlation $g^{(1)}(\tau)$ displays interference oscillations with maximum amplitude at $\tau = 0$ and which decay in amplitude with a Gaussian envelope.

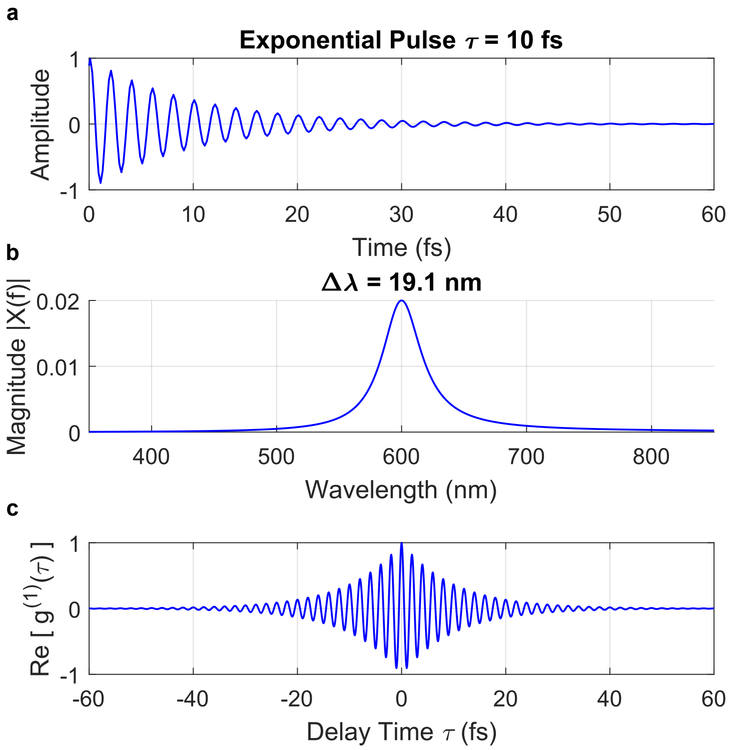

Figure 3: Interference with a Lorentzian Pulse (a) Oscillation of the electric field exponentially decaying pulse with decay rate τ =10 fs at 600 nm. (b) The fast Fourier transform is used to show the pulse's frequency distribution, which is then converted to show wavelength distribution in nm. The pulse has $\Delta\lambda \sim 19nm$ (c) First-order correlation $g^{(1)}(\tau)$ displays interference oscillations with maximum amplitude at $\tau = 0$ and which decay in amplitude with a symmetric exponential envelope.

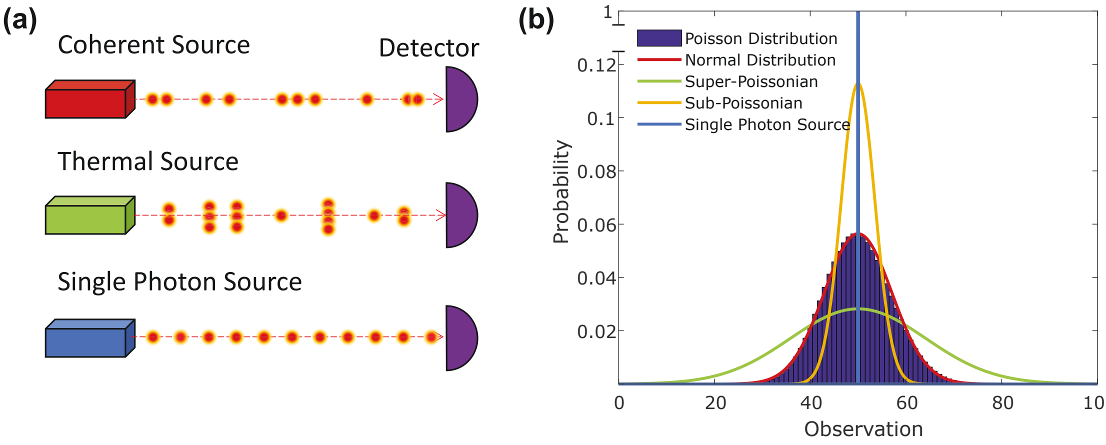

Figure 4: Photon Statistics (a) Schematic of photon temporal distribution of three types of photon sources. (b) Probability distributions with mean photon number $\bar{n} = 50$, for Poissonian $\Delta n = \sqrt{\bar{n}}$, super-Poissonian $\Delta n > \sqrt{\bar{n}}$, and sub-Poissonian $\Delta n < \sqrt{\bar{n}}$

$10\,fs$. Here we note the distinction between angular frequency Ω and frequency Δv. Again, by taking the FFT and converting to nm, we observe the wavelength distribution for the photon wave-packet of $\Delta\lambda \sim 20\,nm$ (Fig. 3(b)). We also note this time the line shape is described by Lorentzian distribution with FWHM $\Delta\Omega$. Once again such a distribution could easily be measured using the Michelson interferometer, and we would observe an exponential decay of the first-order correlation as shown in Figure 3(c), given by:

$$g^{(1)}(\tau) = e^{-i\omega_0 t} \exp\{-|\tau|/\tau_c\} \tag{29}$$

0.4.2 DEFINITION AND TYPES OF LIGHT SOURCES

The quantisation of the electric field as described above led to the interpretation that the electric field is made of individual particles known as photons, coined by Lewis in 1926.[19] Each of these photons is a quantised excitation of the EM field with energy E, given by:

$$E = hv \tag{30}$$

where h is Planck's constant and v is the photon frequency.

If we consider a light source, we can think about the average intensity of this source to represent the average number of photons we would receive per some window of time. Interestingly, as we reduce the window length in time, we find the average number of photons per window doesn't always decrease linearly. It is actually the case that the temporal distribution of photons from different sources changes depending on the source, therefore it is not enough to only consider the mean count rate, we must also consider their photon statistics. In general, there are three categories of photon sources, see Figure 4. Coherent sources, such as a laser, have a random delay between photons and thus follow a Poissonian distribution. Thermal light sources have a high probability of emitting multiple photons at a time (bunched), thus they follow a super-Poissonian distribution. Single-photon sources only ever emit one photon at a time and have a characteristic "minimum" time between photons, known as the radiative lifetime τ_r. Single-photon sources are the only class of sources that follow a non-classical behaviour and show a sub-Poissonian distribution.[66] An ideal source of single-photon source only ever emits one photon at a time with 100% fidelity and can be activated on demand, via optical or electrical excitation.

Classical Hanbury Brown and Twiss - Second-order correlation

The simplest way to measure the difference between these sources and quantify exactly the nature of the photon distribution over time is to measure the second-order coherence of the stream of photons and compare this with the second-order correlation function (also known as the second-order autocorrelation function). This is implemented using a Hanbury Brown and Twiss interferometer setup, which measured the intensity correlations of two detectors A and B after a beamsplitter, Figure 5(a). Whilst the first-order correlation measures how the electric field changes over time (coherence), the second-order correlation measures how the intensity of an electric field changes over time (i.e. temporal coherence), and is given by;

$$g^{(2)}(\tau) = \frac{\langle E^*(t)E^*(t+\tau)E(t+\tau)E(t)\rangle}{\langle E^*(t)E(t)\rangle\langle E^*(t+\tau)E^*(t)\rangle} = \frac{\langle I(t)I(t+\tau)\rangle}{\langle I(t)\rangle\langle I(t+\tau)\rangle} \tag{31}$$

where $E(T)$ is the classical electric field, and $I(t)$ is the intensity of the light field at time t.

For a classical field that has no fluctuation in intensity over time $I(t) = I(t+\tau)$, the second-order correlation is always one $g^{(2)}(\tau) = 1$. For a chaotic light source, such as an atomic discharge lamp, the second-order correlation is always greater than one at $t = 0$ (Fig 5(b)). For a classical Doppler-broadened chaotic source, with Gaussian coherence length τ_c, and lifetime-broadened chaotic source, with Lorentzian coherence length τ_0, the second order correlation is given by;

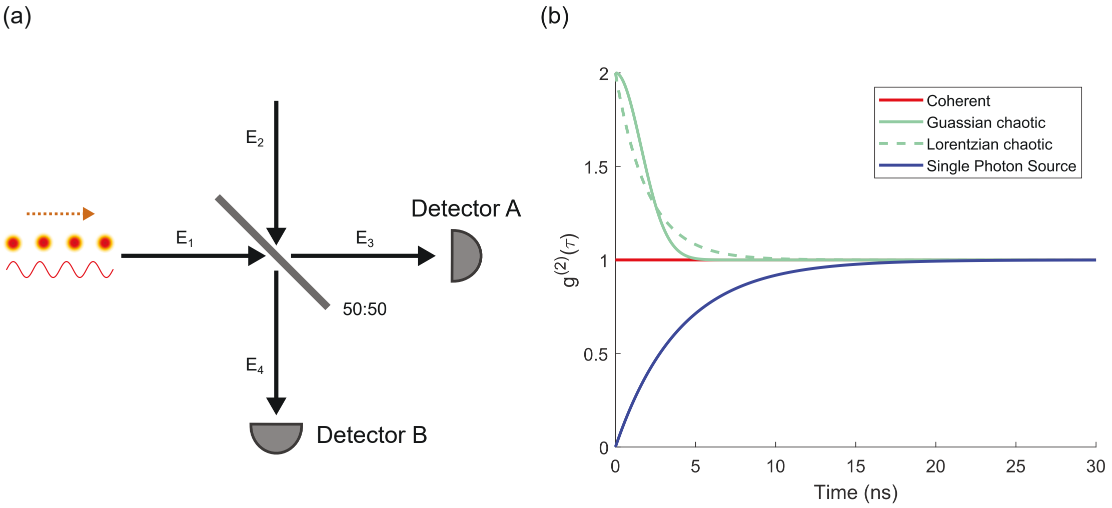

Figure 5: The beamsplitter and the second-order correlation function. (a) Schematic representation of a beamsplitter with spatial modes E_1 through E_4. For the Hanbury-Brown and Twiss experiment, single photons enter only through one port and the correlation between photon detection events are made using detectors A and B. (b) Second-Order Correlation plots for a perfectly coherent source (red), a Doppler-broadened chaotic source with Gaussian lineshape (solid green), a lifetime-broadened chaotic source with Lorentzian lineshape (dashed green), and a non-classical single-photon source (blue).

$$g_g^{(2)}(\tau) = 1 + \exp\{-\pi(\tau/\tau_c)^2)\} \tag{32}$$

$$g_l^{(2)}(\tau) = 1 + \exp\{-2|\tau|/\tau_0\} \tag{33}$$

Interestingly, for all classical fields it is trivial to see that $g^{(2)}(\tau) \geq 1$ for all values of τ. To understand the second-order correlation for quantised fields, with respect to single photons, we must rewrite Eqn. 31 in terms of the photon number operator $\hat{n}$.

Quantum Hanbury Brown and Twiss - Second-order correlation

The number of photons n is related to the number operator $\hat{n}$ by, $\hat{n}|n\rangle = n|n\rangle$, where $|n\rangle$ is the photon number state. The number operator $\hat{n}$ is related to the creation, $\hat{a}^\dagger$, and annihilation, $\hat{a}$, operators by $\hat{n} = \hat{a}^\dagger\hat{a}$. The second-order correlation for quantised particles can be written in terms of the number of photons n that arrive on detector A or B as;

$$g^{(2)}(\tau) = \frac{\langle n_A(t) n_B(t+\tau)\rangle}{\langle n_A(t)\rangle\langle n_B(t+\tau)\rangle} \tag{34}$$

and more generally in terms of the ladder operators as;

$$g^{(2)}(\tau) = \frac{\langle \hat{a}_A^\dagger(t)\hat{a}_B^\dagger(t+\tau)\hat{a}_B(t+\tau)\hat{a}_A(t)\rangle}{\langle \hat{a}_A^\dagger(t)\hat{a}_A(t)\rangle\langle \hat{a}_B^\dagger(t+\tau)\hat{a}_B(t+\tau)\rangle} \tag{35}$$

In the HBT experiment light is only introduced through one input, i.e. an arbitrary state enters port E_1 and the vacuum state enters port E_2, thus the input state is of the form $|\Psi\rangle = |\psi_A, 0_B\rangle$. At $\tau = 0$ eqn 35 is simplified to;

$$g^{(2)}(0) = \frac{\langle \hat{a}_A^\dagger \hat{a}_B^\dagger \hat{a}_B \hat{a}_A\rangle}{\langle \hat{a}_A^\dagger \hat{a}_A\rangle\langle \hat{a}_B^\dagger \hat{a}_B\rangle} \tag{36}$$

Which after applying the input state $|\Psi\rangle$ and some algebra can be simplified to the final result of:

$$g^{(2)}(0) = \frac{\langle \hat{n}(\hat{n}-1)\rangle}{\langle \hat{n}\rangle^2} = \frac{n(n-1)}{n^2} \tag{37}$$

And finally, we see the non-classical result for second-order correlation. For a single-photon source $n = 1$, the second-order correlation dips to zero, $g^{(2)}(0) = 0$, lower than the ideal monochromatic wave with perfectly constant intensity (Fig 5(b)). Interestingly this is not the only result as we can now deduce an estimate for the number of single-photon sources at a given location by extracting the exact value of $g^{(2)}(0)$, i.e. for two single-photon sources, with equal brightness, $n = 2$ and $g^{(2)}(0) = 0.5$, similarly for $n = 3$, $g^{(2)}(0) = 0.67$.

Clearly, significant information about a source's nature is revealed using first- and second-order correlation. For an ideal SPS, the second-order correlation should dip all the way to 0 at $\tau = 0$, but experimental limitations mean this often is not the case. In general, it is widely accepted that a dip below 0.5 i.e. $g^{(2)}(0) < 0.5$, is enough to signify a source is indeed from a single defect.[67,68] Limitations due to the timing jitter of detectors and background fluorescence, and ways to quantify and account for them are covered in the appendix (section: A.1).

0.4.3 LIFETIME AND EMISSION RATE

An ideal single-photon source (also known as a quantum emitter) has a number of key properties. First and foremost it must only emit one photon at a time as discussed above. The next key property is its brightness, or spontaneous emission rate Γ_r. The spontaneous emission rate of an SPS is inversely proportional to its fluorescence lifetime τ_r, which is the average time it takes for a photon to be emitted after the system has been excited by an external energy source (usually optically or electrically). For a quantum emitter, the spontaneous emission rate is completely determined by its immediate environment defined by its refractive index n, the transition frequency ω_{eg}, and the transition dipole moment μ_{eg}, between ground and excited states, and is given by;

$$\Gamma_r = \frac{1}{\tau_r} = \frac{4}{3n} \frac{\mu_{eg}^2}{4\pi\varepsilon_0 \hbar} \left(\frac{\omega_{eg}}{c} \right) \tag{38}$$

where ε_0 is the vacuum permittivity, $\hbar$ is the Plancks constant in terms of angular frequency, and c is the speed of light.

Conventionally this describes the rate of transition for an electron in a two-level system (TLS). In this picture, an electron decays from an excited state to its ground state via spontaneous emission. On a deeper level, this can instead be considered a stimulated emission triggered by a vacuum photon.[66](p168) The random emission is then attributed to the quantum noise of the zero-point fluctuations of the electric field. Interestingly, as the zero-point energy is defined as $E_{vac} = (\hbar\omega/2\varepsilon_0 V)^{1/2}$ and V is the volume of the cavity, by reducing the volume of the cavity we can increase the magnitude of the vacuum field. This in turn increases the zero-point fluctuations and therefore the spontaneous emission rate. This is also known as increasing the local density of photonic states of a two-level system inside an optical cavity, which decreases the radiative lifetime (the Purcell effect).

0.5 HEXAGONAL BORON NITRIDE

Hexagonal boron nitride (hBN) is an atomically thin van der Waals crystal with a honeycomb structure similar to graphene. Each layer consists of strong ionic and covalent bonds between boron and nitrogen atoms within the basal planes, and relatively weak inter-layer bonds due to the van der Waals interaction. The differing bond strength causes hBN to be anisotropic and the strong electron-localisation from the ionic/covalent bonds caused hBN to have a large bandgap of around 5.9 eV, much greater than most two-dimensional materials.[69] This large bandgap results in hBN being optically transparent from the visible to the near IR.[70,71] The weak interlayer bonding allows for mechanical exfoliation of thin hBN flakes all the way down to monolayers, which enables hBN to be used in heterostructure applications.[72] Due to its low defect density and atomically smooth surface it has shown to have a number of applications in 2D heterostructure nano-electronics, acting as a strong insulator, tunnelling barrier, or increasing the carrier mobility in graphene and other 2D semiconductors.[73,74,75,76,77]

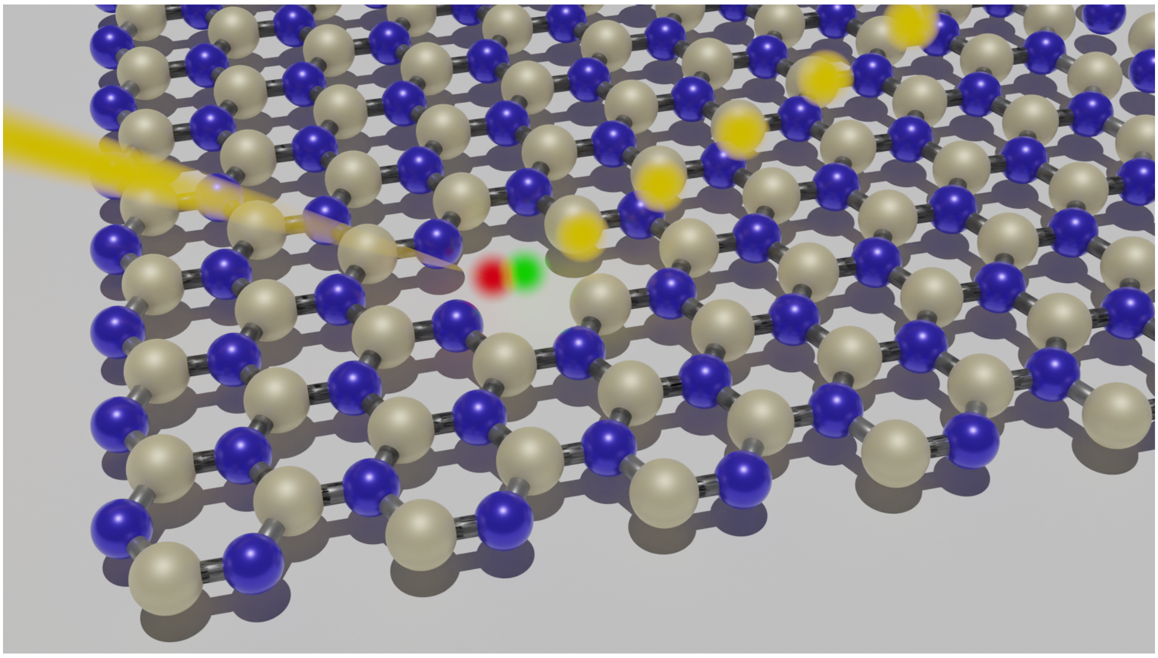

Figure 6: Crystal structure of a hexagonal boron nitride monolayer. Hexagonal lattice structure with alternating boron (beige) and nitrogen (blue) atoms. A defect in the lattice forms a two-level system that can be excited to emit photons.

Though historically seeing significant usage as a dry lubricant in industry, applications with hBNs optical properties only started gaining momentum in 2004 when Watanabe et al. reported on the direct band-gap emission from hBN. This opened up hBN as an emerging material with applications in far UV nanophotonics.[78,79] In contrast to the previous reports in 2016 Cassabois et al. demonstrated that hBN had an indirect band-gap, which opened some controversy about hBN excitonic emission.[80] In this report Cassabois et al. also highlighted the exciton coupling strengths to hBNs optical and acoustic phonon modes. Due to the Frölich interaction electron-phonon coupling is strongest to the high energy longitudinal optical (LO) and transverse optical (TO) phonon modes, with energies of 188 and 162 meV respectively. Exciton scattering via the lower energy acoustic modes is less efficient due to the deformation potential and piezoelectric coupling, with ZA, TA, and LA, having energies of 22, 64, and 95 meV respectively.[81,82,80]

0.5.1 Quantum Emission from hBN

In 2015, Toan Trong Tran made the exceptional discovery point defects in hBN crystals can form an isolated two-level system (TLS) within the band gap that acts as a single-photon emitter at room temperature.[83] These defects can be considered akin to an artificial atom that can be excited with below bandgap

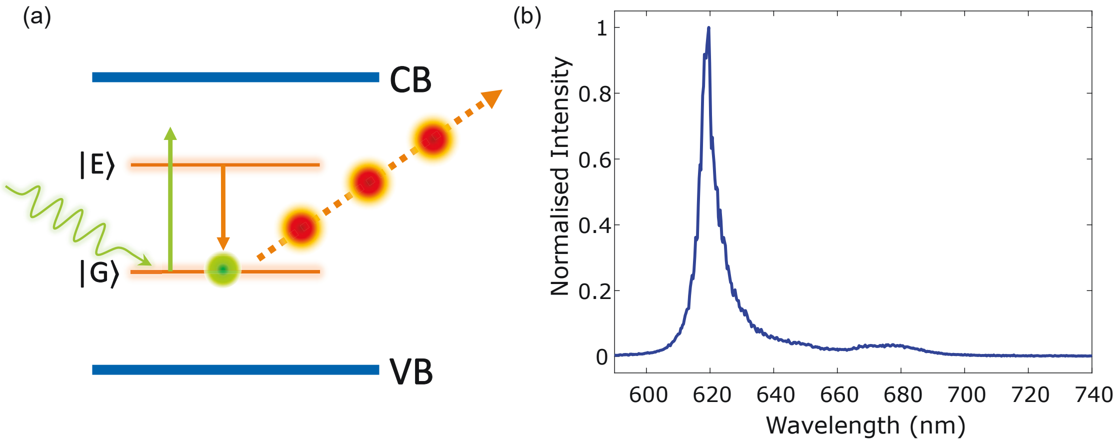

Figure 7: A simplified Jablonski diagram for a two-level system within the bandgap. An electron (green ball) can be excited via Stokes excitation from a lower energy "ground" state $|G\rangle$ to a higher energy "excited" state $|E\rangle$. After some time τ_r, the electron can decay radiatively and emit a single photon (red balls).

excitation and upon relaxation can emit a single photon, as illustrated schematically on a simplified Jablonski diagram in Figure 7(a). The emission from these defects consists of a bright and narrow zero-phonon line (ZPL) and a dim phonon side-band emission red-shifted by ∼160 meV, associated with radiative emission with energy loss via a TO/LO phonon. This very low electron-phonon coupling is characterised by a low Huang-Rhys factor of 1.66, which results in around 70% of emission into the ZPL. This compares very favourably to other solid-state defects such as the nitrogen-vacancy (NV) centre in diamond that only emits around 3% into the ZPL at room temperature (Huang-Rhys factor of 3.73).[84,85] An example spectrum for the emission of an hBN SPE is shown in Fig. 7(b); a narrow emission peak is observed at 620 nm and the phonon sideband (PSB) emission is seen at around 675 nm. Single-photon emission from defects was first observed in the visible spectrum around 580 and 620 nm but has since been observed from the UV to the near-IR.[86,87] Due to hBNs high chemical and structural stability the emission from these defects has been observed from cryogenic temperatures to >800 K, with a temperature-dependent linewidth, opening applications in robust environments and in nanoscale temperature sensing.[88,89,90] It is also possible to tune the emission wavelength of these emitters via the Stark effect and strain tuning over tens of nanometers has been observed, opening mechanical sensing and wavelength-dependent applications.[91,92,93,94] The emitters have also been shown to have relatively high purity, which can be enhanced via post-processing techniques.[95,96].

An integral next step for many quantum applications of these emitters is coupling them to photonic structures. A broad range of advanced functionalities are enabled through photonic structures, some via the scalability enabled through large-scale processing techniques and others directly related to the source such as enhanced collection via directional scattering or coupling to waveguides.[97,98] Photonic structures can enhance single-photon emission via the Purcell effect due to the modulation of the emitter environment and photonic density of states. This results in increased brightness via lifetime reduction and linewidth narrowing which is integral when moving toward indistinguishable sources.[99] There has even been research towards a fully integrated single-photon source with near-term applications in satellite-based quantum communication.[96,100]

0.5.2 BROADENING MECHANISMS

So far I have introduced single-photon emission from two-level systems resulting from point defects in hBN. Next, I will introduce what I consider to be the most fundamental requirement of quantum emitters for applications in quantum technologies: photon indistinguishability. All advanced applications in quantum information processing, and a significant portion of applications in quantum communication and metrology/sensing, require multi-photon entanglement. The entanglement of two photons incident on a 50:50 beamsplitter is described as the Hong-Ou-Mandel effect.[101,102] This quantum interference phenomena results in the bunching of photons after the beamsplitter, i.e. after the beamsplitter of Fig. 5(a) the photons exist in a NOON state where both photons exit together either in spatial mode E_3 or E_4 $|\Psi_{NOON}\rangle = \frac{1}{\sqrt{2}}|N\rangle_3|0\rangle_4 + e^{(iN\varphi)}|0\rangle_3|N\rangle_4$. To observe this effect, the photons must have completely overlap in space (spatial mode matching), they must have the same polarisation state, and finally, they must have identical wavepackets.

ENERGY UNCERTAINTY

The ideal two-level system emits indistinguishable photons where the linewidth of the photons is completely defined by the spontaneous emission lifetime. Using the energy-time uncertainty principle we know $\Delta E \Delta t \gtrsim \hbar$, this means the uncertainty in the energy of a state is inversely proportional to the lifetime T_1 of the state;

$$\Delta v = \frac{1}{2\pi T_1} \tag{39}$$

given $E = \hbar\omega$ and $v = \omega/2\pi$, as above. Eqn. 39 is known as the Fourier or lifetime limited linewidth. The exponential decay for this spontaneous emission is also why Fourier-limited photons have a Lorentzian frequency distribution.

Unfortunately for most defects in solid-state materials, this ideal behaviour is rarely observed, and in the majority of cases, the line is broadened further due to interactions between the two-level system and its environment. These interactions are further categorised into homogeneous and inhomogeneous broadening.

HOMOGENEOUS BROADENING

Homogeneous broadening refers to the non-radiative relaxation through the release of phonons. The relaxation time of these non-radiative transitions can be extremely fast thus the excited state lifetime is reduced, and the linewidth is broadened. This is the solid state equivalent of collisional broadening and is often considered as abrupt phase jumps within the photon wavepacket thus is coined with the term dephasing. Pure dephasing is conventionally given the lifetime T_2^*, maintains a Lorentzian lineshape, and is only meant to account for electron-phonon coupling within the bath.[103,104,105,106,107,68] Though the terminology is sometimes mistaken within the literature and described as spectral diffusion.[68]

In this case, the dephasing rate, or (de-)coherence time, T_2, and resulting linewidth, Δv are given by;

$$\frac{1}{T_2} = \frac{1}{T_1} + \frac{1}{T_2^*} \tag{40}$$

$$\Delta v = \frac{1}{2\pi T_1} + \frac{1}{\pi T_2^*} \tag{41}$$

Note that when dephasing is negligible $T_2^* = \infty$, we return to the Fourier limited linewidth.

INHOMOGENEOUS BROADENING

The final, and often most troublesome, broadening mechanism is known as spectral diffusion. In this case, charge inhomogeneities of the host matrix/material modulate the two-level system over time and cause decoherence.[66] These environmental functions include local charge traps, local electric field/strain fluctuations, and surface states. As the energy of the two-level system varies corresponding to the local field fluctuations, the rate of this modulation varies significantly but generally is considered slower than homogeneous broadening. With this additional term, the coherence time T_2 and linewidth Δv are given by;

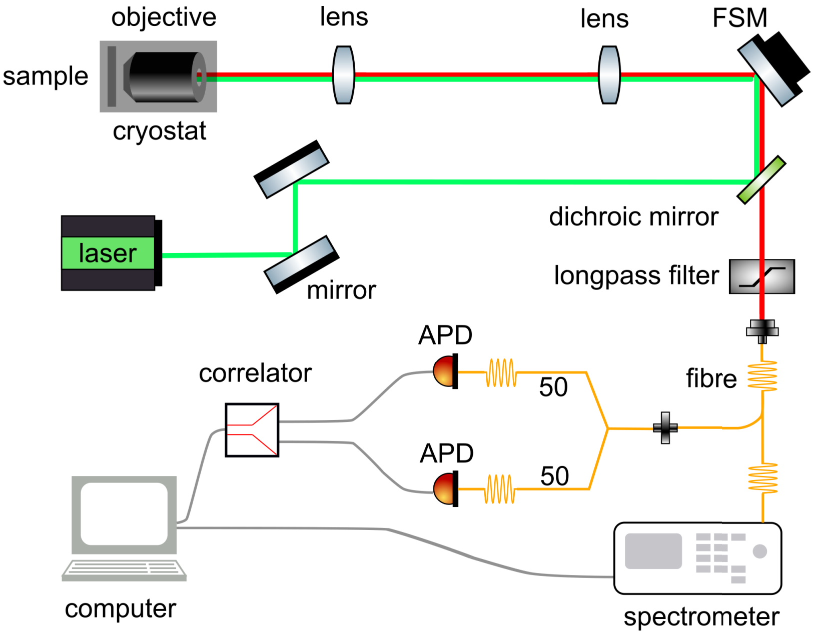

Figure 8: Schematic of the confocal photoluminescence setup (FSM, fast steering mirror; APD, avalanche photodiodes). The dichroic mirror is replaced by a 90/10 beamsplitter for experiments requiring excitation using a tunable laser.

$$\frac{1}{T_2} = \frac{1}{T_1} + \frac{1}{T_2^*} + \sigma_{SD} \tag{42}$$

$$\Delta v = \frac{1}{2\pi T_1} + \frac{1}{\pi T_2^*} + \sigma_{SD} \tag{43}$$

0.6 CONFOCAL MICROSCOPY

Laser scanning confocal microscopy is a measurement technique used extensively throughout this thesis. Working in a dedicated photonics lab enables us to build a custom setup (an open tabletop microscope), which can be reconfigured for individual experiments to add or change functionality accordingly.

A continuous-wave (CW) 532 nm laser (Gem 532™, Laser Quantum Ltd.) is used for excitation and photoluminescence (PL) scanning. The beam is directed via a 532 nm dichroic mirror (LP03-532RE-25) into the attoDRY800 cryostat and focused to a diffraction-limited spot on the sample using a vacuum compatible high numerical aperture objective (attocube LT-APO/VISIR 0.82 NA). A 4f lens system and X-Y piezo scanning mirror (FSM-300™) are used to scan the spot over the sample. The collected light is filtered using the dichroic mirror and an additional long-pass filter (568 LP filter, Semrock™). Confocality is achieved using a 62.5 graded-index multimode fibre as a pinhole in the collection. For finer spatial resolution the multimode fibre can be replaced with a single-mode fibre, with the caveat that single-mode fibres are highly wavelength selective. The signal is then collected using this fibre and directed to a spectrometer for spectral characterisation (room temperature measurements using a Princeton Instruments Acton SpectraPro™ with 300, 600, or 1200 lines/mm gratings, and cryogenic measurements using an Andor Shamrock 303i with 300 or 1800 lines/mm gratings). The multimode fibre can also direct the PL to avalanche photodiodes (Excelitas SPCM-AQRH) for single-photon counting, PL mapping, and autocorrelation measurements. Second-order correlation measurements are made using a fibre-based Hanbury-Brown and Twiss setup and a time-correlated single-photon counting module (Swabian, TimeTagger20 or a Picoharp 300).

0.6.1 COHERENT EXCITATION

Resonant, or coherent, excitation describes the interaction between a driving field and a two-level system where the energy of the field ($E = \hbar\omega$) precisely matches the difference in energy between the two states E_1 and E_2 of a TLS (frequency $\omega_0 = (E_2 - E_1)/\hbar$), i.e. their difference in frequencies is small $\delta\omega \rightarrow 0$. In this scenario, the position of an electron in states $|1\rangle$ and $|2\rangle$ (corresponding to the ground $|G\rangle$ and excited $|E\rangle$ states above) is not described by discrete transitions between separate states, but instead must be described as the oscillation between these states. That is, the electron exists in a superposition of both states simultaneously and is described by the wavefunction $|\Psi\rangle = c_1|1\rangle + c_2|2\rangle$. In the strong field limit, the oscillation between these states occurs at the Rabi frequency of the system Ω_R, with the probability of being measured given by;

$$|c_1(t)|^2 = |\cos(\Omega_R t/2)|^2 = \cos^2(\Omega_R t/2) \tag{44}$$

$$|c_2(t)|^2 = |i\sin(\Omega_R t/2)|^2 = \sin^2(\Omega_R t/2) \tag{45}$$

given the particle begins in the lower level at $t = 0$.

The above solution is only observed when the two-level system does not experience significant damping. The first damping term is due to the decoherence caused by spontaneous emission. At low excitation powers, the Rabi period is longer than the lifetime τ_r and oscillations won't be observed. Thus to see coherent oscillations high excitation powers must be used to significantly reduce the Rabi frequency. Unfortunately, radiative decay is not the only dephasing process and pure dephasing, due to the coupling between the two-level system and the environment, causes the phase terms between ground and excited states to become randomised. This pure dephasing process was introduced earlier (see sec. 0.5.2 and is also the cause of the homogeneous broadening of a transition. Due to this randomisation of phase, the coherence between the ground and excited states is lost, and Rabi oscillations are destroyed. Due to this dephasing, it can be shown the probability that the electron is in the upper state is given by:

$$|c_1(t)|^2 = \frac{1}{2(1+2\xi^2)}\left[1-\left(cos\Omega' t + \frac{3\xi}{(4-\xi^2)^{1/2}} sin\Omega' t\right) exp\left(-\frac{3\gamma t}{2}\right)\right] \tag{46}$$

Where the damping rate γ is given in relation to the Rabi frequency by $\gamma = \xi\Omega_R$, and $\Omega' = \Omega_R\sqrt{1-\xi^2/4}$. For extreme cases of damping ($\xi >> 1$) we see no oscillations and transition probability reduced to an asymptotic function give by:

$$|c_1(t)|^2 = \Omega_R^2/4\gamma^2 = \frac{\mu_{12}^2 E_0^2}{4\hbar^2\gamma^2} \tag{47}$$

Where μ_{12} is the transition dipole moment.

The observation of coherent Rabi oscillations clearly requires the damping rate to be significantly smaller than the Rabi frequency ($\gamma << |\mu_{12}E_0/\hbar| \equiv \Omega_R$ and the temporal resolution shorter than $1/\Omega_R$. In solids with phonon and free-charge scattering causing dephasing, γ, on the order of 1 THz and Ω_R on the order of 1 GHz this can often become experimentally challenging. Nonetheless Rabi oscillations have been observed in hBN and other solid-state defects.[108,6,109,110,111,112,113]

0.6.2 Photoluminescence Excitation

Fortunately, the Rabi cycle phenomenon is not the only important phenomenon observed using coherent excitation. Photoluminescence excitation is the technique where a narrow laser is scanned over the energy of a two-level system and the emission from the two-level system is monitored using avalanche photodiodes. Due to efficient absorption when a resonant laser matches the emission energy of a two-level system, we can use this technique to precisely determine the energy and bandwidth of the TLS. A similar optical path to the confocal setup above is used when exciting the sample with the tunable lasers (listed below).

Laser Name	Tuneability	Gain	Linewidth	Further Specifications
Sirah Matisse 2 DX	Cavity	Rhodamine dye	<200 kHz	570-610 nm w/ WS6
M^2 SolsTiS	Cavity	Ti:Sapphire	<50 kHz	720-940 nm w/ WS6
Fianium Whitelaser	Acousto-Optic filter	Supercontinuum	≈ 5 nm	20 - 80 MHz pulsed and CW

Due to the narrow linewidth for the Ti:Sapphire and Rhodamine Dye lasers, and their relatively broadband tuneability we are able to study defects with emission in the visible and near-infrared wavelengths. In this case, the dichroic mirror is replaced with a 90:10 (transmission:reflection ratio), and the reflected laser is rejected using a Semrock long-pass filter.

For electrical control measurements, a bias is applied to the device (within the cryostat via a vacuum feed through) using either a Keithley Tektronix source-meter (2612B) SMU or an Agilent function generator (33522A).

χαλεπὰ τὰ καλά

"Khalepà tà kalá" - (What is) good/beautiful (is) troublesome.

Plato, Republic 4, 435c

1

Quantum Random Number Generation

Quantum random number generation (QRNG) harnesses the intrinsic randomness of quantum mechanical phenomena. On-chip photonic circuitry provides robust a versatile platform that can address and explore fundamental questions in quantum as well as classical physics. Likewise, integrated waveguide-based architectures hold the potential for intrinsically scalable, efficient and compact implementations of photonic QRNG. Here, we harness the quantum emission from the two-dimensional (2D) material hexagonal boron nitride — an emerging atomically thin medium that can generate single photons on demand while operating at room temperature. By means of a customised splitter arrangement, we achieve true random number generation through the measurement of single photons exiting one of four designated output ports, and subsequently verify the randomness of the sequences in accordance with the National Institute of Standards and Technology benchmark suite. Our results clearly demonstrate the viability and efficiency of this approach to on-chip deterministic random number generators.

1.1 Introduction

The fundamental unpredictability inherent in genuine random numbers is vital for truly secure encryption, data science, and fundamental research[32,114]. Yet obtaining true randomness turns out to be a highly nontrivial task: Many conventional random number generators (RNGs) are actually pseudo-random, and, at their core, require a trusted source of randomness to expand with deterministic algorithms[115]. While such pseudo-random sequences can be obtained with great speed and efficiency, they tend to be subject to long-term correlations. Beyond being a mere nuisance in data science and fundamental research, low-quality random number generators introduce critical points of failure in cryptographic applications[116]. A particularly elegant approach to the generation of sequences of fundamentally random numbers are measurements of multipartite quantum states[117]. Here the pursuit of randomness can be simply realised through the measurement of quantum superposition, that is, the measurement of a particle that exists in multiple states simultaneously. In this vein, a wide range of platforms for quantum random number generation (QRNG) have been implemented, ranging from the prototypical examples of radioactive decay[118], vacuum fluctuations[119], laser phase fluctuations[120,121], to single photons in path superposition[122,123,124] and even device-independent realisations[125].

Light, and specifically single photons, is particularly attractive as it offers numerous advantages to quantum information processing, communication, sensing, and miniaturisation in optically-integrated chips[38]. Using deterministic, sub-Poissonian, light sources hardware limitations can be circumvented offering significant advantages for quantum random number generation[126]. In particular, substantial efforts are being undertaken to utilise solid-state sources that can be triggered on-demand, such as quantum dots[127], single molecules[128], or colour centers in wide-bandgap materials[129]. Of the latter, point defects that act as single-photon emitters (SPEs) in the van der Waals material hexagonal boron nitride (hBN) have recently gained great attention owing to their exceptional brightness, photostability, and tunability[91]. There is significant progress toward fabrication of defects[130,92,131,132] and recent works with aims of identifying their structure[133,134,135,136]. The applicability of these emitters for quantum communications has also recently been explored with demonstrations of Fourier transform limited line widths[137] and the realisation of photonic crystal cavities that allow for Purcell enhancement and applications in cavity quantum electrodynamics[138].

On-chip coupling of single-photon emitters, state manipulation, and detection are the fundamental

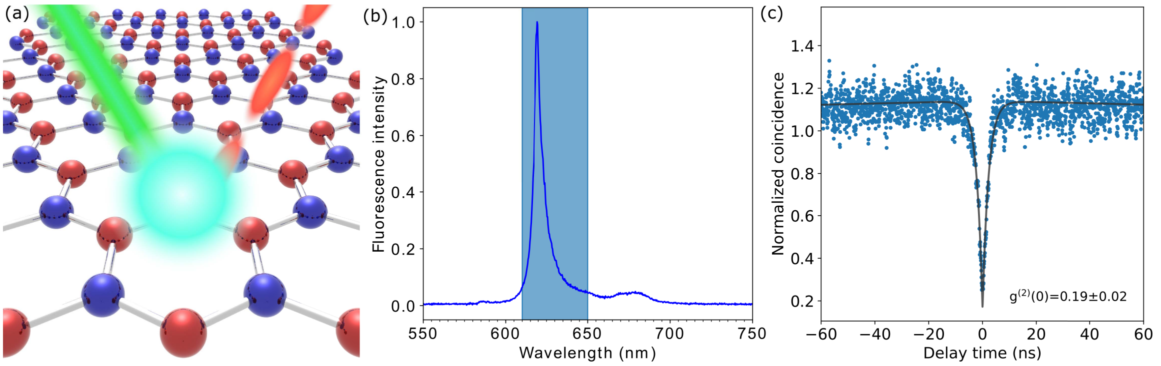

Figure 1.1: A hexagonal boron nitride single-photon emitter. (a) A point defect in the hexagonal lattice of boron and nitrogen atoms is excited by a 532 nm laser to emit a stream of discrete photons. (b) Photoluminescence spectrum of the hBN defect, comprised of a sharp zero-phonon line at 619 nm and phonon side-bands at 675 nm. The single-photon emission is isolated using a 630 ± 20 nm band-pass filter, as indicated by the blue-shaded region. (c) The antibunching curve of the spectrally filtered emission (blue dots) confirms room-temperature single-photon emission, with a fit minimum $g^{(2)}(0) = 0.19 \pm 0.02$.

building blocks for integrated quantum photonics. While the coupling of quantum emission from point defects in 2D materials to optical waveguides has recently been achieved[139,140], we combine this approach with on-chip photonic quantum state manipulation, the next step towards harnessing hBN emitters for scalable integrated quantum photonics.

1.2 EXPERIMENTAL WORKS

1.2.1 METHODS

The hexagonal boron nitride used in our experiments was prepared using commercial multilayer flakes dispersed in solution (Graphene Supermarket). For specific samples to be identified and targeted in a readily reproducible fashion, the hBN solution was drop-cast on a marked silicon substrate and subsequently annealed at 850 $^{\circ}C$ under 1 Torr of argon atmosphere to activate the emitters. This preparation allowed us to choose from a wide range of different multilayer hBN flakes with diameters between 100 and 500 nm, and a thickness in the range of 10 - 40 nm[141]. To reveal the location of the desired point-defect SPE in hBN a photoluminescence (PL) map of the sample was taken using a custom-built scanning confocal microscope[83]. The chosen defect was excited, below saturation, using a 100 µW, 532 nm laser to emit a stream of discrete photons, as illustrated schematically in Fig. 1.1(a). The emission is collected using a 0.9 NA objective (Nikon) and is directed via a multimode fibre for confocal scanning or spectral measurement, using a Princeton Instruments spectrometer (300 lines/mm), or is sent via free space and coupled to the multiplexing chip with a lens. The photoluminescence spectrum of the emitter used in our subsequent experiments is shown in Fig. 1.1(b). To isolate the zero-phonon line (ZPL) from the emission via the phonon sideband (PSB), a tunable band-pass filter was rotated to centre over the ZPL, as highlighted in Fig. 1.1(b). The excited-state lifetime, τ_1, is measured based on the autocorrelation data as $\tau_1 \approx 1.9$ ns, which is comparable with literature values for an hBN SPE[83]. To confirm the single-photon emission from the defect, second-order autocorrelation, $g^{(2)}(\tau)$, was measured using a fibre-based Hanbury-Brown-Twiss interferometer. The normalised histogram, seen in Fig. 1.1(c), is not background-corrected and fit with a three-level model. The fit exhibits a minimum $g^{(2)}(0) = 0.19 \pm 0.02$, well below the threshold value of 0.5, unequivocally indicating single-photon emission from a single defect[142].

As scalability and robustness are key features of integrated optical waveguides, we designed a compact photonic circuit resembling a wagon wheel. In the functional region of this circuit, symmetric radial coupling is employed to convert the stream of single photons from the hBN source injected into the single spatial mode of its central input port to a multi-path superposition state spanning nine output channels (see Fig. 1.2(a)). Notably, in contrast to previous chip designs employing cascaded sequences of directional couplers[122], the functional region of this chip is invariant in propagation direction and, therefore, free of radiation losses associated with repeated s-bends. Moreover, the radial symmetry of the arrangement serves to protect the splitting ratio from deviations due to the inevitable wavelength dependence of the coupling, a crucial aspect in designing circuitry for highly tunable sources such as hBN. The chip was fabricated in fused silica (Corning 7980) using the femtosecond direct laser writing technique[143]. 150 fs pulses from a commercial laser system (Coherent Mira/RegA) with a 100 kHz repetition rate at a carrier wavelength of 800 nm were focused approximately 200 μm below the sample surface using a standard microscope objective (20×, 0.36 NA). By moving the sample with respect to the focal spot with a positioning system (Aerotech Inc.), waveguides with a refractive index contrast of approximately 5×10^{-4} were created along the desired trajectories. At a wavelength of 815 nm, the waveguides support an elliptical mode profile of 9×13 μm and feature intrinsic propagation losses below 0.3 dB/cm. In order to ensure identical couplings to all outer waveguides despite the intrinsically anisotropic coupling behaviour[144], the vertical waveguide spacing in the active region of the splitter was systematically increased, distributing the outer channels around an ellipse with half-axes of 20 μm and 23 μm respectively, as seen in Fig. 1.2(b). Finally, the central guide was inscribed with a slightly lower propagation constant so as to achieve phase matching to the staggered super-mode of the outer ring. A subsequent three-dimensional fan-out section serves to rearrange these cores to line up with the standard 127 μm pitch of commercially available fibre arrays[145].

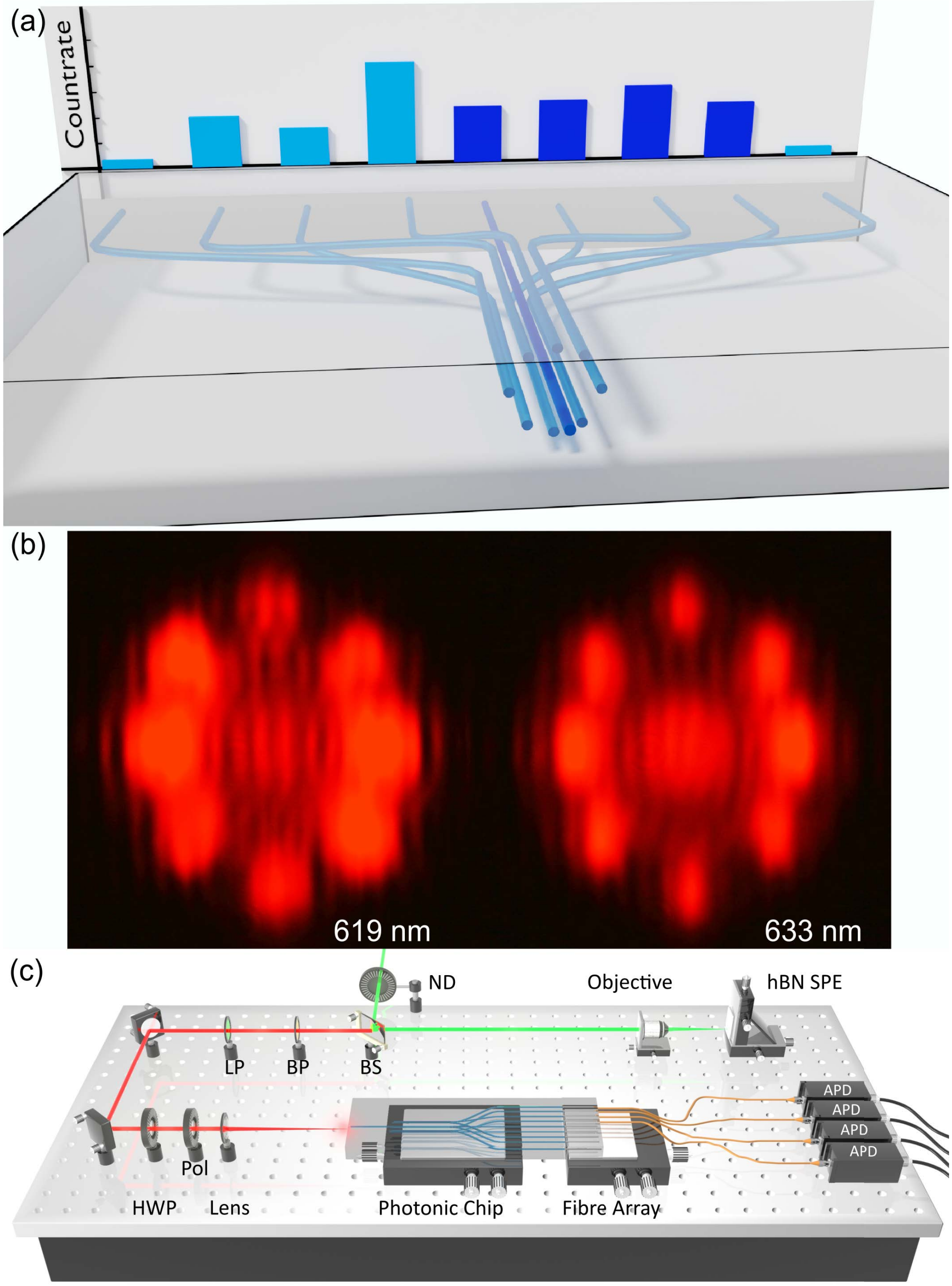

Figure 1.2: Schematic of the chip. (a) Light from a single input waveguide is distributed using a wagon-wheel type structure of eight waveguides, which are subsequently fanned out into an equidistant array for out-coupling. Above the structure, the corresponding output single-photon count rates are displayed, where the four chosen waveguides (dark blue) have a measured count rate standard deviation of 11.6 % before induced losses. (b) Splitting performance of the active region of the chip at 619 nm and 633 nm, respectively. The influence of the interface section was omitted by exciting the central channel of the wagon wheel from the output side, and observing the front facet, respectively. (c) Schematic of the experimental setup. A hexagonal boron nitride single-photon source is excited with a $300\,\mu\mathrm{m}$, 532 nm CW laser and photons are collected through a 0.9 NA objective. The pump laser is suppressed using a 568 nm long-pass filter (LP), and the zero-phonon line is isolated using a 630±20 nm bandpass filter (BP). The polarisation is then controlled using a half-wave plate (HWP) and a linear polariser (Pol) to optimally match the birefringent fast axis of the waveguide circuit. Photons are directly coupled to the chip using a lens, collected using a multimode fibre array, and detected with avalanche photodiodes (APD).

1.2.2 RESULTS

The hBN single-photon emission is directly coupled to the photonic chip through free space with an aspheric lens (c240tme-b), as illustrated in Fig. 1.2(c). The emitter is excited to produce single photons at a rate of $\sim$ 1 MHz before the chip. Single photons at the output of each waveguide are coupled to a multimode fibre array and detected using avalanche photodiodes (Excelitas) with efficiencies of 65 %, dark counts $<$ 100 Hz, and dead times of 22 ns. Their respective arrival times were recorded using a Swabian Instruments time tagger and are dumped in real-time to a log file via a python script. After the chip, across all nine waveguides, we achieved total throughput of $\sim$ 350 kHz. Here, losses are mainly due to coupling to and from the chip, as well as bending losses associated with the different curvature profiles of the individual waveguide trajectories of the fan-out section. To verify that the single-photon emissions of the hBN source were efficiently coupled to the chip and additional background counts were negligible, we recorded second-order correlations between pairs of output channels ($g^{(2)}_{1,5}(0)$ corresponding to channels 1 and 5). With minimal losses, the single-photon purity is maintained and is unequivocally demonstrated with fit $g^{(2)}(0)$ of 0.24 ± 0.03, 0.25 ± 0.8, 0.20 ± 0.06, and 0.22 ± 0.02 as seen in Fig. 1.3(a), all within one standard deviation of the free space $g^{(2)}(0)$ above.

To obtain a random binary sequence, time-tagged photon arrivals are detected across four avalanche photodiodes (APDs). To maximise the generation rate, we employ a scheme where one photon yields two bits by interpreting each detection event as a two-digit binary number, i.e. ‘00’, ‘01’, ‘10’, or ‘11’, corresponding to each spatial mode where the photon superposition may collapse. This time-tagged sequence records blocks of 100 000 arrival events, which are then immediately transferred from the time-tagger to memory, this is repeated indefinitely until stopped. The creation of the random number sequence occurs after a the entire measurement is completed, but we would also like to note this conversion can happen in real time due to the simple interfacing between hardware (Swabian Time Tagger 20) and software (python). Next we highlight the inherent scalability of this approach: With the creation of larger multiplexed states distributed across 2^n outputs, a single photon can yield n bits, i.e., 2^n numbers, each with probabilities of 2^{-n}. Furthermore, such extended settings will also mitigate potential detector saturation due to the brightness of the hBN source by reducing the average count-rate of each detector involved in the scheme. Balancing the requirements of our proof-of-principle experiments against the quadratic scaling behaviour of resources, and the availability of resources, we chose a configuration of four APDs interrogat-

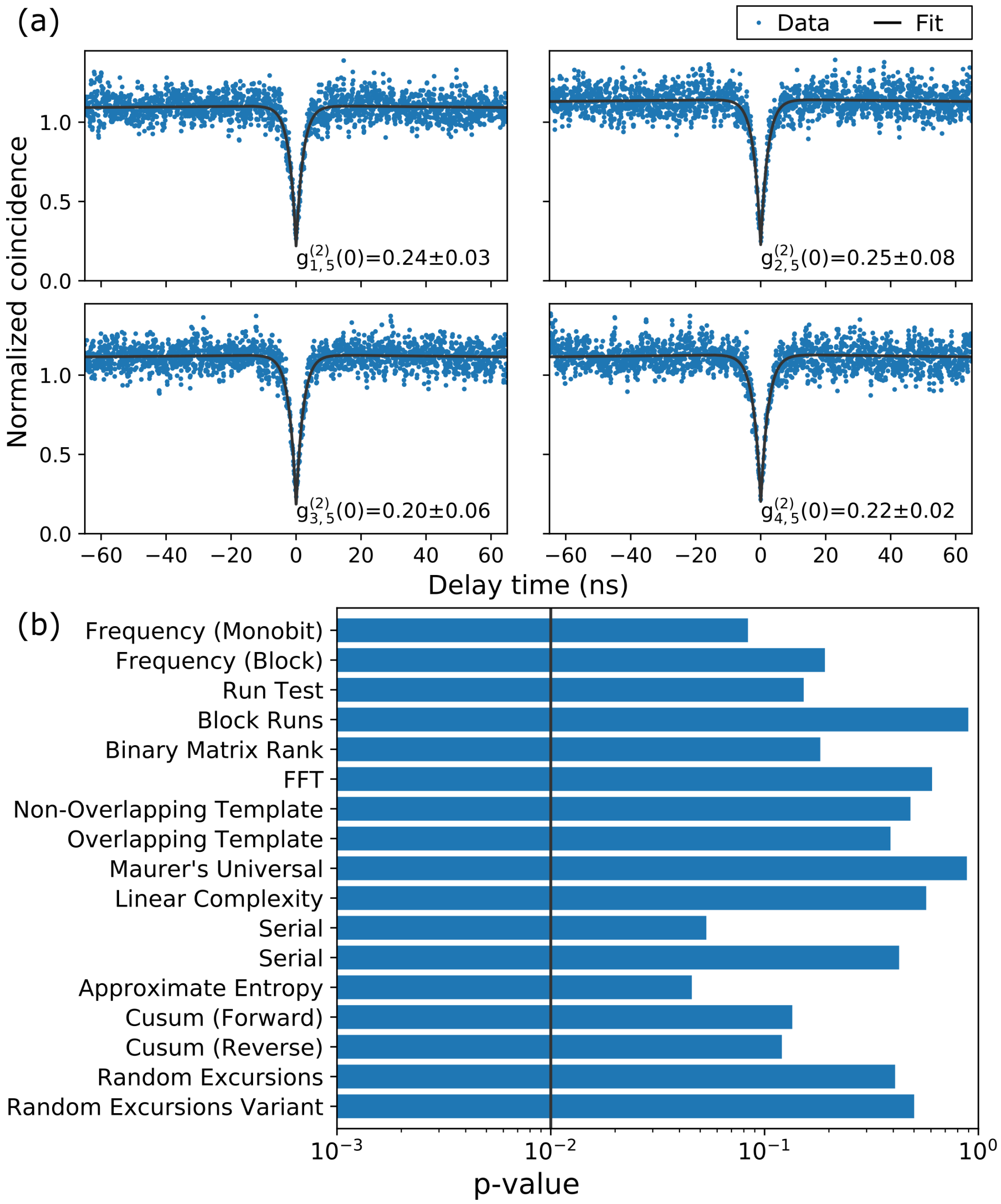

Figure 1.3: Single-photon correlation and random number statistics of the multiplexed state. (a) Antibunching curves show that single-photon purity is retained throughout the chip. Each output is correlated with output 5 and the second order correlation minimum is always significantly below 0.5. (b) NIST randomness test results for a sequence of 1M bits, generated using the arrival of single photons in four spatial modes. The black vertical line displays the minimum p-value required to indicate true randomness (p-value $>$ 0.01) for each test. The Serial test requires two independent p-values both to be greater than 0.01 to be considered random.

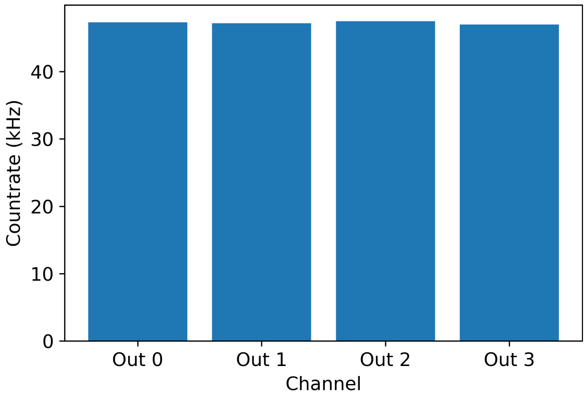

Figure 1.4: Average count-rates for the single-photon multiplexed state. Each output is attenuated to almost identical average count-rates of 47.25 kHz.

ing the four channels highlighted in dark blue in the bar diagram of Fig. 1.2(a). The single-photon count rate distribution after the chip of channels 1 – 4 exclusively were 23, 25, 30, and 23 % respectively. To fully equalise the count rates at the detectors, differences in photon rates of the channels and individual detection efficiencies of the APDs were compensated by deliberately introducing appropriate additional losses through adjusting physical coupling to the fibre via a micrometer in each channel, yielding an optimised detection rate distribution of 25.0, 25.0, 25.1, and 24.9 %. Notably, the outstanding brightness of our hBN emitter yielded a total post-chip count rate of 189 kHz or 47 kHz in each interrogated channel (seen in Fig. 1.4), despite the additional losses and the fact that photons were only collected from four out of the nine total channels.

The randomness of the data stream was evaluated using a python implementation of the National Institutes of Standards and Technologies (NIST) test suite for random and pseudorandom number generators[146,147]. The test suite determines the statistical probability (p-value) that the generated sequence is a random sequence. The tests were performed on sequences of 1,000,000 bits, and for a sequence to be considered random, the p-value of each test must exceed 0.01, given a significance level of $\alpha = 0.01$. Each test has a different interpretation summarised by its shorthand name. For example, the "Frequency" tests determine the absolute ratios of 0's and 1's per section ("Block") or the entirety ("Monobit") of the sequence. The "Runs" tests determine whether uninterrupted sequences of identical bits occur as expected for a random sequence. Template tests identify the probability of specific short sequences appearing throughout the generated sequence. And the "Discrete Fourier Transform" ("Spectral") test detects hidden periodic signatures within the sequence that would indicate the sequence is non-random. Further information on the rest of the tests and the implementation is available on through NIST[146]. To correctly implement the

Test Name	**Relevant Parameter(s)**
Significance value (α)	A = 0.01
Frequency (Block)	M = 10000
Non-overlapping template	m = 10, N = 100
Overlapping template	m = 9
Linear complexity	M = 500
Serial tests	m = 14, p-value 1 and 2 are presented
Approximate entropy	m = 13
Random excursions	All Passed: Average of states -4 to 4 is presented
Random excursions variant	All Passed: Average of states -9 to 9 is presented

Table 1.1: NIST test suite parameters

test suite a number of tests require user-specified parameters along with the binary sequence to be tested. A summary of these parameters is presented in table 1.1, with details on how to set these parameters also available in the test suite documentation[146].

The "Non-overlapping template Matching Test" is used to determine if a random binary string contains too many irregular occurrences of a non-periodic pattern. To be assured the p-values were valid, 100 blocks (N) were chosen to be tested against 284 ten-bit templates (with length $m = 10$). The sequence was determined to be random with an average p-value $= 0.48$, given each template was tested against the significance value $\alpha = 0.01$ (as shown in Figure 1.5.)

Successfully passing all tests, as summarised in Fig. 1.3(b), we demonstrate the first solid-state single-photon source coupled with a static multiplexing chip for use in random number generation. Crucially, certain mismatches of count rates between different detectors may be inevitable in most real-world scenarios, e.g., due to fabrication limitations, spectrally broad emission lines which affect well-defined coupling

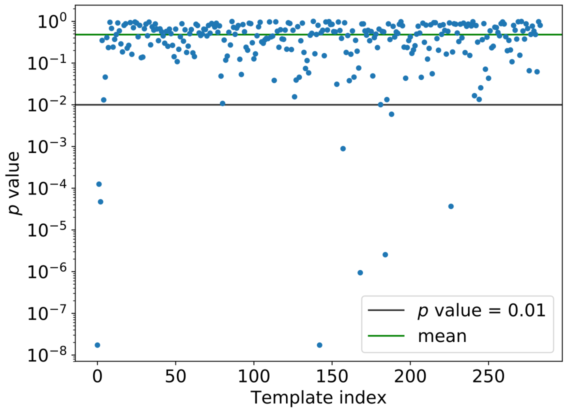

Figure 1.5: Non-overlapping template test results. A binary sequence generated with single photons arrival position from four multiplexed channels is tested with all possible 10 bit templates. An average p-value = 0.48 indicates the sequence is random given α = 0.01

constants, as well as physical differences between detectors. Yet, given the superior brightness of solid-state single-photon sources, these can be easily remedied by selective introduction of appropriate losses in individual channels, and further mitigated by the use of narrow-bandwidth hBN emitters[148,92].

Finally, we also considered the generation of four simultaneous streams of random numbers from a single source, demonstrating the scalability of multiplexing given the limitations of current photodetector technology. With dead times of 22 ns, the single-photon avalanche diodes used have a maximum theoretical flux around 45 MHz. Multiplexing effectively reduces the relative flux using n independent channels. To generate each random binary sequence, each channel is independently analysed, taking the integer photon arrival time in picoseconds modulo 2. The NIST test suite was once more applied, and all four independent channels separately pass the required significance (p-value > 0.01) for all tests, as seen in Figure 1.6. Here we realise two random number generation schemes from a single static device coupled with bright room-temperature single-photon sources. The flexibility of spatial multiplexing is not limited to RNG applications but provides a platform for quantum information processing[149].

1.2.3 Conclusion

In conclusion, we demonstrate on-chip quantum state manipulation and quantum random number generation using photons produced by a room-temperature single-photon emitter based on a 2D material. Using the high brightness of the hBN single photon emitter, we show efficient coupling to an on-chip photonic waveguide structure, allowing us to prepare a spatial superposition state and generate a stream of true quantum random numbers. The compact photonic chip design readily allows for the number of random bits per photon to be increased via the number of involved waveguides far beyond the limitations of bulk-optical arrangements. The on-chip platform can also be readily integrated with commercial optical fibre arrays and other photonic devices. Together with the exceptional brightness and robustness of hBN-based single-photon sources, the system presented here offers an intrinsically stable and readily scalable platform for photonic quantum information processing.

1.3 Summary

In this chapter, a defect in hexagonal boron nitride is introduced as a source of single photons that can be triggered optically via stokes excitation. Here we demonstrate one of the first proof of principle applica-

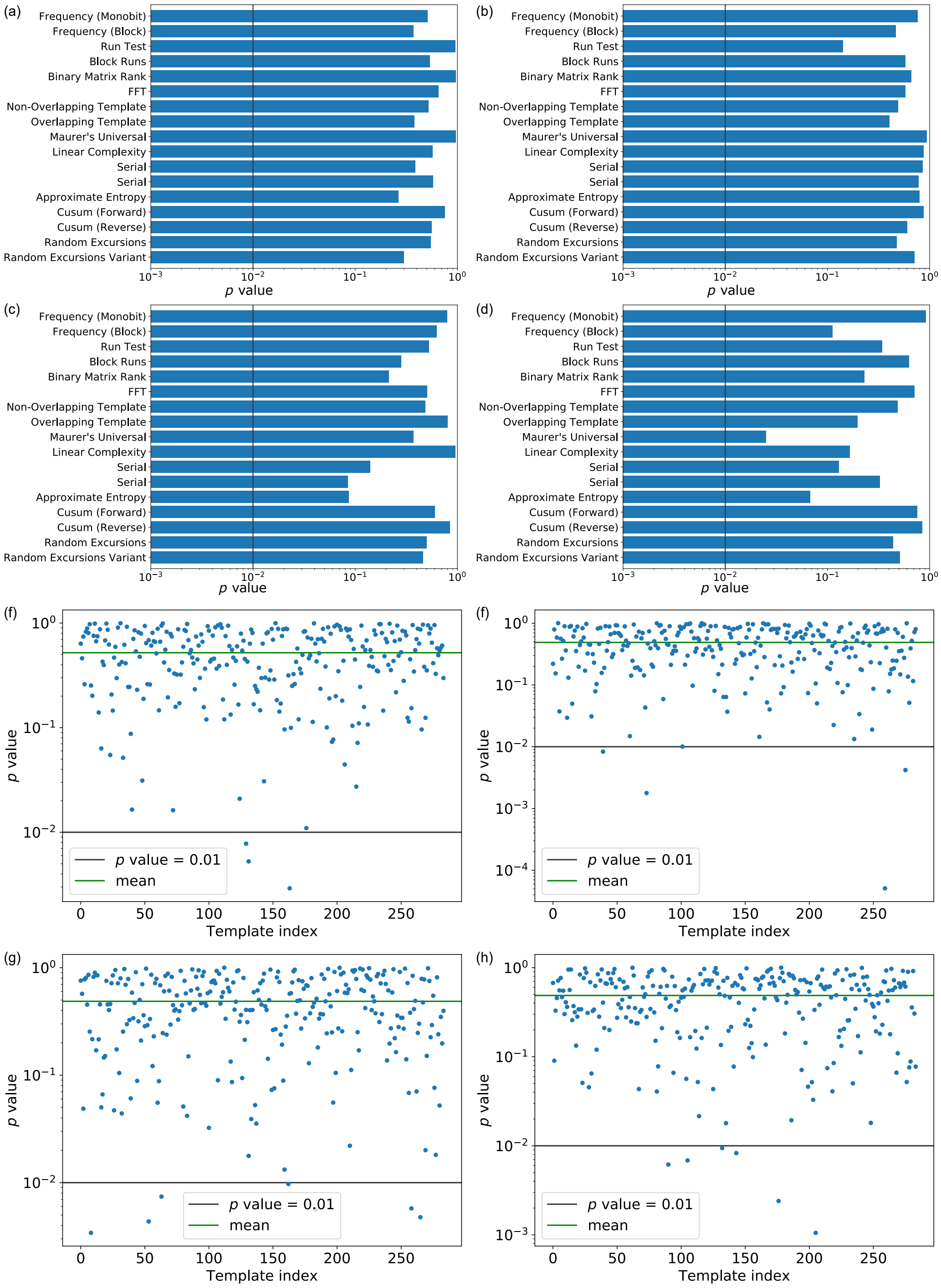

Figure 1.6: NIST test results from four simultaneous streams of random numbers. (a) - (d) NIST test results from binary strings generated from channels 1 – 4 respectively, as p-values are larger than α = 0.01 the sequences can be considered random. (e) - (h) Non-overlapping template test results from simultaneous streams. Four binary sequences are generated using single photons arrival times from four multiplexed channels. The streams are then tested against all 283 ten-bit templates finding average p-values of 0.52, 0.488, 0.487 and 0.487 for channels 1 – 4.

tions of room temperature emission from the solid state Van der Waals material. This application makes use of the exceptional brightness of the hBN emission, and the implementation is relatively insensitive to the relatively broad emission linewidth of hBN single photon emitters at room temperature. At the time of this publication, this was one of the first proof of principle demonstrations with hBN, with other examples including the use of hBN single photons for satellite-based quantum key distribution, and super-resolution microscopy[150,151]. More fundamental studies of temperature sensing capabilities of hBN SPE's have led to a new field of research on nano-scale temperature sensing[88,152,153], and the discovery of spin active emission in hBN from the negatively charged boron vacancy (VB^{-}) is promising for temperature, pressure, and magnetic field quantum sensing[53,52,136,154,155].

Although the room temperature study of hBN emitters garnered significant interest, there has been limited investigation toward their cryogenic properties, and with the considerable expansion of quantum, applications enabled through bright, narrow, and controllable single photon emission, this is the direction I next steered my thesis. In the coming chapters, I discuss exactly this; beginning with the control and enhancement of quantum emission via two laser excitation.

"We explore because we are curious, not because we wish to develop grand views of reality or better widgets."

Brian Cox and Jeff Forshaw, The Quantum Universe:
Everything That Can Happen Does Happen (2011)

2

Optical Repumping of Resonantly Excited Quantum Emitters in Hexagonal Boron Nitride

RESONANT EXCITATION OF SOLID-STATE QUANTUM EMITTERS enables coherent control of quantum states and generation of coherent single photons, which are required for scalable quantum-photonics applications. However, these systems can often decay to one or more intermediate dark states, or spectrally jump, resulting in the lack of emitted photons on resonance. Here we present an optical co-excitation scheme that uses a weak non-resonant laser to reduce transitions to a dark state and amplify the photoluminescence from quantum emitters in hexagonal boron nitride (hBN). Using a two-laser repumping scheme, we achieve optically stable resonance fluorescence of hBN emitters and an overall increase of **on** time of an order of magnitude compared with only resonant excitation. Our results are important for the deployment of atom-like defects in hBN as reliable building blocks for quantum-photonics applications.

2.1 Introduction

Solid-state single-photon emitters that possess narrow emission linewidths are promising for scalable quantum-photonics application[37,127,129]. Specifically, defects in diamond[156], silicon carbide[157], or rare-earth ions in solid-state hosts[158,159] are attracting considerable attention due to their potential use in spin-photon interface architectures[160]. In recent years, single defects in atomically thin materials such as transition-metal dichalcogenides or hexagonal boron nitride (hBN) have been identified[161,162,163]. The hBN quantum emitters possess high brightness at room temperature and often exhibit a high Debye-Waller factor that maximises the emission in the zero-phonon line (ZPL)[164,165,166]. Significant progress has been achieved in performing spectroscopic studies of hBN quantum emitters[167,168,169,141,170,171] and modulating their emission wavelengths using strain or an electric field[93,172,173]. However, under resonant excitation, hBN emitters exhibit blinking and undergo a transition to a metastable state, which often results in a non-radiative decay[137,174,108]. The blinking behaviour of hBN quantum emitters prohibits efficient resonant excitation and coherent manipulation, which is needed for scalable quantum applications. Similar blinking behaviour was also reported for quantum dots[175,176] and some of the colour centres in diamond[152,177]. Indeed, a lot of attention has been devoted to increasing the stability of the main optical transitions under resonant excitation. The methods used include dynamic electric field modulation or active feedback that stabilises the random spectral diffusion of the emitter[176,178], or optical repumping of the optical transition of the selected emitter to avoid relaxation to the dark state[152,177]. In this work, we use a weak non-resonant laser with a wavelength between 500 and 532 nm, in addition to a resonant laser that drives the system coherently to stabilise the optical transition of single defects in hBN. The second laser acts as an additional excitation pathway and re-initialises the system into its bright state. The two-laser re-pumping scheme enables the observation of bright resonant fluorescence with Fourier transform–limited photons emitted from the hBN. We provide an in-depth analysis of the photo-dynamics of the system and discuss its applicability for improved coherence and future photon-indistinguishability measurements.

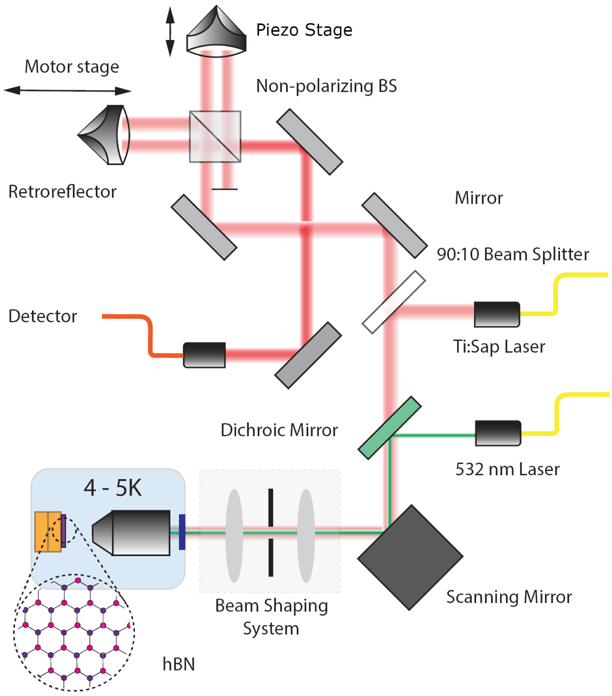

Figure 2.1: The photoluminescence setup with two continuous-wave (cw) excitation sources (532 and 715 nm) and a Michelson interferometer at the collection stage. The sample is mounted inside a closed-loop cryostat, with in built xyz positioning and 0.81 NA objective, and is cooled to ∼4 K

2.2 EXPERIMENTAL WORK

2.2.1 METHODS

The optical measurements are performed with a custom confocal microscope with a Michelson interferometer at the collection stage, as shown in figure 2.1. The sample investigated consists of hBN flakes (Graphene Supermarket) drop-cast on a silicon substrate with 285 nm native oxide, which was annealed at 850 °C for 30 min to activate the emitters. The sample is placed inside a closed-loop liquid-helium-flow cryostat (Attocube Attodry800) and cooled to approximately 4 K. A Ti:sapphire laser (Msquared SolsTiS) with a linewidth of approximately 50 kHz is directed into the objective as an excitation source. In addition, a 532 nm laser (Laser Quantum gem 532) or a tunable laser (NKT Photonics SuperK Fianium) is aligned with the excitation path for co-excitation with the Ti:sapphire (Fig. 2.1). The emission is collected into either a spectrometer or avalanche photodiodes (Excelitas SPCM-AQRH) in a Hanbury Brown–Twiss configuration (fibre-based, not shown). Alternatively, the emission is directed, via free space, to a Mach Zehnder interferometer (MZI) for optical coherence length measurements.

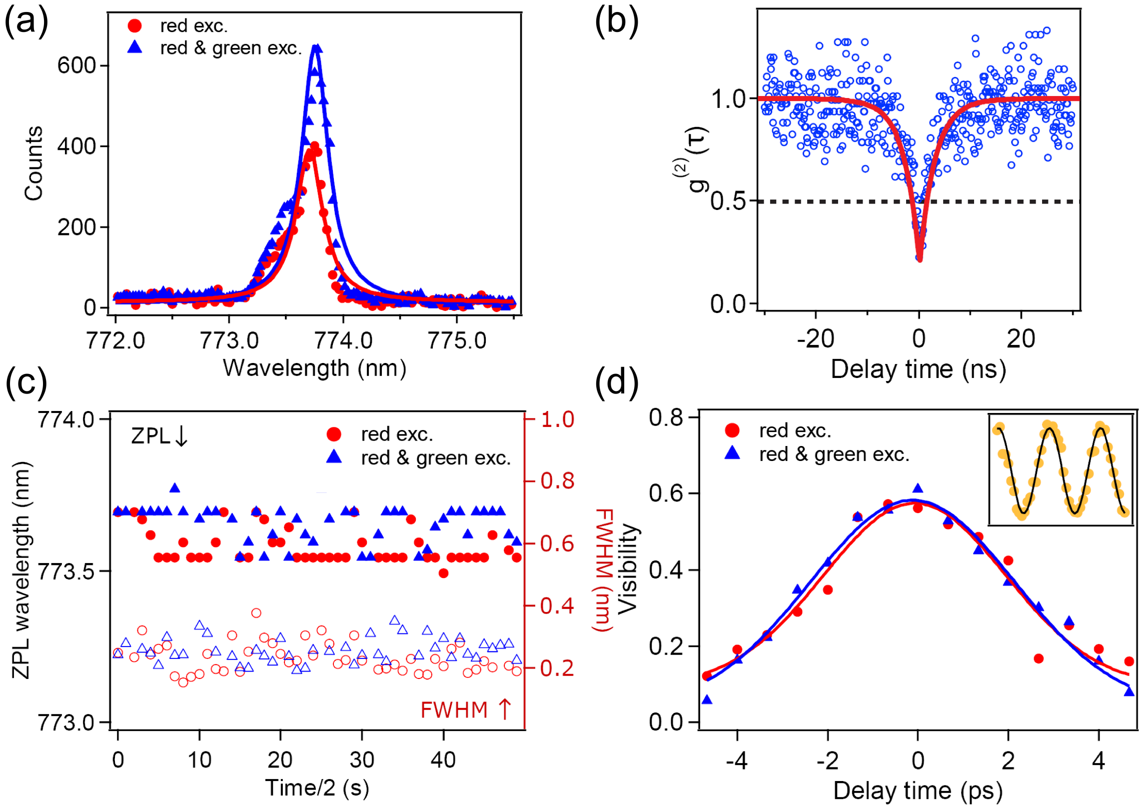

Figure 2.2: Cryogenic photoluminescence measurement. (a) PL spectra of the emitter with 715 nm excitation (red) and repumping with 532 nm (green). The solid lines are Lorentzian fits to the ZPL wavelength, yielding a linewidth of 135 GHz with a small shoulder resulting from a second dim emitter or ZPL wavelength shift resulting from local ionisations or charge fluctuations. (b) Second-order correlation measurement under the repumping condition. (c) PL spectroscopy statistics of the emitter with 715 nm excitation only (red) and with co-excitation with 715 with 532 nm (blue) over a period of 50 s. (d) Coherence-time measurement for red excitation (red circles) and co-excitation with 532 nm (blue triangles). The inset shows an example of intensity oscillation at near-zero-arm-length as the position of the short arm of the MZI is varied.).

2.2.2 RESULTS

We begin with the non-resonant excitation of the system. To investigate the effect of a weak non-resonant laser, we characterise the zero-phonon line (ZPL) wavelength of the emitters with incoherent excitation at 715 nm, as well as with a 532 nm weak non-resonant laser. Figure 2.2(a) shows the photoluminescence (PL) spectra of a selected hBN emitter with a ZPL wavelength of approximately 774 nm under two excitation conditions: (i) 715 nm laser (red trace, 650 µW) and (ii) co-excitation with 715 and 532 nm lasers (green trace, 650 and 60 µW respectively). The PL of the emitter displays a narrow peak with a FWHM of approximately 135 GHz nm and a ZPL at approximately 774 nm derived from a Lorentzian fit to the data. Under excitation with 532 nm (60 µW), there is no detectable fluorescence from this emitter. However, excitation with a 532 nm laser in addition to the 715 nm laser results in an increase of the emission intensity by nearly twofold[151]. The results below are presented for a single selected emitter, though we also observe similar behaviour from other probed emitters. Because of the operation of the Ti:sapphire laser, we limit this study of hBN defects to emitter ZPL wavelengths above 700 nm. Second-order correlation measurement under co-excitation [Fig. 2.2(b)] indicates single-photon antibunching behaviour with $g^{(2)}(0) = 0.23$, without any background correction.

In this work, we focus on how the co-excitation scheme affects the optical coherence properties and blinking dynamics of hBN emitters. Under excitation with only 715 nm [Fig. 2.2(c), red circles] the typical spectral diffusion of the hBN emitters is observed. The spectral diffusion is quantified by observing the ZPL position over time. The ZPL is seen to vary by $\sim$ 0.25 nm and the full-width at half-maximum (FWHM) varies within approximately 22 GHz, over a duration of 50 s. Under co-excitation with an additional green (532 nm) laser, there is no noticeable difference; the emission linewidth and the ZPL wavelength exhibit similar behaviour, as shown by the blue triangles in Fig. 2.2(d). Each spectrum is collected for 2 s and the spectrometer resolution is limited to around 0.08 nm (see A.2.

To further understand the effect of the two-laser co-excitation, we measure the optical coherence time of the emitter under both stokes excitation and co-excitation using the Michelson interferometer depicted in Fig.2.1. For this measurement, the short arm of the interferometer is scanned with a linear piezo stage over two interference fringes using an integration time of 200 ms at each position [Fig. 2.2(d) inset]. The long arm is then extended in increments of approximately 0.1 mm and the short arm scan is repeated. Figure 2.2(d) shows a plot of the coherence visibility; that is, the interferogram for various path differences; acquired for excitation with the 715 nm laser (red trace) or co-excitation with the additional 532 nm laser (blue trace). The interferogram is fitted with a Gaussian model with the centre position set at the position of equal arm lengths to extract the coherence times. The coherence time of 6.8 ± 0.4 ps corresponds to 715 nm excitation and a value of 6.4 ± 0.4 ps was obtained under co-excitation, corresponding to linewidths of approximately 147 and 163 GHz, respectively. Although there is a slight decrease in the coherence time, it is well within the uncertainty of the measurement, albeit lower than the typical coherence values from defects in hBN[179]. Importantly, the comparable values indicate that the spectral diffusion (i.e., the inhomogeneous broadening of the natural linewidth) remains of the same magnitude for both excitation schemes.

We then perform off-resonant photon correlation measurements to gain insight into the photophysical mechanisms behind the observed photoluminescence increase under co-excitation. Figure 2.3(b) shows

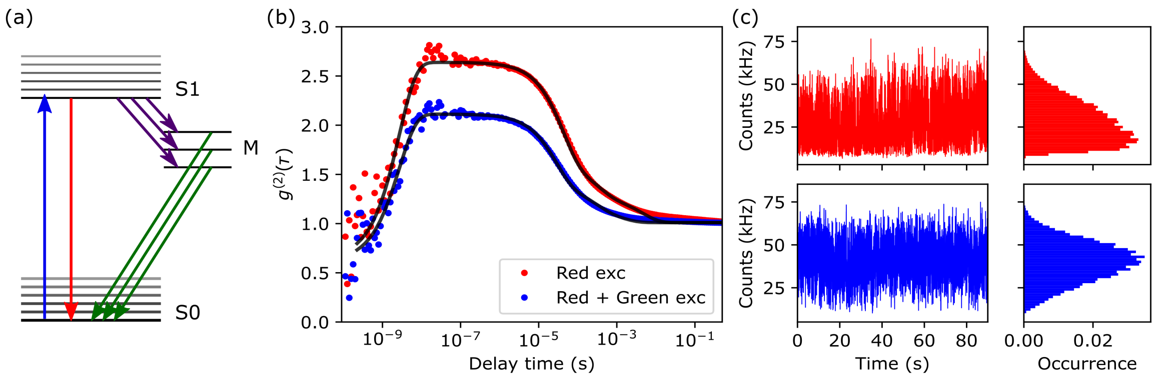

Figure 2.3: Photophysics of a hBN defect under co-excitation. (a) Simplified Jablonksi energy-level diagram. Resonant excitation promotes an electron (blue), which decays either via radiative emission (red) or non-radiatively (green) via intersystem crossings (purple) through a metastable (M; dark) state. (b) Photon correlations showing noticeable intermediate states without co-excitation (red dots) and with co-excitation (blue dots). The black lines are the fitting of the correlation data with a second-order correlation function corresponding to a four-level system. (c) Time trace of avalanche-photodiode counts (bin width of 10 ms) and the corresponding histogram showing the reduction of blinking (50 bins, integration time 1350 s), without (top figures) and with (bottom figures) the co-excitation scheme.

single-photon second-order correlation measurements with excitation at a wavelength of 715 nm and a power of 650 μW (red circles), and co-excitation with a wavelength of 500 nm and a power of 60 μW (blue circles). As expected, the second-order autocorrelation function exhibits antibunching at a short delay time (nanosecond range), evidence that we are observing photoluminescence from a single defect. Extensive bunching at longer delay times (microsecond range) suggests the defect energy-level structure may include multiple metastable states, each with corresponding long non-radiative lifetimes (dark states) as illustrated in Fig. 2.3(a). The best fit to the data is acquired with a model with three long-lived metastable states [Eq. 2.1], which are commonly attributed to additional electronic states, local defects, or to surface-charge traps (dark states)[171,180,165].

$$g^{(2)}(\tau) = 1 - (1 + a_{exc})e^{(-|\tau|/\tau_{exc})} + \sum_{n=1}^{3} a_n e^{(-|\tau|/\tau_n)} \qquad (2.1)$$

The fitting of Eq. 2.1 yields $\tau_1 = 41 \pm 0.65$ μs (27 ± 0.60 μs), $\tau_2 = 0.35 \pm 0.08$ ms (0.26 ± 0.03 ms), and $\tau_3 = 4.5 \pm 1.8$ ms (1.3 ± 0.7 ms) for the single 715 nm laser excitation (and co-excitation respectively). The amplitude of the bunching component of the blue trace (co-excitation) decreases, showing agreement with the enhancement of PL intensity of the emitter with additional excitation with the second laser [Fig. 2.2(a)]. This measurement confirms that in the case of the excitation with only the 715 nm laser, the system spends more time in dark metastable states. Furthermore, photon statistics show the existence of a very fast blinking in the system (on the order of approximately 10 ms). Figure 2.3(c) shows the PL

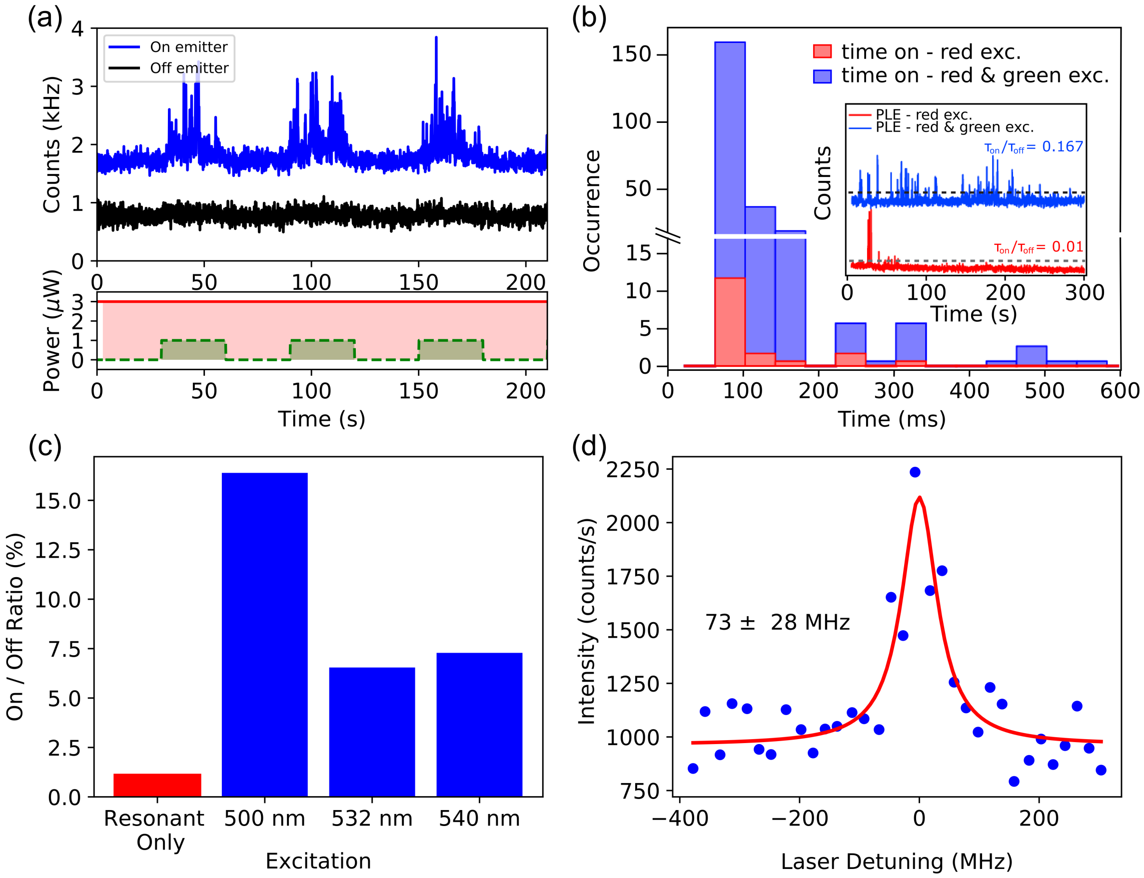

Figure 2.4: Resonant excitation with repumping. (a) Resonant-fluorescence-intensity trace of an optical transition with and without an additional non-resonant repumping laser. The resultant switching PL corresponds to 30 s *on* and *off* durations of the 500 nm laser focused on the emitter (blue trace, offset by 1 kHz) and away from the emitter for reference (black trace). (b) Histogram of on-resonance time with resonant excitation with 1 μW (red bar) and with co-excitation with 1 μW at 500 nm (blue bar). The inset shows the PL-intensity traces for resonant excitation with 1 μW of 500 nm laser repumping (blue) and without repumping (red). (c) Effect of the wavelength of the co-exciting laser, showing the wavelength of 500 nm is the most efficient. (d) Resonant photoluminescence excitation (PLE) with the 500 nm repumping laser showing a near-lifetime-limited linewidth of 73 MHz.

intensity time-trace binned every 10 ms, along with the corresponding histograms on the right-hand side. In the case of the 715 nm excitation, the system undergoes blinking events on the millisecond timescale, which are suppressed by addition of the green co-excitation, as confirmed by the reduced bunching and the improved histogram shown in Fig. 2.3(b).

Leveraging the performance of the emitter under co-excitation (repumping), we now attempt coherent excitation of the emitter. We use the co-excitation scheme to resonantly excite the emitter by tuning a Ti:sapphire tunable laser to the zero phonon line (ZPL). In this scheme the co-excitation is achieved by the combination of the Ti:sapphire laser and a green laser emitting at 500 nm with a power of 1 μW. To minimise laser scattering, we spectrally filter the resonant laser and collect only emission from the phonon sideband, using a long-pass filter at 780 nm. Figure 2.4(a) shows the PL intensity from the emitter under resonant co-excitation with 30 s pulses of the repumping laser over a period of 5 min (blue trace, offset by +1 kHz). This is compared with the same sequence with the lasers focused off the emitter (black trace), to ensure the increased PL is indeed from the emitter. The bottom panel in Fig. 2.4(a) shows the laser sequence. Only when excitation with a green laser is added to the resonant excitation can the emitter be excited and detected. This effect is also completely reversible as shown through repeated excitation conditions. Under resonant excitation only (without repumping), the probability of resonant excitation is very low due to spectral diffusion (spectral jumps due to charge fluctuations around the emitter) or blinking (entering long-lived dark states). Under the additional repumping laser the photoluminescence increases, which corresponds with the decreased probability of entering, and lifetime within, long lived metastable states as outlined above.

Here we also note we do not quantify the rates of the fast spectral diffusion from this emitter as shown by[181]. The affect of repumping on fast spectral-diffusion of emitters in hBN will further elucidate the feasibility of this technique considering applications requiring photon indistinguishability and two photon interference. Though out of the scope of this project we believe this should be considered in future works.

The analysis of photoluminescence intensity using resonant excitation with or without repumping is depicted in Fig. 2.4(b). To define the *on*-resonance and *off*-resonance times (denoted as τ_{on} and τ_{off}), we use threshold values of 1.5 and 2.5 kHz (dashed black lines) for the resonant excitation only and the co-excitation scheme, respectively. In the case of only resonant excitation, the emitter is excited only 1% of the time ($\tau_{on}/\tau_{off} = 0.01$), but when the green repumping excitation is added, the probability increases to more than 15% ($\tau_{on}/\tau_{off} = 0.17$), which is an increase of more than an order of magnitude. Although the probability of the system being on is dramatically higher with co-excitation, the system stays on resonance for a relatively short period of ∼0.1 s. Nevertheless, this is sufficient to generate more than 10^5 photons before the next spectral jump.

We also compare other co-excitation wavelengths, including the most commonly used, 532 nm. We find a strong dependence on the repumping wavelength, and the 500 nm (approximately 2.48 eV) laser works significantly better than the lower-energy lasers with wavelengths of 532 or 540 nm. The 532 nm laser energy of approximately 2.48 eV either corresponds with a charge-transfer threshold of the particular defect or is sufficiently high to charge the nearby traps that would result in a sufficient free-carrier density to be trapped by the quantum emitter. While we cannot distinguish between the two scenarios, the second scenario is more likely since co-excitation only increases the emitter brightness, as is shown for the off-resonant excitation cases (Fig. 2.3). Note that lower co-excitation wavelength (e.g., 480 nm) also shows a reduced repumping efficiency compared with the co-excitation wavelength of 500 nm (not shown).

More importantly, however, each initialisation of the co-excitation cycle results in a flux of photons, while the resonant-laser frequency remains constant. This indicates that the emitter's original ZPL-wavelength position remains the same, without any significant spectral drift. This is vital for the future generation of indistinguishable photons from hBN defects[108]. In this regard, we are able to extract the linewidth of the emitter by scanning the resonant laser over the ZPL wavelength while the green laser is on, as shown in Fig. 2.4(d). The linewidth obtained is 73 ± 28 MHz, corresponding to the Fourier-transform limit of single-photon emitters in hBN with typical lifetimes of a few nanoseconds. This measured linewidth corresponds with the emission of a single spectral jump, with a laser scanning speed of 200 MHz/s. We also note the complete spectral envelope corresponds to the integration over all spectral jumps. Under the green coexcitation, the blinking events (in the millisecond range) are reduced significantly and the probability of resonant excitation is significantly increased. Further reduction of blinking and spectral diffusion is required for some applications in quantum-information processing, and several strategies can be used to increase the stability of single photon emitters based on h-BN; for example, electrical modulation based on p-i-n junctions[182], or use of the dc-Stark-shift effect with an active-feedback loop[183].

2.2.3 CONCLUSION

We demonstrate an effective co-excitation scheme for the resonant excitation of hBN quantum emitters. We show that by applying the two-laser repumping scheme, we can recover emitters from the dark state, resulting in increased resonant photoluminescence. The probability of emission, in this case, is increased by a factor of 15. Importantly, this approach can enhance the brightness of single-photon emitters and can be effectively used to increase the on-resonance time of the emitter. Given the progress with electric field modulation of quantum emitters in hBN, future studies may achieve stabilisation of coherent emission electrically, thus paving the way for on-chip devices. Our work serves as an important step toward the use of hBN quantum emitters for quantum-information applications.

2.3 SUMMARY

In this chapter I study one of the mechanisms that inhibits single photon emission from quantum emitters due to interactions with their environment. Specifically, we attribute this quenching of emission to long lived metastable states that trap the electron in a dark state. We demonstrate that by introducing a weak non-resonant laser, we are able to reduce the lifetime of these dark states, thereby enhancing the emission from the defect. This effect has also been observed in other single photon emitting defects such as the germanium vacancy (GeV) in diamond, where a weak non-resonant laser is also always employed to enhance the quantum emission. Interestingly, the emission from the germanium vacancy maintains its narrow spectral characteristics and it has been shown to produce indistinguishable photons via observing Hong Ou Mandel interference[184]. Observation of the emission enhancement mechanism in hBN is an important stepping stone along the path toward stable coherent emission from hBN SPEs.

In this work we specifically concentrate on increased emission and the photo-dynamics of these emitters under resonant excitation, but have yet to study the spectral characteristics of the emitted photons. To determine whether spectral diffusion is the most significant broadening mechanism, or determine whether other mechanisms are equally significant we look to the next chapter specifically on the dephasing mechanisms of hBN single photon emitters.

”The best that most of us can hope to achieve in physics is simply to misunderstand at a deeper level.”

Wolfgang Pauli to Jagdish Mehra (May 1958)

3

Phonon Broadening

Quantum emitters in hexagonal boron nitride (hBN) are emerging as bright and robust sources of single photons for applications in quantum optics. In this work, we present detailed studies on the limiting factors for achieving Fourier transform limited spectral lines. Specifically, we study phonon dephasing and spectral diffusion of quantum emitters in hBN via resonant excitation spectroscopy at cryogenic temperatures. We show that the linewidths of hBN quantum emitters are phonon broadened, even at 5 K, with typical values of the order of ~ 1 GHz. While spectral diffusion dominates at increasing pump powers, it can be minimised by working well below saturation excitation power. Our results are important for the future utilisation of quantum emitters in hBN for quantum interference experiments.

3.1 INTRODUCTION

Solid state quantum light sources are emerging as promising candidates for many applications in quantum technologies[129,185,186]. Among these sources, optically active point defects in hexagonal boron nitride are attracting considerable attention due to their extreme brightness, and high Debye Waller factor which means the majority of the photons are emitted into the zero phonon line (ZPL)[187,188,189,190,166]. While final defect assignments are still under debate[191], a number of recent experiments and theoretical papers hint at carbon related defects adjacent to a vacancy site in the hBN lattice[133,192]. In addition, numerous recent studies have shown that several defects in hBN exhibit spin dependent optical transitions, and exhibit optically detected magnetic resonance (ODMR), which is vital for their employment as solid state qubits and quantum sensors at the nano-scale[154,193,194].

For practical quantum photonic applications, where photon interference and generations of indistinguishable photons are required[195,196,109,197], it is important to characterise the coherent properties of the emitted photons. Specifically, studies of dephasing mechanisms[198,199], coherence and line broadening effects underpin the applicability of quantum emitters for photon interference experiments. Previous studies of hBN quantum emitters have revealed the emissions in hBN are broadly affected by spectral diffusion[174,108,200,201,202,179,137]. Preliminary resonant excitation experiments showed that observation of Fourier Transform limited lines is possible, but rather rare[137], as compared to other solid state emitters, such as diamond[203,204]. Some of the challenges stemmed from the fact that the level structure of the emitters is still poorly understood, and environmental effects in layered materials are strongly sample-dependent.

In this work, we employ coherent excitation spectroscopy at cryogenic temperatures to study the dephasing of quantum emitters in hBN. Importantly, our work focuses predominantly on coherent excitation (i.e. the excitation laser is on-resonance with the hBN emission). We find that even at low temperatures of 5 K, the lines are predominantly broadened by phonon coupling. We also observe that spectral diffusion can be minimised by employing excitation powers well below the saturation power. We explain our results in the context of electron - phonon coupling and provide an important analysis for future experiments on two photon interference with quantum emitters in hBN.

3.2 Experimental Work

3.2.1 Methods

Sample preparation

The hBN used in this work was exfoliated from high crystal bulk hBN and then transferred to SiO2/Si substrate with PDMS. A pre-annealing of 500C is conducted to remove the transfer residuals. The sample is then etched for 10 min in 900W hydrogen plasma at 60 torr using a microwave plasma deposition system(SEKI AX5100) to create defects on the flake surface. Finally, the sample was annealed for 30 min in a tube furnace (Lindberg/Blue M™) in air.

Optical measurements

The sample was mounted on the cooling stage of an Attocube Attodry800 closed system cryostat, placed under vacuum, and cooled to ~ 4.5 K. Optical measurements were then performed using a custom scanning confocal microscope with a 0.82 NA vacuum compatible objective mounted inside the cryostat (also at 4.5 K). A tunable dye laser (Sirah Matisse 2 DS) with linewidth around 100 kHz was used for resonant excitation, and a 532 nm diode laser (Laser Quantum GEM) was used for off-resonant excitation. For photoluminescence excitation measurements a scan rate of 1 GHz/s was used to tune dye laser wavelength over the ZPL, then the phonon sideband emission from SPE was filtered using a 580 nm long pass filter, coupled via a single mode fibre, and detected using an Avalanche Photodiode (Excelitas SPCM-AQRH). Second order correlation measurements were performed using a fibre beam-splitter and a TimeTagger20, and lifetime measurements were taken using a 40 MHz pulsed 512 nm laser (PiL051X™, Advanced Laser Diode Systems GmbH) and TimeTagger20.

3.2.2 Results

The hBN flakes were mechanically exfoliated onto a silicon substrate from high-purity bulk hBN. The exfoliated hBN flakes were then treated with a H_2 plasma (10 minutes at 900 W, 100 sccm at 60 torr), after which the sample was annealed for 30 min in air at 850°C to remove any residual contaminants from the hBN surface. The sample was then placed under vacuum in a closed looped cryostat and cooled to 5 K.

The main dephasing mechanisms of the hBN emitters are shown in Figure 3.1a. Coupling to lattice

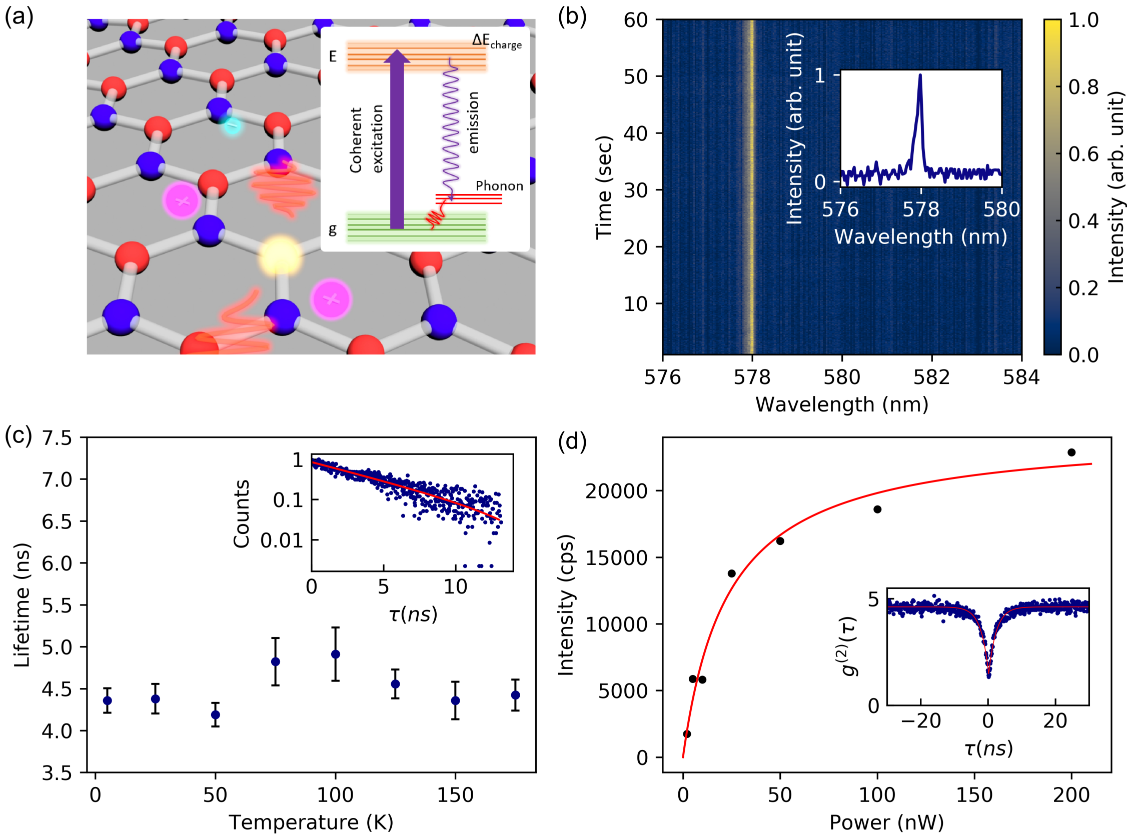

Figure 3.1: Characterisation of hBN single-photon emitters. (a) Schematic representation of the hBN lattice with a point defect (yellow sphere). The emission from the defect is broadened by charge fluctuations and lattice phonons. The inset is a simplified electron energy diagram that illustrates dephasing pathways under resonant excitation. (b) PL spectra of hBN emitters under 532 nm excitation at 5 K. Each spectrum was recorded for 0.1 s. The inset is a single PL spectrum of the same emitter. (c) hBN SPE lifetime showing no significant change versus temperature, under 512 nm pulsed excitation. Error bars are uncertainty of the fit (95% confidence interval). The inset demonstrates a representative lifetime measurement acquired at 5 K. The red line is a single exponential fit of the data. (d) PL saturation measurement of the hBN emitter under resonant excitation. The inset shows a resonant $g^{(2)}(\tau)$ measurement, recorded under 10 nW excitation power.

phonons (phonon dephasing) and random fluctuations of trapped charges in close proximity to the defect (spectral diffusion) are the main dephasing processes for all emitters in solid state hosts, and result in broadening of the emission lines. To investigate a particular defect, we screen for a relatively bright emitter with spectrometer limited linewidth (<0.1 nm). Figure 3.1b shows photoluminescence (PL) spectra of such an hBN emitter at 5 K under 1 mW excitation. The emitter does not exhibit any noticeable spectral diffusion as is illustrated by the time-series of PL spectra collected over a period of 60 s. Next, we used a 512 nm pulsed laser with a repetition rate of 40 MHz to measure the lifetime of the emitter at temperatures in the range of 5 K to 150 K. Figure 1c shows that the emission decay rate is approximately constant over this temperature range. The total decay rate from the excited states, $\gamma = 1/\tau_0 = \gamma_r + \gamma_{nr}$, is, in general, a combination of temperature-independent radiative rate (γ_r), and a non-radiative rate (γ_{nr}) which depends on temperature (T). The dependence of the lifetime on temperature is typically described by the Mott–Seitz model for non-radiative relaxation;

$$\tau(T) = \frac{\tau_0(0)}{1 + ae^{(-\Delta E/k_b T)}} \tag{3.1}$$

Where ΔE is the activation energy, a is the non-radiative relaxation strength parameter, and k_B is the Boltzmann constant[205]. Our results suggest that non-radiative relaxation in hBN is not affected by phonons, at least within this temperature range (Fig. 3.1c). A lifetime of $\tau = 4.4 \pm 0.1$ ns was derived by fitting a single exponential to the data as is shown in the inset of Fig.3.1c. This indicates a Fourier-Transform limited linewidth of ~ 36 MHz at 5 K from this emitter.

We next coherently excited the emitter by tuning a narrowband laser (linewidth < 100 kHz) to the emission energy of the emitter. For this measurement, the emissions into the phonon sideband was collected using a long-pass filter. First, we measured the saturation behaviour of the emitter under resonant excitation as is shown in figure 3.2d. The solid line is a fit to the data with the equation;

$$I = I_{sat}\frac{P}{P + P_{sat}} \tag{3.2}$$

yielding a saturation power of $P_{sat} = 23.4$ nW and saturation intensity of $I_{sat} = 24.5$ kHz for this emitter. We recorded an autocorrelation curve from the emitter under 10 nW excitation power, as shown in the inset of figure 3.1d. We also note, we did not observe Rabi oscillations under excitation powers as high

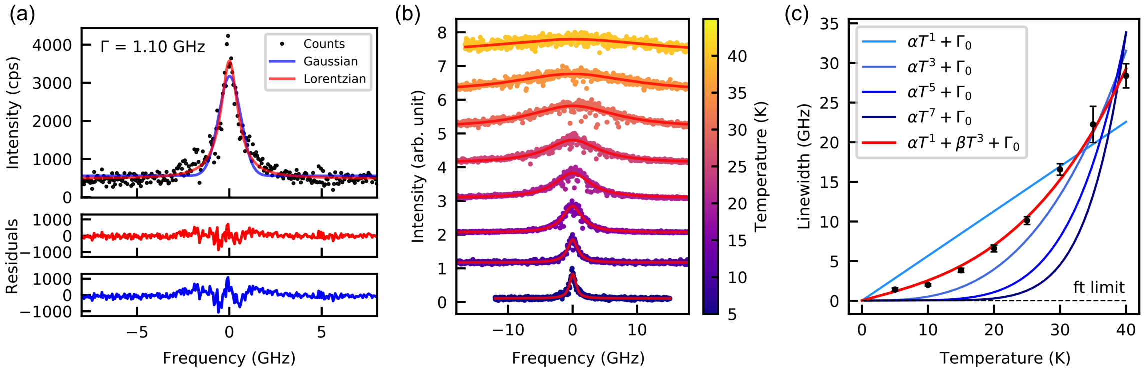

Figure 3.2: Phonon-limited linewidth of hBN SPE. (a) Photoluminescence excitation (PLE) spectrum for hBN single-photon emitter. The linewidth is fit with Gaussian and Lorentzian functions (top), with the corresponding residuals for each fit shown in the bottom panels. The Lorentzian fit is closest to the data and reveals a linewidth (FWHM) of 1.10 ± 0.04 GHz at 5 K. (b) Broadening of the emission linewidth is demonstrated as a function of temperature, due to increased interaction with phonons. Each spectrum is fitted with a Lorentzian function (solid red lines). (c) PLE linewidths (FWHM) as a function of temperature, with an error of 1 standard deviation from each Lorentzian fit. A model (solid red), which is a combination of T^1 and T^3, fits experimental data better than the other higher-order polynomial fits. The fit limit (dash line) is set according to the Fourier transform limited linewidth of 36 MHz.

as 10 μW (i.e. well above saturation), indicating the strong dephasing was faster than the lifetime of the emission[108].

We turn our attention to the characterisation of the dephasing processes of this emitter employing the resonant photoluminescence excitation (PLE) scheme. The PL intensity of the resonant excitation under a pump power of 7 nW is shown in Fig. 3.2a fitted with Gaussian and Lorentzian functions (top part of the plot). The Lorentzian function fits best and has substantially lower residuals compared to the Gaussian fit (Figure 3.2a bottom panels). A Lorentzian shape indicates that the emission linewidth is homogeneously broadened, thus phonons are the dominant broadening mechanism even at 5 K. The full width half maximum (FWHM) of the PLE spectrum, in this case, is 1.10 ± 0.04 GHz, which is significantly broader than the Fourier-Transform limited linewidth of $\sim$ 36 MHz estimated from the lifetime of the same emitter (see Figure 3.1). Given this linewidth we would expect to see around 3% of photons to be emitted coherently, resulting in a rather low probability of observing indistinguishable photons (Hong-Ou-Mandel experiment) would be extremely low. Note that the saturation measurements were recorded using phonon side band collection. Under cross polarisation scheme[206], where ZPL photons can be collected a much higher count rate of coherent photons is expected. Further improvement in the collection of photons from the ZPL could be achieved through coupling the defect to a dielectric cavity.

To explore the phonon-related PLE spectral broadening further, we show PLE spectra collected using a relatively low pump power of 7 nW over a temperature range of 4 to 40 K in Figure 3.2b. The emis-

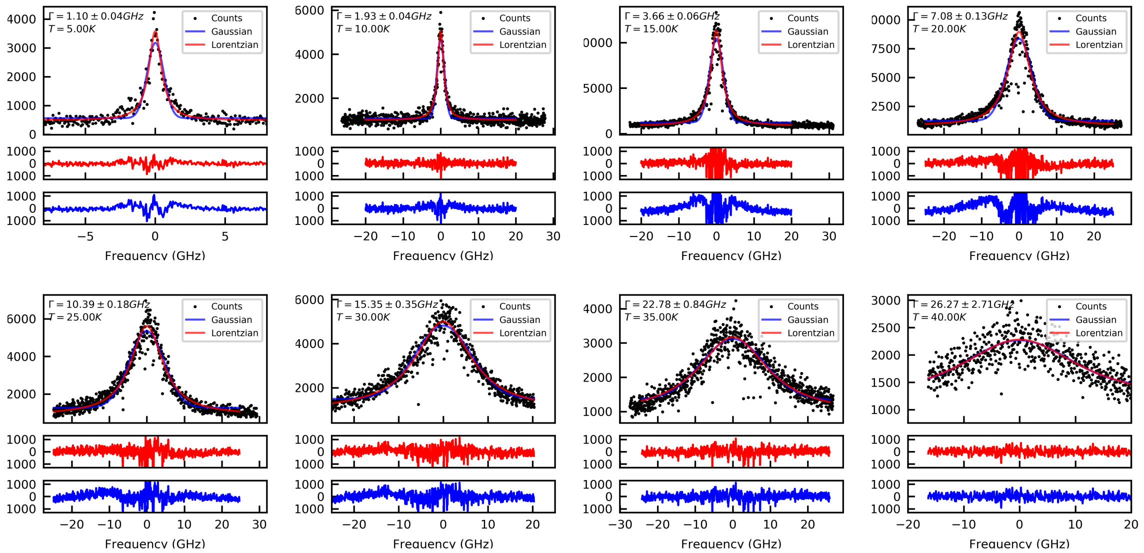

Figure 3.3: Lorentzian vs. Gaussian fitting of PLE spectrum. Each PLE spectrum between 5 and 40 K is fit with both Lorentzian and Gaussian functions. For all cases the residuals are smaller for the Lorentzian fit indicating there is no significant change in spectral diffusion, due to heating, over this range.

sion linewidth increases dramatically as the temperature rises, reaching nearly 30 GHz at 40 K, due to an increase in the interaction rate with phonons. We also note that phonon broadening remains the dominant broadening mechanism over this entire temperature range, which we attribute to the relatively small change in thermal energy up to 40 K. This small change in thermal energy has a weak effect on spectral diffusion. As expected, each individual PLE spectrum shows a better fit with a Lorentzian function, as shown in Figure 3.3.

In Figure3.2c, we plot the PLE linewidth (full width at half maximum) against the sample temperature, and fit the data with aT^1, aT^3, aT^5, aT^7 and $aT + bT^3$ curves[205,207,208]. As can be seen from the fits, higher order polynomials do not describe the data as well as $aT + bT^3$. Close to absolute zero, the dependence of the linewidth on the temperature is expected to be linear as a first-order approximation[209]. Since we are performing the measurements in the intermediate temperature range, a polynomial fit $aT + bT^3$ corresponds to the appropriate model. Above 20 K the linewidth scales as the cube of the temperature $\Gamma = (36 + 0.32 \pm 0.02 \cdot T^3)$ MHz. For low temperatures ($<$ 20 K), the behaviour deviates from T^3 and is better approximated by a linear dependence on temperature $\Gamma = (36 + 220 \pm 29 \cdot T)$ MHz. To speculate about the type of the observed electron-phonon interactions and its relation to strain, we note that for defects under the strain that is larger than the spin-orbit interaction, the orbital eigenstates no longer have well defined angular momentum. In that case, the inelastic Raman process results in a com-

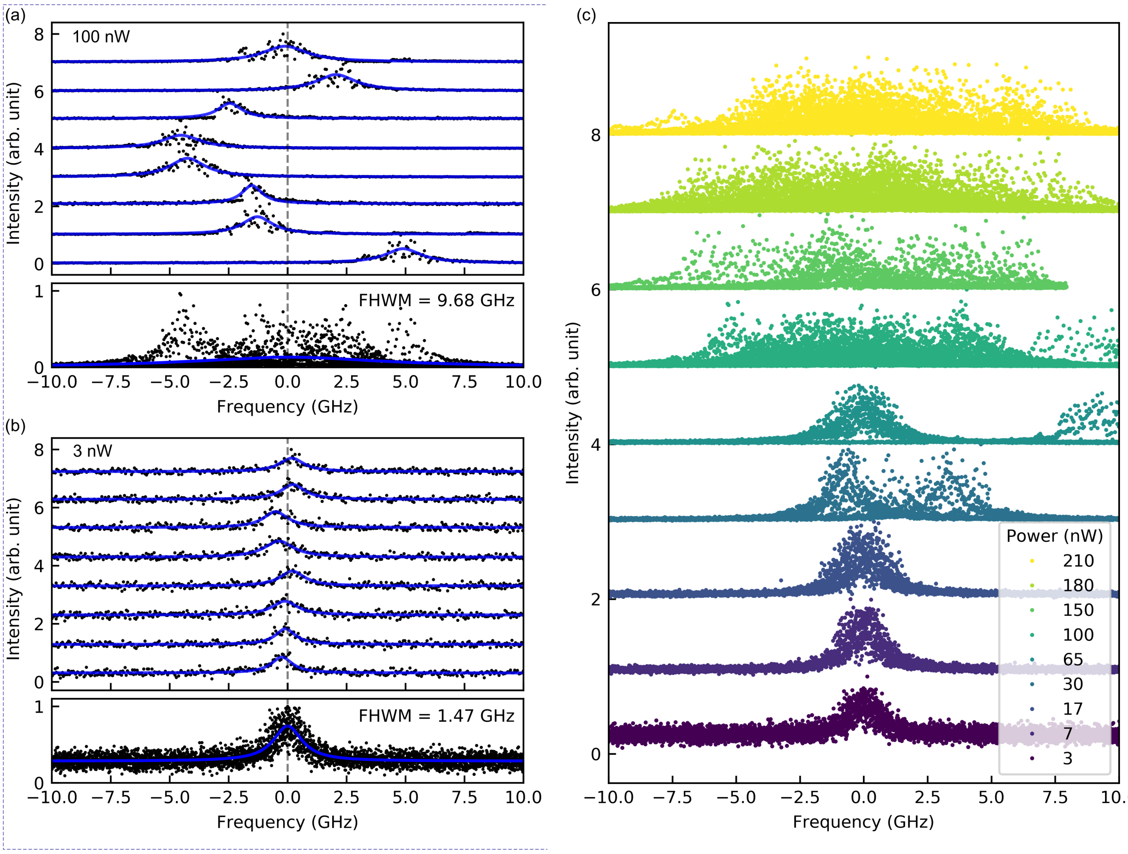

Figure 3.4: Power-dependent spectral diffusion characterised by resonant photoluminescence spectroscopy. (a) Individual PLE scans at a pump power of 100 nW (top) and the corresponding integrated PLE spectrum (bottom) showing significant spectral diffusion. (b) Individual PLE scans at a pump power of 3 nW (top) and the corresponding integrated PLE spectrum (bottom) showing negligible diffusion (c) Integrated PLE spectra at pump powers in the range of 3 to 210 nW, showing that the integrated linewidth increases with pump power.

peting orbital relaxation rate and the corresponding linewidth dependence on temperature that scales as $\sim T^5$, which is not observed in our measurements of hBN defects. The fits with higher-order polynomials T^5 and T^7 do not match our data well which indicates that in our system, degenerate electronic states are not dominant, the Jahn-Teller effect is small, the effect of strain is low, and the inelastic Raman process is not prominent[205,210,211]. When it comes to the type of phonons in the electron-phonon interactions, the linear component of the linewidth temperature dependence corresponds to the first-order transition between the orbital states and the absorption or emission of a single phonon, while T^3 dependence related to a two-phonon elastic scattering dephasing process. This phonon broadening effect indicates that further cooling (below 5 K) would enable further narrowing and may enable Fourier-Transform limited linewidth for such SPEs in hBN. Note, that unlike the situation with single molecules[198], where low energy phonons are visible and present as sharp spectral lines, hBN defects do not exhibit this phenomenon, at least at 5 K. Hence the phonons are likely a mixture of bulk and acoustic phonons within the hBN lattice.

Next, we explore the dependence of the PLE emission as a function of pump power at 5 K to evaluate spectral diffusion of the emitter. Figure 3.4a shows a series of eight individual scans at pump power of 100 nW, and as observed by the change in peak location this power results in a significant spectral diffusion. At the bottom of Figure 3.4a, the integrated spectrum is shown and has a broadened linewidth of $\sim$ 10 GHz. On the other hand, Figure 3.4b shows when the power is reduced to 3 nW the spectral diffusion is significantly reduced to the sub-GHz level.

This measurement is consistent with the temperature-dependent measurements which show that the linewidth, at a pump power of 7 nW, is broadened due primarily to interactions with phonons and to a lesser extent by spectral diffusion. Interestingly, we also note that the linewidth for individual scans maintains a similar linewidth to the low power scans ($\sim$ 1 GHz) signifying the dominant broadening mechanism of the line is still homogeneous. This also opens the possibility that active field modulation, post-selection techniques or charge depletion may play a role in enabling bright coherent emission from such an hBN source. By efficient decoupling of the emitter from its local environment, one could avoid spectral diffusion and enable high power excitation and emission[178,182,212].

To reveal the full spectral diffusion behaviour of the emitter, we recorded a number of PLE scans using excitation powers from 3 to 210 nW, as shown in Figure 3.4c. Spectral diffusion is seen to significantly increase at a transition power around 30 - 65 nW, corresponding with the saturation power, above which stable coherent excitation becomes difficult. These results demonstrate that to use such hBN emitters for quantum interference and enable viable levels of indistinguishability between consecutive photons, it is essential to use excitation powers below saturation and/or lower temperatures.

3.2.3 CONCLUSION

To summarise, in this study we characterise the significant dephasing and spectral broadening mechanisms in an hBN single photon emitter under resonant excitation. We find that the resonant linewidth, even at cryogenic temperatures, is dominated by phonon broadening and results in linewidths of $\sim$ 1 GHz. As we heat the sample, the linewidth broadens with a $aT + bT^3$ relationship indicating that degenerate electronic states and strong strain do not appear to play a significant role in phonon dephasing. We further showed that spectral diffusion can be minimised by employing excitation powers well below saturation.

3.3 SUMMARY

This work opens exciting opportunities for quantum interference experiments with defects in hBN. Development of cross polarisation schemes to collect ZPL photons should be implemented using waveguide structures[213,214,215,163]. This is certainly within reach with the currently available nano-fabrication techniques and will enable substantially more coherent photons. Our results also infer that extended cooling below 5 K can enable further narrowing of the spectral linewidth and may enable an approach to generate indistinguishable photons on demand. Finally, established tuning techniques[172,173] can be utilised to not only stabilise spectral diffusion but tune two distinct hBN emitters into the same resonance, thus paving the way to generate remote indistinguishable photons.

πάθει μάθος

"páthei máthos" - (There is) learning in suffering/experience

Aeschylus, Agamemnon, 177

4

Electrical Control of Quantum Emitters in a Van der Waals Heterostructure

CONTROLLING AND MANIPULATING individual quantum systems in solids underpins the growing interest in the development of scalable quantum technologies. Recently, hexagonal boron nitride (hBN) has garnered significant attention in quantum photonic applications due to its ability to host optically stable quantum emitters. However, the large band gap of hBN and the lack of efficient doping inhibits electrical triggering and limits opportunities to study the electrical control of emitters. Here, we show an approach to electrically modulate quantum emitters in an hBN–graphene van der Waals heterostructure. We show that quantum emitters in hBN can be reversibly activated and modulated by applying a bias across the device. Notably, a significant number of quantum emitters are intrinsically dark and become optically active at non-zero voltages. To explain the results, we provide a heuristic electrostatic model of this unique behaviour. Finally, employing these devices we demonstrate a nearly-coherent source with linewidths of ≈160 MHz. Our results enhance the potential of hBN for tuneable solid-state quantum emitters for the growing field of quantum information science.

4.1 INTRODUCTION

Van der Waals (vdW) heterostructures have emerged as a fascinating platform to study light-matter interaction at the nanoscale[216,217,218,219]. Assembling various atomically thin crystals has enabled the observation of new physical phenomena in these unconventional materials, including superconductivity[220], interlayer excitons[221], moire lattices[216,222], and correlated electronic systems[223]. Furthermore, advanced practical devices such as broadband photodetectors, efficient light-emitting diodes, and nanoscale lasers have also been realised from a variety of vdW crystals[224]. Indeed, control over light emission from a selected family of transition metal di-chalcogenides enabled optical detection of valley states, and observation of exciton-polariton condensates even at room temperature[225,226,227,228]. Of particular interest is the ability to manipulate light emission from single point defects, commonly referred to as single-photon emitters (SPEs), as they are critical building blocks for quantum technologies[186,185]. Hexagonal boron nitride (hBN), a wide band gap vdW crystal, has been extensively studied in recent years as a vdW host of SPEs that are ultra-bright and optically stable[133,229,230,96,108]. In addition, hBN SPEs exhibit spin–photon interface and can be engineered on-demand in an atomically thin crystal[154,193]. This combination of photophysical properties foreshadows ample opportunities for their utilisation as quantum sources and quantum repeaters in scalable quantum photonic devices. An outstanding challenge for solid-state SPEs is to realise electrical control of the optical emission. This challenge stems from the fact that most hosts of defect-based SPEs are wide band gap materials in which p-type or n-type doping is limited[231,232]. Indeed, even for well-studied materials such as diamond or silicon carbide, electrical modulation of quantum emitters is limited to specific defects and often requires cumbersome device engineering[233,234,182,235].

Here we demonstrate a facile and scalable approach to electrically modulate quantum emitters in hBN – graphene heterostructures. Our experiments show that single photon emitters in hBN can be activated and modulated by applying a voltage across the devices. Intriguingly, we show that most of the quantum emitters become optically active at non-zero voltages, in contrast to what has been observed in the case of defects in 3D crystals. We interpret our results in the context of electrically-induced changes in the charge states of the hBN defects and provide electrostatic models to support the experimental findings.

4.2 Experimental Work

4.2.1 Methods

We begin by introducing the methods used to fabricate, measure and simulate a structure used to electrically modulate the photoluminscance from single photon emitters in hBN.

Preparation of hBN flakes

The hBN flakes are mechanically exfoliated onto 285 nm and 90 nm SiO2/Si substrates with Scotch tape from ultra high-purity bulk hBN crystals (carbon and oxygen impurity concentrations of $< 10 * 18cm^{-3}$). The hBN crystals are synthesised using a HPHT process (high pressure high temperature of 4.5 GPa and 1500 °C respectively). The tape residuals on the flakes are removed through a 4-hour calcination process in air at 500 °C using a hot plate. The single photon emtiters are activated/generated using a hydrogen plasma process. The plasma process is performed in a microwave plasma deposition system (SEKI AX5100). The exfoliated hBN flakes are placed on a graphite puck and then the chamber is pumped down to 1×10^{-2} torr. After purging with argon for 10 minutes, 100 sccm H_2 is induced and the chamber pressure is gradually increased to 60 Torr. The plasma power is set to 900 W, and hBN samples are treated for 3 minutes. Following this, a 40-minute high-temperature (700 °C) annealing process is conducted in a tube furnace (Lindberg/Blue) in air, at a ramp heating rate of 120 °C/min. The samples are cooled to room temperature naturally (normally takes 2-3 hours to cool down to room temperature). After this, the UV ozone cleaning process is conducted in a UV ozone generator (ProCleaner™ Plus, Bioforce Nanosciences Inc.)

After the plasma treatment, the desired hBN flake on Si/SiO2 substrate is identified using a home-built scanning confocal PL microscope. The heterostructures are fabricated using an aligned transfer technique using polyvinyl alcohol (PVA) coated polydimethylsiloxane (PDMS) as a stamp. The gold electrodes of 5 nm Cr and 100 nm gold were fabricated using standard aligned photolithography and vacuum thermal deposition.

PHOTOLUMINESCENCE SPECTROSCOPY

The PL spectra were collected with a custom-built scanning confocal microscope. The samples were excited with a 300 μW 532 nm continuous-wave (CW) laser. The laser reflection was filtered spectrally using a 532 nm dichroic mirror. Low-temperature optical measurements were performed using a similar confocal system with the sample mounted on the cold finger within an attoDRY800 cryostat (operating at 4 K). The emissions are collected with the spectrometer for spectra or two avalanche photodiodes (APDs) for photon counting. The second-order auto-correlation ($g^2(\tau)$) measurements are conducted with a time-correlated single-photon counting module (Swabian, TimeTagger20) in a fibre-based Hanbury Brown-Twiss configuration with two APDs. Further information is detailed in the introduction (0.6).

THEORETICAL CALCULATIONS

Theoretical calculations reflect the linear drop of an electric field across a classical capacitance assuming all charge builds up at the contacts, i.e. V/t. To ensure the limited density of states of the non-metallic contacts were not significantly altering the classic capacitor behaviour, a nonlinear Poisson equation was solved for both contacts assuming parabolic bands. Band diagrams reflect the band alignment from biasing the capacitance formed between a heavily doped p-type silicon (work function $\Phi \sim 5$ eV) and a 10 nm thick layer of graphite ($\Phi \sim 4.6$ eV). For simplicity a dielectric constant of 3.6 is used for both the hBN and SiO_2, the electron affinity hBN is 2.3 eV and SiO_2 is 0.9 eV[236,237]. Band bending effects of charge build-up in the non-metallic contacts were considered for both the graphite and Si contacts by numerically solving the classic one-dimensional Poisson equation with a Newton Raphson method provided by the diamond-banalyzer python package (https://pypi.org/project/diamond-bandalyzer/), although only resulted in $\sim$ 0.2 eV shifts at 20 V, and thus were ignored.

4.2.2 RESULTS

A schematic illustration of the heterostructure devices used in this study is shown in Figure 4.1a. The device structure consists of multilayer graphene (MLG), a hBN capping layer, and a hBN emitter layer stacked vertically on p-type silicon with a 285 nm thermal oxide. Bias is applied between the bottom p-type silicon and MLG. An optical image of the device is shown in Figure 4.1b. The black, light blue, and green dashed lines indicate the boundaries of the MLG, the hBN capping layer, and the hBN layer that

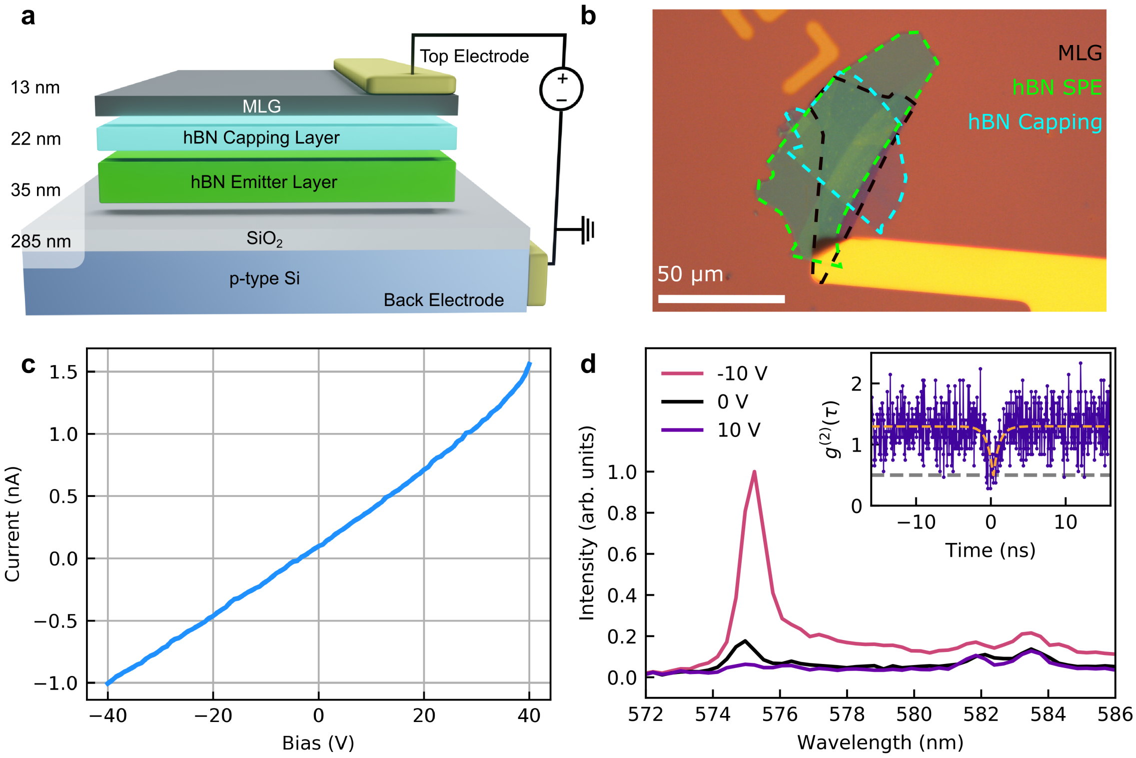

Figure 4.1: The hBN/MLG heterostructure device. a. Schematic of the device and its operating principle. The device is biased using gold electrodes in contact with MLG and p-type silicon. Layer thicknesses are indicated on the left. b. Optical image of a device consisting of MLG, a hBN capping layer, and a hBN layer that contains SPEs. The substrate is bulk p-type silicon with a 285 nm thermal oxide layer. Each layer is outlined by dashed lines. c. I-V curve from the device shows a negligible leakage current. d. Normalised PL spectra of a fluorescence peak at 575 nm from the heterostructure under a bias of -10 V (red), 0 V (black), and 10 V (violet), at 4 K. Inset: Second autocorrelation data measured from the same emitter under -10 V bias, at 4 K. The PL was filtered using a tuneable band pass filter centred at 575 ± 2 nm and the fit (dashed yellow) reveals $g^{(2)}(0) = 0.48$.

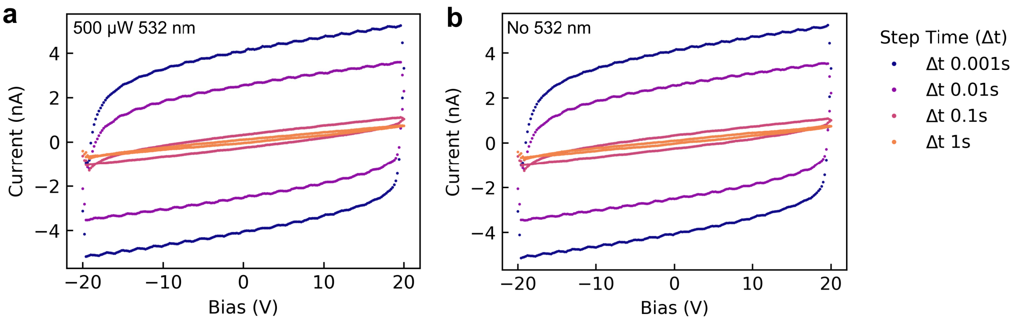

Figure 4.2: I-V characteristics of hBN/MLG heterostructure with 285 nm thermal silicon oxide layer. a. Current vs. voltage curves for voltage step time of 0.001 to 1s with 532 nm laser excitation on the heterostructure. b. Current vs. voltage curves for voltage step time of 0.001 to 1s without 532 nm laser excitation (dark) on the heterostructure.

hosts the quantum emitters, respectively. The capping layer (≈ 20 nm) is used to prevent quenching of emitters in the active hBN layer by MLG[238,229]. Details of the fabrication process can be found in the methods section above.

To characterise the device, we first measured a current-voltage (I-V) curve by sweeping the bias from -40 V to 40 V. The current scales linearly with voltage, as shown in Figure 4.1c, and the maximum measured current is less than 1.5 nA. This is an upper bound on the current through the hBN layers since the top electrode is in contact with both the MLG and the oxide layer. The I-V curve shows that the device behaves as a capacitor that generates an electric field within the hBN layers.Next, we study the optical properties of quantum emitters embedded in the heterostructure. Almost all optical measurements were performed using a 532 nm continuous-wave excitation laser, and a custom-built confocal microscope (see methods for details). The hBN/MLG heterostructure device was loaded into a closed cycle He cryostat operating at 4 K. Figure 4.1d shows photoluminescence (PL) spectra from one emitter at 4 K, using a bias of -10 V (red curve), 0 V (black curve) and 10 V (violet curve). Remarkably, a clear peak at 575 nm arises when the voltage is switched from 10 V to 0 V and increased further at -10 V as shown in Figure 4.1d, indicating activation of the emitter by the applied bias. After filtering the emission peak at 575 nm using a 575±2 nm band-pass filter, second-order correlation measurements were performed. The inset shown in Figure 4.1d reveals a dip at zero delay, $g^{(2)}(0) = 0.48$, indicating the presence of non-classical emission which we attribute to a single quantum emitter with some background PL. Here we note that as the background PL also varies with the applied bias, no background correction was used for $g^{(2)}(0)$ measurements, thus the $g^{(2)}(0)$ value represents an upper bound for these emitters (detailed below in Figure 4.4).

We further confirm the electrical response from the device as shown in Figure 4.2. We perform voltage

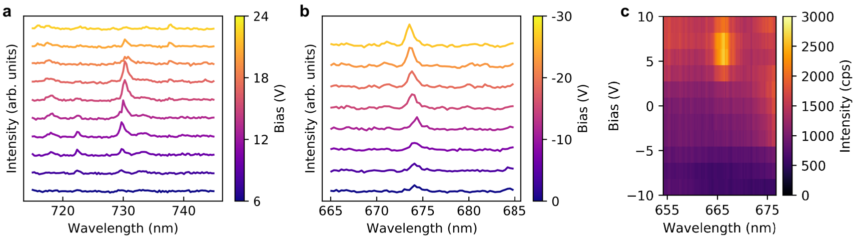

Figure 4.3: Photoluminescence emission lines response to bias. a, b. Normalised PL spectra of two different emitters at a positive bias of 6 V to 24 V (a) and negative bias of 0 V to -30 V (b), respectively. c. Room-temperature PL spectra recorded over a bias range of -10 V to 10 V displaying activation of a 667 nm emission peak at 7 V.

sweeps from -20 V to +20 V and back to -20 V with differing step times (Δt) and 0.4 V steps. As seen in Figure 4.2a and b, there is no significant photocurrent in the hBN/MLG heterostructure, i.e. the laser excitation does not significantly affect the global charge transfer mechanisms. The leakage current is also negligible under short time scales (voltage step time Δt = 0.001 s, leakage current < 5 nA), and this reduces further over time. Interestingly, the device also shows a strong capacitive behaviour when the bias is applied on time scales less than 0.1s. We note here, the charging behaviour cannot be isolated to only the hBN/MLG interface and is likely also contributed to by the Si/electrode, MLG electrode interfaces, and also the SiO2/electrode interface, as the electrode is not confined only to the graphene as seen in Figure 4.1b.

Additionally, we demonstrate the switching phenomenon is common among many emission peaks from in this device as shown in the cryogenic spectra in Figure 4.3. Activation of emission is clearly displayed under positive and negative bias. In Figure 4.3a peak at 730 nm is activated at ~ 8 V and continues to increase in intensity to ~17 V, the dims above 22 V (each spectra is vertically offset for clarity). Figure 4.3b displays an emission peak at 674 nm which intensity increases monotonically as the bias drops from 0 V to -30 V. The switching behaviour is persists also at room temperature, as seen in Figure 4.3c.

Further analysis of the emitter shown in Figure 4.1d is shown in Figure 4.4. A narrow PL peak is observed at 575 nm, which responds strongly to the influence of an applied bias. Under a +10 V bias, the PL is completely quenched, whereas under a -10 V bias, the PL increases significantly. To determine whether the PL is from a single emitter, second order correlation data is recorded using a fibre based Hanbury-Brown and Twiss interferometer, and a tuneable filter to create a bandpass of 575 ±2 nm. The data was fit with the model for a two level system with an aditional metastable state (3 levels), detailed in appedix section AA.1 Long time scale correlations (Figure 4.4d) reveal bunching from the emitter due to an additional metastable state (bunching amplitude $A_m = 0.3$ and lifetime τ_m =1.3 µs). Short time scale correlations

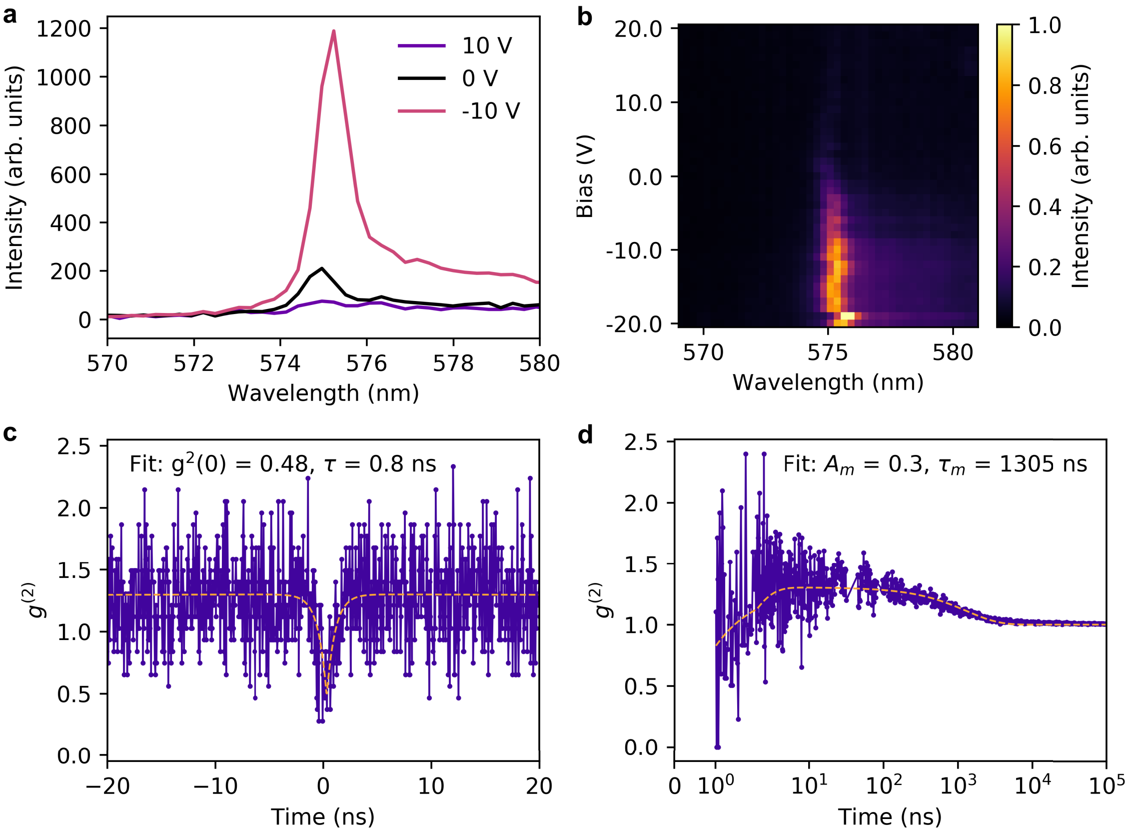

Figure 4.4: Emitter PL and second order correlation for an emitter activated under a bias. a. Cryogenic PL spectra of an emitter in the heterostructure under a bias of -10 V (red), 0 V (black) and 10 V (purple), with 300 µW 532 nm excitation. b. Series of normalised PL spectra recorded over a bias range of -20 V to 20 V. c. Short time scale second autocorrelation data measured from the same emitter under -10 V bias (purple). The PL was filtered using a tuneable bandpass filter centred at 575 ± 2 nm and the fit (dashed yellow) reveals g(2)(0) = 0.48, without background correction. d. Long time scale second autocorrelation data between 1 ns and 0.1 ms revealing bunching due to an additional metastable state. .

reveal a dip with $g(2)(0) = 0.48 \pm 0.12$, and an excited state lifetime of $\tau = 0.77 \pm 0.16$ ns, as shown in Figure 4.4c. Measurements are not background corrected as the background PL changes as a function of bias due to the high density of emission lines. This results in the fit $g(2)(0)$ representing an upper bound for the emitter.

The electrical control of the hBN emitters is shown in Figure 4.5. The bias dependence of PL spectra from two emitters is plotted in Figures 4.5a and 4.5b. The spectra, normalised for clarity, illustrate two distinct behaviours observed predominantly under positive (Figure 4.5a) and negative (Figure 4.5b) bias applied to the MLG electrode. The emitter in Figure 4.5a does not fluoresce at zero bias. However, as the bias is increased, the emitter becomes active around 8 V, and increases in brightness up to ≈15 V where it goes through a maximum and then decreases as the bias is increased further. It becomes inactive at ≈22 V and is not returning to its optically active state as higher bias is applied (within our experimental limitations). On the other hand, the emitter in Figure 4.5b shows completely different behaviour. As the bias is reduced from 0V to - 30V, the emission intensity increases gradually and remains optically active even under - 30V. This is unexpected, given that under positive biases, there was only a window of voltages under which the emission was persistent. This is explained later in detail, and corresponds well to our proposed model. Note, that in both cases, a minor shift of the emission was observed, as expected, due to the Stark shift[173,172]. The direction of the Stark shifts depends on the polarity of the applied bias and the dipole orientation of each emitter.

The emission intensity can be further tuned dynamically with the applied bias. This is shown in Figure 4.5c, where an emitter is modulated using a square wave voltage function, oscillating between 0 and +10 V. The period of the intensity modulation resembles the square wave bias function, illustrating the repeatability of the activation process - the switching is reversible and repeatable. Similar behaviour was also observed for emitters activated by a negative bias, and is discussed below.

A detailed analysis of the switching rates is presented in Figure 4.5d-g. The time-correlated intensity was recorded using a time tagger (Swabian instrument, jitter of < 200 ps) whilst bias step functions were applied to the device. Figure 4.5d,e shows the PL rise and decay times when a bias of +10 V was turned on and off, respectively. The curves were fitted with single exponential functions and the rise (τ_{on}) and fall times (τ_{off}) were found to be 86 and 40 µs, respectively. The rise time is ≈ 2000 times slower than the fall time, indicating significant differences between the charging and discharging dynamics[239].

The corresponding measurements obtained using a negative bias of -10 V are shown in Figure 4.5f-g.

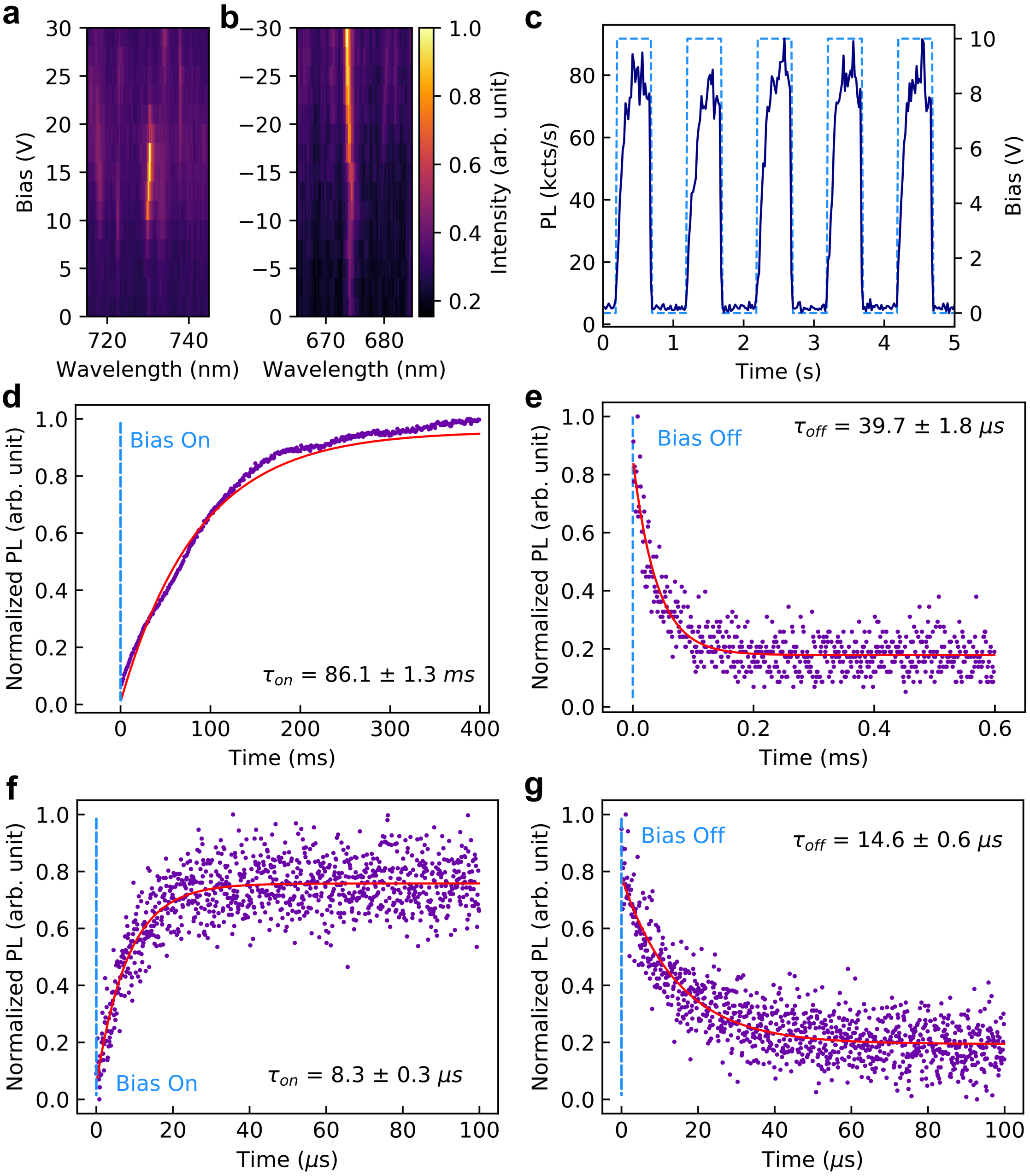

Figure 4.5: Electrical control of hBN emitters in the heterostructure device. a, b. Normalised PL spectra recorded from two different emitters as the bias applied to MLG varied from 0 V to +30 V (a), and -30 V (b). c. Dynamic modulation of the emission intensity of an emitter by a square wave bias function. The bias is switched periodically between 0 V and +10 V, as shown by the light blue trace. The filtered PL signal intensity detected by an avalanche photodiode (APD) is plotted in dark blue. d, e. Normalised PL intensity versus time, showing the emission dynamics when the emitter is turned on (d) and off (e) by a +10 V step function applied to the MLG electrode. The measured data are fitted with single exponential functions, and the time constants, τon, and τoff are 86 ms and 40 µs, respectively. f, g. Corresponding dynamics from an emitter that becomes active under negative bias, measured by applying a -10 V step function to the MLG electrode. Under negative bias, τon and τoff are 8 µs and 15 µs, respectively

Under negative bias, τ_{on} and τ_{off} are comparable, approximately 8 µs and 15 µs, respectively. Strikingly, the rise time under negative bias is over four orders of magnitude faster than under the positive bias, whilst the fall times are similar under both positive and negative bias. The dramatic difference between the rise times is indicative of distinct emitter activation mechanisms under positive and negative bias, as is discussed in detail below.

To provide a broad, statistically-representative overview of the behaviour of emitters under applied bias, we recorded PL spectra from a large ensemble of emitters within the area of a single excitation laser spot. The spectra recorded as a function of bias over the range of -40 V to +40 V is shown in Figure 4.6a, where each emission line corresponds to an emitter in hBN. The lines at 580 nm (620 nm) are the G (2D) bands of MLG and remain unchanged (at this particular spectrometer resolution using a 300 lines/mm grating)[229]. A large number of emitters spanning a broad range of emission wavelengths are activated when a positive bias is applied to the MLG electrode, mostly above +10 V. Similarly, numerous emission lines appear when a negative bias is applied to the device, and become increasingly bright as the bias decreases to -40 V. We note that no emission was observed from the device at any bias in the absence of the excitation laser - that is, all emissions discussed in this paper are field-activated PL rather than electroluminescence.

To investigate this effect further, we plot the intensity from a number of representative emitters as a function of applied bias in Figure 4.6b and Figure 4.6c. Figure 4.6b shows four emissions that are active within a positive bias range. The peak intensity at each chosen wavelength is extracted from the maximum intensity over 1.5 nm range. This window also helps account for spectral wandering and any stark shift. The PL intensity from each of these emitters is highly bias-dependent. For example, the intensity of the 581 nm line peaks at a bias of ≈10 V, while the 641 nm line peaks at ≈28 V. Interestingly, most of the emitters have a clear bias activation range - that is, they are optically active over this range and inactive at biases outside this range. Such behaviour has never been observed for any other solid-state quantum emitters, this is also discussed in detail below. The behaviour is substantially different when a negative bias is applied to the MLG electrode. As is shown in Figure 4.6a, as the bias is reduced from 0 V to -40 V, a number of emitters become optically active and none of them deactivate over the entire bias range. The intensity of a number of representative emissions from this group is plotted versus bias in Figure 4.6c. The emitters are very dim at zero bias, and the emission intensities increase linearly as the bias is reduced from 0 to -40 V under constant laser excitation power. We note that an increase in emitter intensity versus bias has been observed previously for neutrally charged NV centers in diamond[240,233]. However, more

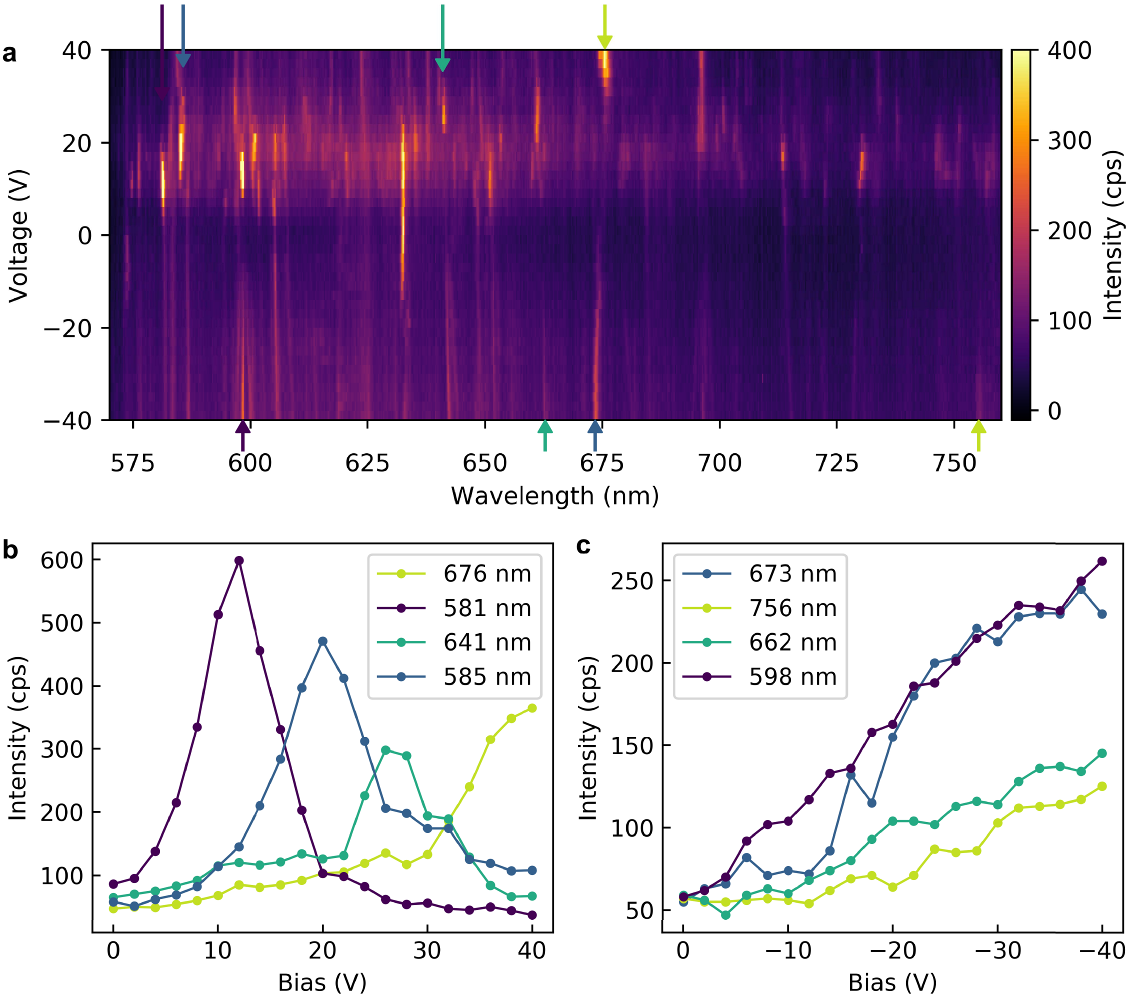

Figure 4.6: Activation of hBN emitters in the heterostructure device. a. PL spectra recorded as a function of bias, over the range of -40 to +40V. The lines at 580 nm and 620 nm are the G band and 2D band of MLG. The remaining lines are emitters in hBN. The upper and lower arrows indicate the position of the PL lines from which peaks are emission maxima are extracted for (b) and (c) respectively. b, c Emission intensity versus bias for a number of emitters activated by a positive (b) and a negative (c) voltage applied to the MLG electrode.

broadly, the observation of PL emissions that are inactive until a voltage is applied has not been reported for any solid-state quantum systems. Finally, based on the above results, most of the emitters appear to be track-able from the positive to the negative voltage range, indicating that they are the same emitters (i.e. each spectral line corresponds to the same emitter – or emitters belong to the same crystallographic origin).

4.2.3 DISCUSSION

We now turn to a discussion of the photo-physics of these emitters under applied bias. We attribute the emitter activation and deactivation caused by a positive bias (seen in Figure 4.6b) to changes in charge states of defects in hBN, and the activation of emitters under negative bias (seen in Figure 4.6c) to the injection of hot electrons from MLG into hBN. These two processes are characterised by the slow and fast emitter activation dynamics, as is discussed below in the context of the electron energy level diagram shown in Figure 4.7.

The device band diagram under zero bias is shown in Figure 4.7a. The MLG quasi Fermi level, E_F, and the bottom of the hBN conduction band are located 4.6 eV and 2.3 eV below the vacuum level, respectively[241,237]. Also shown on the diagram are two hypothetical charge transition levels of a defect in hBN, adapted from reported density functional theory (DFT) calculations[242,192]. Figures 4.7b and c show the device at a bias of +10 V and +20 V, respectively, and illustrate how a positive bias sweep causes sloping of the energy bands, and an effective sweep of E_F within a subset of the band gap of hBN. A defect with a charge transition level within this region of the band gap will gain/lose an electron as E_F moves above/below the level (Figure 4.7b). Similarly, a defect with two charge transition levels in this region of the band gap will change charge state twice if E_F sweeps through both levels. Hence, the hBN defect in Figure 4.7a will have lost two electrons upon the application of +20 V to the MLG (Figure 4.7c). Each change in the charge state of an emitter will result in a corresponding change in the defect energy levels and hence the emission spectrum[233,240]. Importantly, a change in charge state often causes activation or deactivation of an emitter – either absolutely or effectively by causing the emission energy to shift outside the measured spectral range[240]. Hence, activation of a hBN quantum emitter upon the application of a positive bias to the MLG electrode of our heterostructure device can be caused by a change in the charge state of the emitter by +1 (Figure 4.7b). Deactivation of the emitter at a greater positive bias can be caused by the second change in charge state, provided that E_F crosses a second charge transition level of the emitter (Figure 4.7c). Note that the defects are located at various depth of the hBN layer. Hence, upon voltage application, the band bending would individually influence different defects (and their corresponding charge transition levels) due to different distances from the graphene/p-doped silicon (discussed further below). A variation in the local environment of the defects can also account for the different voltages (and consequently the electric fields) required to control the emitters.

Based on the above, activation of an emitter upon application of a negative bias could be argued to be caused by a change in the charge state of the emitter by -1. However, an upward sweep of E_F within the band gap of hBN will populate deep defect levels; and thus we do not expect it to activate emitters. Moreover, we found that the activation rate measured by applying a step voltage function to the device is over three orders of magnitude slower for the case of positive bias than for the case of negative bias (Figure 4.5d and f, respectively), indicating a fundamental difference in the charge transfer dynamics. To explain this difference, we consider energy band diagrams for the negatively charged device shown in Figures 4.7d and e, for the case of -10 and -20 V respectively. Application of a bias that is negative with respect to the MGL electrode inverts the gradient of the sloped bands and effectively raises E_F towards the hBN conduction band. In this configuration, electrons excited in the MLG by the laser (yellow arrows in Figure 4.7) can tunnel across the barrier at the MLG-hBN interface and drift (red broken arrows) within hBN under the influence of the applied electric field. The resulting photocurrent provides a means to supply hot electrons to emitters via the hBN conduction band. This charge transfer mechanism is therefore expected to be fast relative to the case of a positive bias (Figure 4.7b and c), where electron removal from the deep hBN charge transition levels likely occurs via a hopping mechanism and electrons flow to the MLG via trap states inside the hBN band gap.

The above analysis illustrates two distinct charge transfer mechanisms between the MLG electrode and defects in hBN, which are slow/fast in the case of positive/negative bias, applied to the MLG. The first can account for emitter activation and deactivation upon application of a positive voltage sweep to the device, and the second can account for emitter activation by a negative bias. We note that the almost universal deactivation of emitters at +40 V, seen in Figure 4.6a, is likely a consequence of the fact that E_F lies very close to the hBN valence band and the ground states of most emitters are ionised at this voltage. We also note that, as is evident from Figure 4.7, the voltage needed to activate/deactivate various emitters is a function of the emitter location within the hBN. This observation combined with the fact that a number of distinct defect species are responsible for the rich emission spectrum of hBN accounts for the variation in activation and deactivation voltages seen in Figure 4.6a.

To provide further experimental support for our model, we increased the excitation laser wavelength from 532 nm ($\approx$2.3 eV) to 602 nm ($\approx$2 eV). The longer wavelength excitation should not be sufficient to overcome the energy barrier (see figure 4.7d-e) under negative bias, and hence no emitters should be activated. Indeed, this hypothesis is confirmed. Figure 4.7f shows PL spectra of emitters under positive and negative bias recorded at the same confocal spot using the two excitation wavelengths. It is clear that new emitters appear under negative bias when a 532 nm excitation laser is used, but no emission appears under the longer wavelength excitation of 602 nm.

To illustrate the potential of our devices for practical and scalable quantum photonic applications, we demonstrate the resonant excitation of these quantum emitters under a negative bias. We expect that under

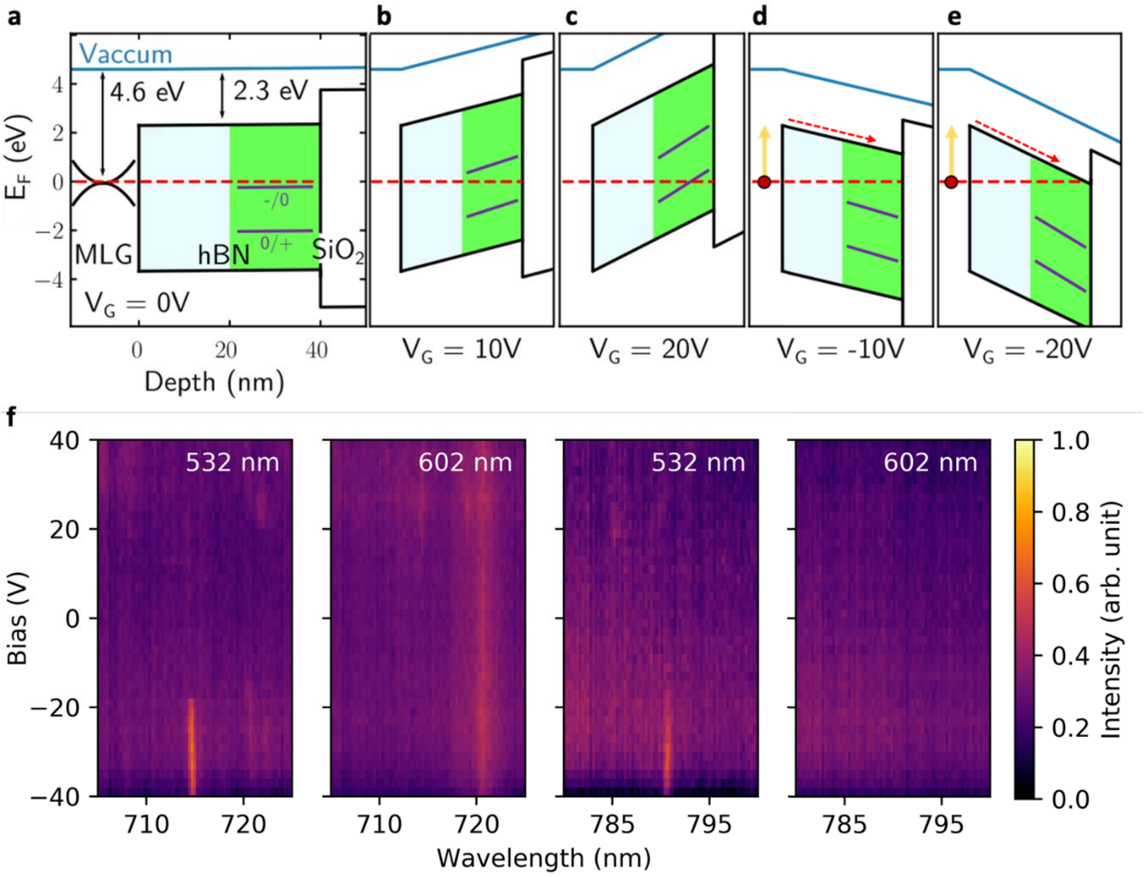

Figure 4.7: Band diagram of the heterostructure device under various bias configurations. a. The device where both electrodes are grounded (V_G = 0 V). The hBN capping layer is shown in light blue, and the hBN layer that contains quantum emitters is shown in green (the thickness of each hBN layer is assumed to be 20 nm). The MLG quasi-Fermi level (E_F) extends into the hBN, indicating charge transfer between MLG and defect states in hBN (see text). The purple lines indicate two hypothetical charge transition levels of a single defect in hBN. b,c. The device with a bias of +10 V (b) and +20 V (c) applied to the MLG electrode. d,e. The device with a bias of -10 V (d) and -20 V (e) applied to the MLG electrode. The solid yellow arrows show photoexcitation of an electron in MLG, and broken red arrows indicate the drift of the electrons via the band gaps of the hBN layers. f. Experimental verification of the model, whereby emitters (at ≈715 and 790 nm) are only visible under green excitation (λ_{exc} = 532 nm) but not under lower energy red excitation (λ_{exc} = 602 nm), at the same confocal spot. The emission at 720 nm is graphene Raman [229].

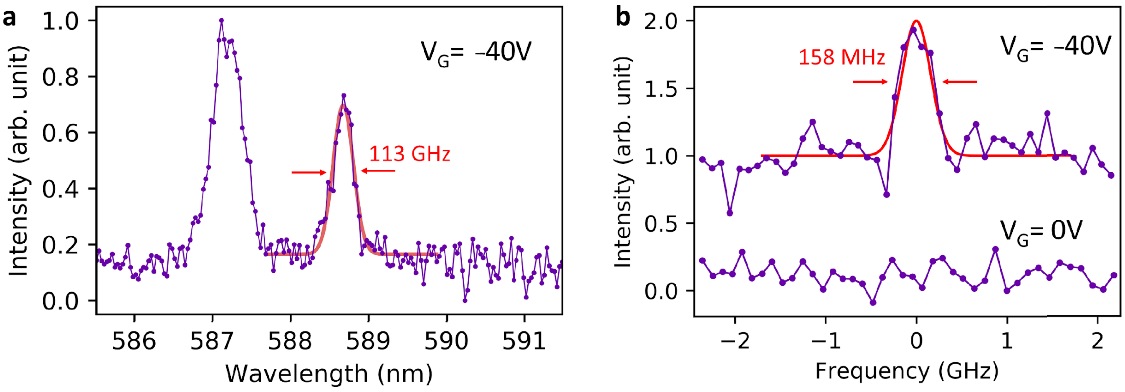

Figure 4.8: Coherent excitation of quantum emitters in hBN heterostructure. a. Emission spectrum of a single emitter with a ZPL at ≈588.5 nm, recorded under non-resonant 532 nm excitation. b. Resonant excitation of the same emitter, resulting in a nearly-coherent photon source with a linewidth of ≈158 MHz. Both measurements were done using a bias voltage, VG= −40 V.

these conditions, the charge transfer under bias governs the charge states of both emitters and surrounding charge traps and thus suppresses charge fluctuations and spectral diffusion of quantum emitters under resonant excitation[182]. This was indeed observed, as is illustrated in Figure 4.8. Figure 4.8a shows an emitter with a ZPL at ≈588.5 nm, recorded from the device using an off-resonant 532 nm excitation laser. The off-resonant linewidth is phonon broadened as expected. Figure 4.8b shows a resonant excitation scan of the same emitter with a measured linewidth of ≈158±19 MHz. Both measurements were taken using an applied bias, V_G=-40 V, and importantly, no resonant emission was observed at zero bias. For quantum emitters in hBN with excited state lifetimes on the order of ≈3 ns, ≈160 MHz certainly represents a nearly-coherent, Fourier Transform limited, linewidth, which is highly promising for future-generation indistinguishable photons.

4.3 Conclusion and Summary

To summarise, we demonstrate electrical modulation and control of a variety of quantum emitters in a vdW heterostructure. The quantum opto-electronic devices consist of hBN/MLG heterostructures; they operate at accessible voltages and can be assembled using readily-accessible fabrication techniques. We propose two distinct mechanisms for device operation versus bias polarity based on electrostatic charge switching of quantum emitters and the drift of hot photoelectrons. Our results open a plethora of new opportunities in integrated quantum photonics with vdW materials. First, the ability to modulate and switch on/off quantum emitters is imperative for scalable quantum circuitry. Second, electrostatic gating can now be used to activate emitters post hBN growth and processing, and to select emitters at specific wavelengths. Third, a single device can now be employed to activate and tune quantum emitters into resonance to achieve indistinguishable photons from quantum emitters in hBN. Indeed, our results already show that under negative bias a nearly-coherent quantum source in hBN with linewidths of $\approx$160 MHz can be obtained. Finally, and equally important, our results constitute the possibility to characterise charge transition levels of specific defects in hBN, and correlate them with theoretical studies of specific atomic defect structures.

5

Conclusion and Outlook

5.1 CONCLUSION

Controlling and manipulating individual quantum systems underpins the development of scalable quantum technologies. Hexagonal boron nitride is emerging as an exceptional platform for applications in quantum photonics and quantum emission from defects in this material is a promising candidate for quantum information carriers, flying qubits, integral to the future of advanced quantum technologies. The two-dimensional van der Waals (vdW) crystal hosts single-photon emitting defects (quantum emitters) opening new functionality currently inaccessibly with other 3D quantum sources. Due to the two-dimensional nature of the crystal, hBN is an ideal material to integrate into vdW heterostructure devices and has potential applications throughout many quantum technologies from advanced sensing to quantum communication and information processing.

In this thesis, I begin by demonstrating quantum random number generation using hBN single-photon emission as a source of random bits. This work was a proof of principle application of room temperature emission from the solid state van der Waals material hBN. At the time of the work, this was one of only a few real-life demonstrations of how we may immediately make use of hBN's bright quantum emission. We were able to show that by simply coupling the emission to a photonic circuit we could create a scalable technology capable of producing truly random numbers.

The exceptional room temperature properties of hBN SPEs are catalysis for research across the globe, but to unlock the full potential of these sources throughout quantum technologies much stronger understanding of their control, coherence, and broadening mechanisms is essential. In chapters 2-4 I explore the properties of hBNs single-photon emission at cryogenic temperatures to further our understanding of the utility of these quantum emitters. Most importantly I extensively study these emitters under resonant excitation, a technique limited to only a few studies, which enables us to attain precise information on the emitters and their environment. In chapter 2 I find that the photoluminescence (PL) for some hBN emitters is strongly dependent on local charge traps. I introduce a multiple laser excitation scheme and demonstrate considerable PL enhancement due to the suppression of long-lived dark states. To further detail the defects' interaction with their environment I proceed to study the emitter line broadening mechanisms explicitly. I find the line is broadened significantly by phonons even at 5 K, and the broadening follows a $\Delta\lambda \propto aT^1 + bT^3$ relationship with temperature, corresponding to first and second-order electron-phonon interactions. Finally, I demonstrate an electrical device capable of controlling the photoluminescence of emitters in hBN. In this work, we make use of the two-dimensional structure of the hBN lattice and fabricate a device for which the applied field is over a few tens of nanometers. Using this device, we are able to elucidate information on the potential position of hBN emitters within the hBN bandgap and comment on possible activation mechanisms due to band bending under an applied field.

The work of this thesis demonstrates how hBN single-photon emitters are immediately applicable in some quantum applications, and presents solutions that enable these sources to be used more universally throughout quantum information applications. Developing a complete understanding of these sources is not the work of only one student, let alone a single research group! But in this thesis, I advance our understanding of these sources by specifically focusing on the limitations of these emitters, and I show through study at cryogenic temperatures we can unveil information on how these two-level systems couple to their environments. In each chapter, I show how we can manipulate this environment to enhance and control the sources of flying qubits.

5.2 Outlook

In this section, I comment on some recent exciting work and potential directions of research for hBN single-photon emitters. Although hBN is an excellent candidate for the ideal single-photon source, there are many challenges that still remain before it can claim this title.

The first challenge is the deterministic creation of these emitters. At the present time, there is no fully deterministic mechanism to create hBN emitters. There are methods used to create specific classes of emitters; for instance, ion beam irradiation is the preferred technique to create the negatively charged boron vacancy, and for visible emitters, they are often ”created” using thermal annealing, or electron or plasma irradiation. But these techniques still often cause damage in the form of uncontrolled sputtering, surface states, vacancies, interstitials, and dislocations etc, which affects the quality of the emitters down the line when ideally we would want to consider a two-level system completely insulated from their environment. To this end, research into the formation of these defects, involving the precise classification of each specific emitter, is of utmost importance.

Interestingly, a new class of emitters at 437 nm (designated blue emitters) have recently been discovered. The blue emitters can be fabricated near deterministically (using an electron beam) from crystals with a characteristic emission at 4.1 eV.[243] These emitters have been found to have a near zero permanent dipole moment, which means they may be relatively insensitive to their local environments, which is integral for photon interference applications.[6,5] On the other hand, other defects in hBN exhibit spin-dependent fluorescence that can be initialised and coherently manipulated.

The next challenge will be demonstrating photon indistinguishability and multi-photon interference. Although Fourier-limited (lifetime-limited) lines from hBN are claimed to have been observed, there is still a question on the utility of such claims without the following interference experiments (see reference[137] and comments). Recently suppression of local charge fluctuations, using a similar device to that shown in chapter 4, has been shown to significantly reduce spectral diffusion of a visible emitter in hBN, enabling stable Fourier limited emission from hBN.[244] This stabilisation technique is extremely promising for multi-photon interference experiments as it enables both linewidth and wavelength tuning with a single device.

The final challenge to make full use of these sources will be to demonstrate an efficient way to extract coherent photons from the zero phonon line. There are a few avenues to pursue to achieve this goal. At present, coherent emission is only observed under resonant excitation. Using this excitation technique, one must find a way to distinguish between the excitation field and the emitted photons. Due to the two-dimensional nature of hBN it is highly feasible to consider a cross-polarisation scheme where the excitation field is filtered based on polarisation. This was briefly attempted without success during my thesis. The cross-polarisation technique could be coupled with the use of transparent substrates or suspended hBN flakes to further enhance the extinction of the excitation laser. Alternatively, hBN emitters could be coupled to a dielectric cavity to direct the emission in a separate spatial mode to the excitation. This approach may have the advantage of enhancing the emission via the Purcell effect whilst also maintaining the distinction between the excitation and emission fields. Another technique that can be used in combination or separately would be temporal filtering. Here short pulses are used to excite the two-level system and photons are only collected after the laser pulse has dissipated. The alternate avenue for extracting coherent emission would be spectral filtration under stokes (or possibly anti-stokes) excitation. Due to the much larger field amplitude required using off-resonant excitation, this would also require additional techniques to suppress spectral diffusion, and may also benefit from coupling to optical cavities to enhance the emission.

In summary, hexagonal boron nitride is an exciting and promising source of single photons with potential applications throughout advanced quantum technologies. Here, I investigate the cryogenic properties of hBN's quantum photoluminescence and demonstrate a proof of principle application for these emitters. Finally, I highlight some of the challenges and prospects for this material, specifically framed toward the broad interest in quantum optics with 2D materials.

A

Appendix

A.1 SECOND ORDER CORRELATION ANALYSIS

Second-order correlation measurements are routinely performed on many photoluminescence lines to reveal the nature of the emission. Using this measurement technique, we are able to determine how a source emits photons over time. As single-photon sources emit only one photon at a time, we describe their statistics as sub-Poissonian. A random distribution of photons over time is described as a Poissonian distribution, observed from sources such as lasers. If photons are distributed in bunches over time, they are described as super-Poissonian, as seen from thermal light sources. When taking the second-order correlation measurement, these distributions manifest themselves as a dip, flat line, or peak at zero delay time for sub-Poissonian, Poissonian, or super-Poissonian respectively.

We implement this experimentally using a fibre-based Hanbury Brown-Twiss intensity interferometer (HBT), and tunable bandpass filters to isolate a single photoluminescence peak. The data is normalized in real-time using the count rates on each detector as given by the equation below.

$$g^{(2)}(t) = C(t)/(N_1 N_2 \omega T) \tag{A.1}$$

Where C(t) is the un-normalized correlations, N_1 and N_2 are the detector count rates, ω is the bin width, and T is the total integration time.

If background correction is possible, i.e. the background counts are measurable, $g^{(2)}(t)$ data can be corrected by dividing by the signal-to-noise ratio.

$$g^{(2)}(t) = C(t)/(N_1 N_2 \omega T) \tag{A.2}$$

The autocorrelation data were fitted with a three-level model:

$$g^{(2)}(t) = 1 - ((1 - A) + A_m)e^{-t/\tau} + A_m e^{-t/\tau_m} \tag{A.3}$$

Where A is equal to the antibunching minimum ($g^{(2)}(0)$), A_m is the bunching amplitude associated with the metastable state, and τ and τ_m are the lifetimes for the excited state and the metastable states respectively.

A.2 SPECTROMETER RESOLUTION

Spectroscopy is a major analysis technique used extensively throughout this thesis. Accordingly, one must fully characterise the analysis instruments to understand their limitations. An Andor Shamrock 303i spectrometer is used in the majority of spectrum measurements. Figure. A.1a displays the resolution limit from this spectrometer using an 1800 lines mm^{-1} grating and a graded-index multi-mode fibre acting as a slit of 62.5 µm. A photoluminescence line of ∼2 GHz (1.3 pm), characterised using resonant photoluminescence excitation[6], is observed to have a width of ∼132 GHz (84 pm). With the 300 lines mm^{-1} grating we observe a spectrometer limited linewidth of ∼631 GHz (400 pm) (Figure. A.1(b)).

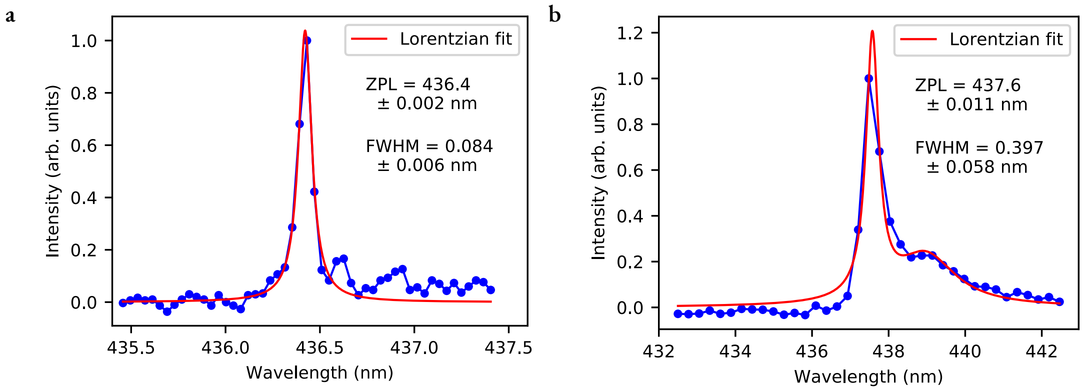

Figure A.1: Andor spectrometer resolution. (a) Using the 1800 lines mm^{-1} grating and a slit size of 62.5 μm a PL line of ~2 GHz (1.3 pm) is observed to have a width of ~132 GHz (84 pm). (b) Using the 300 lines mm^{-1} grating the same PL peak is observed to have a linewidth of ~631 GHz (400 pm).

References

[1] Simon JU White, Tieshan Yang, Nikolai Dontschuk, Chi Li, Zai-Quan Xu, Mehran Kianinia, Alastair Stacey, Milos Toth, and Igor Aharonovich. Electrical control of quantum emitters in a van der waals heterostructure. *Light: Science & Applications*, 11(1):1–9, 2022.

[2] Simon White, Connor Stewart, Alexander S Solntsev, Chi Li, Milos Toth, Mehran Kianinia, and Igor Aharonovich. Phonon dephasing and spectral diffusion of quantum emitters in hexagonal boron nitride. *Optica*, 8(9):1153–1158, 2021.

[3] Simon JU White, Ngoc My Hanh Duong, Alexander S Solntsev, Je-Hyung Kim, Mehran Kianinia, and Igor Aharonovich. Optical repumping of resonantly excited quantum emitters in hexagonal boron nitride. *Physical Review Applied*, 14(4):044017, 2020.

[4] Simon JU White, Friederike Klauck, Toan Trong Tran, Nora Schmitt, Mehran Kianinia, Andrea Steinfurth, Matthias Heinrich, Milos Toth, Alexander Szameit, Igor Aharonovich, et al. Quantum random number generation using a hexagonal boron nitride single photon emitter. *Journal of Optics*, 23(1):01LT01, 2020.

[5] Ivan Zhigulin, Jake Horder, Victor Ivady, Simon JU White, Angus Gale, Chi Li, Charlene J Lobo, Milos Toth, Igor Aharonovich, and Mehran Kianinia. Stark effect of quantum blue emitters in hbn. *arXiv preprint arXiv:2208.00600*, 2022.

[6] Jake Horder, Simon J.U. White, Angus Gale, Chi Li, Kenji Watanabe, Takashi Taniguchi, Mehran Kianinia, Igor Aharonovich, and Milos Toth. Coherence properties of electron-beam-activated emitters in hexagonal boron nitride under resonant excitation. *Phys. Rev. Appl.*, 18:064021, Dec 2022.

[7] Thinh N Tran, Sejeong Kim, Simon JU White, Minh Anh Phan Nguyen, Licheng Xiao, Stefan Strauf, Tieshan Yang, Igor Aharonovich, and Zai-Quan Xu. Enhanced emission from interlayer excitons coupled to plasmonic gap cavities. *Small*, 17(45):2103994, 2021.

[8] Yongliang Chen, Mika T Westerhausen, Chi Li, Simon White, Carlo Bradac, Avi Bendavid, Milos Toth, Igor Aharonovich, and Toan Trong Tran. Solvent-exfoliated hexagonal boron nitride nanoflakes for quantum emitters. *ACS Applied Nano Materials*, 4(10):10449–10457, 2021.

[9] Yongliang Chen, Chi Li, Simon White, Milad Nonahal, Zai-Quan Xu, Kenji Watanabe, Takashi Taniguchi, Milos Toth, Toan Trong Tran, and Igor Aharonovich. Generation of high-density quantum emitters in high-quality, exfoliated hexagonal boron nitride. *ACS Applied Materials & Interfaces*, 13(39):47283–47292, 2021.

[10] Milad Nonahal, Simon JU White, Blake Regan, Chi Li, Aleksandra Trycz, Sejeong Kim, Igor Aharonovich, and Mehran Kianinia. Bottom-up synthesis of single crystal diamond pyramids containing germanium vacancy centers. *Advanced Quantum Technologies*, 4(7):2100037, 2021.

[11] Nicholas Joel Damaso, Simon JU White, and Sejeong Kim. Analysis of anapole resonators in low index materials. *Journal of Optics*, 23(3):034003, 2021.

[12] Nils Bernhardt, Sejeong Kim, Johannes E Fröch, Simon JU White, Ngoc My Hanh Duong, Zhe He, Bo Chen, Jin Liu, Igor Aharonovich, and Alexander S Solntsev. Large few-layer hexagonal boron nitride flakes for nonlinear optics. *Optics Letters*, 46(3):564–567, 2021.

[13] Mehran Kianinia, Simon White, Johannes E Fro ch, Carlo Bradac, and Igor Aharonovich. Generation of spin defects in hexagonal boron nitride. *ACS Photonics*, 7(8):2147–2152, 2020.

[14] Nils Bernhardt, Kirill Koshelev, Simon JU White, Kelvin Wong Choon Meng, Johannes E Froch, Sejeong Kim, Toan Trong Tran, Duk-Yong Choi, Yuri Kivshar, and Alexander S Solntsev. Quasi-bic resonant enhancement of second-harmonic generation in ws2 monolayers. *Nano Letters*, 20(7):5309–5314, 2020.

[15] Max Planck. Zur theorie des gesetzes der energieverteilung im normalspektrum. *Berlin*, pages 237–245, 1900.

[16] Albert Einstein. Über einen die erzeugung und verwandlung des lichtes betreffenden heuristischen gesichtspunkt. *Annalen der Physik*, 1905.

[17] Arnold B Arons and MB Peppard. Einstein's proposal of the photon concept—a translation of the annalen der physik paper of 1905. *American Journal of Physics*, 33(5):367–374, 1965.

[18] Arthur H Compton. A quantum theory of the scattering of x-rays by light elements. *Physical review*, 21(5):483, 1923.

[19] Gilbert N Lewis. The conservation of photons. *Nature*, 118(2981):874–875, 1926.

[20] Louis De Broglie. *Recherches sur la théorie des quanta*. PhD thesis, Migration-université en cours d'affectation, 1924.

[21] Erwin Schrödinger. An undulatory theory of the mechanics of atoms and molecules. *Physical review*, 28(6):1049, 1926.

[22] Werner Heisenberg. Über den anschaulichen inhalt der quantentheoretischen kinematik und mechanik. In *Original Scientific Papers Wissenschaftliche Originalarbeiten*, pages 478–504. Springer, 1985.

[23] Paul Adrien Maurice Dirac. The quantum theory of the emission and absorption of radiation. *Proceedings of the Royal Society of London. Series A, Containing Papers of a Mathematical and Physical Character*, 114(767):243–265, 1927.

[24] Enrico Fermi. Quantum theory of radiation. *Reviews of modern physics*, 4(1):87, 1932.

[25] John Preskill. Quantum computing 40 years later. *arXiv preprint arXiv:2106.10522*, 2021.

[26] R Feynman. Internat. *J. Theor. Phys*, 21:467–488, 1982.

[27] Albert Einstein, Boris Podolsky, and Nathan Rosen. Can quantum-mechanical description of physical reality be considered complete? *Physical review*, 47(10):777, 1935.

[28] Erwin Schrödinger. Die gegenwärtige situation in der quantenmechanik. *Naturwissenschaften*, 23(50):844–849, 1935.

[29] David Bohm. *Quantum theory*. Prentice-Hall, New York, 1951.

[30] John S Bell. On the einstein podolsky rosen paradox. *Physics Physique Fizika*, 1(3):195, 1964.

[31] Charles H Bennett, Herbert J Bernstein, Sandu Popescu, and Benjamin Schumacher. Concentrating partial entanglement by local operations. *Physical Review A*, 53(4):2046, 1996.

[32] Nicolas Gisin, Grégoire Ribordy, Wolfgang Tittel, and Hugo Zbinden. Quantum cryptography. *Reviews of modern physics*, 74(1):145, 2002.

[33] CH Bennett and G Brassard. Int. conf. computers, systems & signal processing, bangalore, 1984.

[34] Artur K Ekert. Quantum cryptography and bell's theorem. In *Quantum Measurements in Optics*, pages 413–418. Springer, 1992.

[35] TE Northup and R Blatt. Quantum information transfer using photons. *Nature photonics*, 8(5):356–363, 2014.

[36] Juan Ignacio Cirac, Peter Zoller, H Jeff Kimble, and Hideo Mabuchi. Quantum state transfer and entanglement distribution among distant nodes in a quantum network. *Physical Review Letters*, 78(16):3221, 1997.

[37] Jianwei Wang, Fabio Sciarrino, Anthony Laing, and Mark G Thompson. Integrated photonic quantum technologies. *Nature Photonics*, 14(5):273–284, 2020.

[38] Jeremy L O'brien, Akira Furusawa, and Jelena Vučković. Photonic quantum technologies. *Nature Photonics*, 3(12):687–695, 2009.

[39] M. D. Eisaman, J. Fan, A. Migdall, and S. V. Polyakov. Invited Review Article: Single-photon sources and detectors. *Review of Scientific Instruments*, 82(7):071101, jul 2011.

[40] Vittorio Giovannetti, Seth Lloyd, and Lorenzo Maccone. Advances in quantum metrology. *Nature photonics*, 5(4):222–229, 2011.

[41] Emanuele Polino, Mauro Valeri, Nicolò Spagnolo, and Fabio Sciarrino. Photonic quantum metrology. *AVS Quantum Science*, 2(2):024703, 2020.

[42] Vittorio Giovannetti, Seth Lloyd, and Lorenzo Maccone. Quantum-enhanced measurements: beating the standard quantum limit. *Science*, 306(5700):1330–1336, 2004.

[43] MJ Holland and K Burnett. Interferometric detection of optical phase shifts at the heisenberg limit. *Physical review letters*, 71(9):1355, 1993.

[44] Carlton M Caves. Quantum-mechanical noise in an interferometer. *Physical Review D*, 23(8):1693, 1981.

[45] Junaid Aasi, Joan Abadie, BP Abbott, Richard Abbott, TD Abbott, MR Abernathy, Carl Adams, Thomas Adams, Paolo Addesso, RX Adhikari, et al. Enhanced sensitivity of the ligo gravitational wave detector by using squeezed states of light. *Nature Photonics*, 7(8):613–619, 2013.

[46] Daniel F Walls. Squeezed states of light. *nature*, 306(5939):141–146, 1983.

[47] Jonathan P Dowling. Quantum optical metrology–the lowdown on high-noon states. *Contemporary physics*, 49(2):125–143, 2008.

[48] Lu Zhang and Kam Wai Clifford Chan. Scalable generation of multi-mode noon states for quantum multiple-phase estimation. *Scientific reports*, 8(1):1–12, 2018.

[49] Christian L Degen, Friedemann Reinhard, and Paola Cappellaro. Quantum sensing. *Reviews of modern physics*, 89(3):035002, 2017.

[50] Romana Schirhagl, Kevin Chang, Michael Loretz, and Christian L Degen. Nitrogen-vacancy centers in diamond: nanoscale sensors for physics and biology. *Annu. Rev. Phys. Chem*, 65(1):83–105, 2014.

[51] HJ Mamin, M Kim, MH Sherwood, CT Rettner, K Ohno, DD Awschalom, and D Rugar. Nanoscale nuclear magnetic resonance with a nitrogen-vacancy spin sensor. *Science*, 339(6119):557–560, 2013.

[52] Andreas Gottscholl, Matthias Diez, Victor Soltamov, Christian Kasper, Andreas Sperlich, Mehran Kianinia, Carlo Bradac, Igor Aharonovich, and Vladimir Dyakonov. Room temperature coherent control of spin defects in hexagonal boron nitride. *Science Advances*, 7(14):eabf3630, 2021.

[53] Andreas Gottscholl, Matthias Diez, Victor Soltamov, Christian Kasper, Dominik Krauße, Andreas Sperlich, Mehran Kianinia, Carlo Bradac, Igor Aharonovich, and Vladimir Dyakonov. Spin defects in hbn as promising temperature, pressure and magnetic field quantum sensors. *Nature communications*, 12(1):1–8, 2021.

[54] David P DiVincenzo. The physical implementation of quantum computation. *Fortschritte der Physik: Progress of Physics*, 48(9-11):771–783, 2000.

[55] Andrew Steane. Quantum computing. *Reports on Progress in Physics*, 61(2):117, 1998.

[56] Yuri Ozhigov. Quantum computer can not speed up iterated applications of a black box. In *Quantum Computing and Quantum Communications*, pages 152–159. Springer, 1999.

[57] Lov K Grover. Quantum mechanics helps in searching for a needle in a haystack. *Physical review letters*, 79(2):325, 1997.

[58] Yudong Cao, Jonathan Romero, Jonathan P Olson, Matthias Degroote, Peter D Johnson, Mária Kieferová, Ian D Kivlichan, Tim Menke, Borja Peropadre, Nicolas PD Sawaya, et al. Quantum chemistry in the age of quantum computing. *Chemical reviews*, 119(19):10856–10915, 2019.

[59] Peter W Shor. Polynomial-time algorithms for prime factorization and discrete logarithms on a quantum computer. *SIAM review*, 41(2):303–332, 1999.

[60] Peter W Shor. Algorithms for quantum computation: Discrete logarithms and factoring. In *Foundations of Computer Science, 1994 Proceedings., 35th Annual Symposium on*, pages 124–134. Ieee, 1994.

[61] Lieven MK Vandersypen, Matthias Steffen, Gregory Breyta, Costantino S Yannoni, Mark H Sherwood, and Isaac L Chuang. Experimental realization of shor's quantum factoring algorithm using nuclear magnetic resonance. *Nature*, 414(6866):883, 2001.

[62] Ben P Lanyon, Till J Weinhold, Nathan K Langford, Marco Barbieri, Daniel FV James, Alexei Gilchrist, and Andrew G White. Experimental demonstration of a compiled version of shor's algorithm with quantum entanglement. *Physical Review Letters*, 99(25):250505, 2007.

[63] Alberto Politi, Jonathan CF Matthews, and Jeremy L O'brien. Shor's quantum factoring algorithm on a photonic chip. *Science*, 325(5945):1221–1221, 2009.

[64] Alexandre Blais, Ren-Shou Huang, Andreas Wallraff, Steven M Girvin, and R Jun Schoelkopf. Cavity quantum electrodynamics for superconducting electrical circuits: An architecture for quantum computation. *Physical Review A*, 69(6):062320, 2004.

[65] Devon Biggerstaff. *On integrated photonic quantum simulations*. PhD thesis, The University of Queensland, 2015.

[66] Anthony Mark Fox, Mark Fox, et al. *Quantum optics: an introduction*, volume 15. Oxford university press, 2006.

[67] I Aharonovich, Stefania Castelletto, DA Simpson, Chun-Hsu Su, AD Greentree, and Steven Prawer. Diamond-based single-photon emitters. *Reports on progress in Physics*, 74(7):076501, 2011.

[68] Sonia Buckley, Kelley Rivoire, and Jelena Vučković. Engineered quantum dot single-photon sources. *Reports on Progress in Physics*, 75(12):126503, 2012.

[69] Fengnian Xia, Han Wang, Di Xiao, Madan Dubey, and Ashwin Ramasubramaniam. Two-dimensional material nanophotonics. *Nature Photonics*, 8(12):899–907, 2014.

[70] Chunyi Zhi, Yoshio Bando, Chengchun Tang, Hiroaki Kuwahara, and Dimitri Golberg. Large-scale fabrication of boron nitride nanosheets and their utilization in polymeric composites with improved thermal and mechanical properties. *Advanced Materials*, 21(28):2889–2893, 2009.

[71] Yi Lin, Tiffany V Williams, and John W Connell. Soluble, exfoliated hexagonal boron nitride nanosheets. *The Journal of Physical Chemistry Letters*, 1(1):277–283, 2010.

[72] Xuekun Lu, Minfeng Yu, Hui Huang, and Rodney S Ruoff. Tailoring graphite with the goal of achieving single sheets. *Nanotechnology*, 10(3):269, 1999.

[73] Cory R Dean, Andrea F Young, Inanc Meric, Chris Lee, Lei Wang, Sebastian Sorgenfrei, Kenji Watanabe, Takashi Taniguchi, Phillip Kim, Kenneth L Shepard, et al. Boron nitride substrates for high-quality graphene electronics. *Nature nanotechnology*, 5(10):722–726, 2010.

[74] Liam Britnell, Roman V Gorbachev, Rashid Jalil, Branson D Belle, Fred Schedin, Mikhail I Katsnelson, Laurence Eaves, Sergey V Morozov, Alexander S Mayorov, Nuno MR Peres, et al. Electron tunneling through ultrathin boron nitride crystalline barriers. *Nano letters*, 12(3):1707–1710, 2012.

[75] Genevieve Clark, John R Schaibley, Jason Ross, Takashi Taniguchi, Kenji Watanabe, Joshua R Hendrickson, Shin Mou, Wang Yao, and Xiaodong Xu. Single defect light-emitting diode in a van der waals heterostructure. *Nano letters*, 16(6):3944–3948, 2016.

[76] Carmen Palacios-Berraquero. Atomically-thin quantum light emitting diodes. In *Quantum confined excitons in 2-dimensional materials*, pages 71–89. Springer, 2018.

[77] Matthew Yankowitz, Qiong Ma, Pablo Jarillo-Herrero, and Brian J LeRoy. van der waals heterostructures combining graphene and hexagonal boron nitride. *Nature Reviews Physics*, 1(2):112–125, 2019.

[78] Kenji Watanabe, Takashi Taniguchi, and Hisao Kanda. Direct-bandgap properties and evidence for ultraviolet lasing of hexagonal boron nitride single crystal. *Nature materials*, 3(6):404–409, 2004.

[79] Kenji Watanabe, Takashi Taniguchi, Takahiro Niiyama, Kenta Miya, and Masateru Taniguchi. Far-ultraviolet plane-emission handheld device based on hexagonal boron nitride. *Nature photonics*, 3(10):591–594, 2009.

[80] Guillaume Cassabois, Pierre Valvin, and Bernard Gil. Hexagonal boron nitride is an indirect bandgap semiconductor. *Nature photonics*, 10(4):262–266, 2016.

[81] K Cho. Excitons (topics in current physics), 1979.

[82] J Serrano, A Bosak, Raúl Arenal, M Krisch, Kenji Watanabe, T Taniguchi, H Kanda, Angel Rubio, and Ludger Wirtz. Vibrational properties of hexagonal boron nitride: inelastic x-ray scattering and ab initio calculations. *Physical review letters*, 98(9):095503, 2007.

[83] Toan Trong Tran, Kerem Bray, Michael J Ford, Milos Toth, and Igor Aharonovich. Quantum emission from hexagonal boron nitride monolayers. *Nature nanotechnology*, 11(1):37–41, 2016.

[84] Audrius Alkauskas, Bob B Buckley, David D Awschalom, and Chris G Van de Walle. First-principles theory of the luminescence lineshape for the triplet transition in diamond nv centres. *New Journal of Physics*, 16(7):073026, 2014.

[85] Sherif Abdulkader Tawfik, Sajid Ali, Marco Fronzi, Mehran Kianinia, Toan Trong Tran, Catherine Stampfl, Igor Aharonovich, Milos Toth, and Michael J Ford. First-principles investigation of quantum emission from hbn defects. *Nanoscale*, 9(36):13575–13582, 2017.

[86] Toan Trong Tran, Christopher Elbadawi, Daniel Totonjian, Charlene J Lobo, Gabriele Grosso, Hyowon Moon, Dirk R Englund, Michael J Ford, Igor Aharonovich, and Milos Toth. Robust multicolor single photon emission from point defects in hexagonal boron nitride. *ACS nano*, 10(8):7331–7338, 2016.

[87] Gabriele Grosso, Hyowon Moon, Benjamin Lienhard, Sajid Ali, Dmitri K Efetov, Marco M Furchi, Pablo Jarillo-Herrero, Michael J Ford, Igor Aharonovich, and Dirk Englund. Tunable and high-purity room temperature single-photon emission from atomic defects in hexagonal boron nitride. *Nature communications*, 8(1):1–8, 2017.

[88] Mehran Kianinia, Sherif Abdulkader Tawfik, Blake Regan, Toan Trong Tran, Michael J Ford, Igor Aharonovich, and Milos Toth. Robust solid state quantum system operating at 800 k. In *CLEO: QELS_Fundamental Science*, pages JTu5A–24. Optica Publishing Group, 2017.

[89] Nathan Chejanovsky, Mohammad Rezai, Federico Paolucci, Youngwook Kim, Torsten Rendler, Wafa Rouabeh, Felipe Fávaro de Oliveira, Patrick Herlinger, Andrej Denisenko, Sen Yang, et al. Structural attributes and photodynamics of visible spectrum quantum emitters in hexagonal boron nitride. *Nano letters*, 16(11):7037–7045, 2016.

[90] Nicholas R Jungwirth, Brian Calderon, Yanxin Ji, Michael G Spencer, Michael E Flatté, and Gregory D Fuchs. Temperature dependence of wavelength selectable zero-phonon emission from single defects in hexagonal boron nitride. *Nano letters*, 16(10):6052–6057, 2016.

[91] Niko Nikolay, Noah Mendelson, Nikola Sadzak, Florian Böhm, Toan Trong Tran, Bernd Sontheimer, Igor Aharonovich, and Oliver Benson. Very large and reversible stark-shift tuning of single emitters in layered hexagonal boron nitride. *Physical Review Applied*, 11(4):041001, 2019.

[92] Noah Mendelson, Zai-Quan Xu, Toan Trong Tran, Mehran Kianinia, John Scott, Carlo Bradac, Igor Aharonovich, and Milos Toth. Engineering and tuning of quantum emitters in few-layer hexagonal boron nitride. *ACS nano*, 13(3):3132–3140, 2019.

[93] Noah Mendelson, Marcus Doherty, Milos Toth, Igor Aharonovich, and Toan Trong Tran. Strain-induced modification of the optical characteristics of quantum emitters in hexagonal boron nitride. *Advanced Materials*, 32(21):1908316, 2020.

[94] Daniil M Lukin, Alexander D White, Rahul Trivedi, Melissa A Guidry, Naoya Morioka, Charles Babin, Öney O Soykal, Jawad Ul-Hassan, Nguyen Tien Son, Takeshi Ohshima, et al. Spectrally reconfigurable quantum emitters enabled by optimized fast modulation. *npj Quantum Information*, 6(1):1–9, 2020.

[95] Chi Li, Zai-Quan Xu, Noah Mendelson, Mehran Kianinia, Milos Toth, and Igor Aharonovich. Purification of single-photon emission from hbn using post-processing treatments. *Nanophotonics*, 8(11):2049–2055, 2019.

[96] Tobias Vogl, Ruvi Lecamwasam, Ben C. Buchler, Yuerui Lu, and Ping Koy Lam. Compact Cavity-Enhanced Single-Photon Generation with Hexagonal Boron Nitride. *ACS Photonics*, 6(8):1955–1962, 8 2019.

[97] Ali W Elshaari, Anas Skalli, Samuel Gyger, Martin Nurizzo, Lucas Schweickert, Iman Esmaeil Zadeh, Mikael Svedendahl, Stephan Steinhauer, and Val Zwiller. Deterministic integration of hbn emitter in silicon nitride photonic waveguide. *Advanced Quantum Technologies*, 4(6):2100032, 2021.

[98] Stefan Häußler, Gregor Bayer, Richard Waltrich, Noah Mendelson, Chi Li, David Hunger, Igor Aharonovich, and Alexander Kubanek. Tunable fiber-cavity enhanced photon emission from defect centers in hbn. *Advanced Optical Materials*, 9(17):2002218, 2021.

[99] Johannes E Fröch, Sejeong Kim, Noah Mendelson, Mehran Kianinia, Milos Toth, and Igor Aharonovich. Coupling hexagonal boron nitride quantum emitters to photonic crystal cavities. *ACS nano*, 14(6):7085–7091, 2020.

[100] Tobias Vogl, Kabilan Sripathy, Ankur Sharma, Prithvi Reddy, James Sullivan, Joshua R Machacek, Linglong Zhang, Fouad Karouta, Ben C Buchler, Marcus W Doherty, et al. Radiation tolerance of two-dimensional material-based devices for space applications. *Nature communications*, 10(1):1–10, 2019.

[101] Chong-Ki Hong, Zhe-Yu Ou, and Leonard Mandel. Measurement of subpicosecond time intervals between two photons by interference. *Physical review letters*, 59(18):2044, 1987.

[102] H Fearn and R Loudon. Quantum theory of the lossless beam splitter. *Optics communications*, 64(6):485–490, 1987.

[103] Charles Santori, David Fattal, Jelena Vučković, Glenn S Solomon, and Yoshihisa Yamamoto. Indistinguishable photons from a single-photon device. *Nature*, 419(6907):594, 2002.

[104] L Besombes, K Kheng, L Marsal, and H Mariette. Acoustic phonon broadening mechanism in single quantum dot emission. *Physical Review B*, 63(15):155307, 2001.

[105] F Gindele, K Hild, Wolfgang Langbein, and U Woggon. Phonon interaction of single excitons and biexcitons. *Physical Review B*, 60(4):R2157, 1999.

[106] Xudong Fan, T Takagahara, JE Cunningham, and Hailin Wang. Pure dephasing induced by exciton–phonon interactions in narrow gaas quantum wells. *Solid state communications*, 108(11):857–861, 1998.

[107] JL Skinner and D Hsu. Pure dephasing of a two-level system. *The Journal of Physical Chemistry*, 90(21):4931–4938, 1986.

[108] Kumarasiri Konthasinghe, Chitraleema Chakraborty, Nikhil Mathur, Liangyu Qiu, Arunabh Mukherjee, Gregory D Fuchs, and A. Nick Vamivakas. Rabi oscillations and resonance fluorescence from a single hexagonal boron nitride quantum emitter. *Optica*, 6(5):542, 5 2019.

[109] WB Gao, Atac Imamoglu, Hannes Bernien, and Ronald Hanson. Coherent manipulation, measurement and entanglement of individual solid-state spins using optical fields. *Nature Photonics*, 9(6):363–373, 2015.

[110] Yu Zhou, Abdullah Rasmita, Ke Li, Qihua Xiong, Igor Aharonovich, and Wei-bo Gao. Coherent control of a strongly driven silicon vacancy optical transition in diamond. *Nature communications*, 8(1):1–7, 2017.

[111] D Andrew Golter, Thein Oo, Mayra Amezcua, Kevin A Stewart, and Hailin Wang. Optomechanical quantum control of a nitrogen-vacancy center in diamond. *Physical review letters*, 116(14):143602, 2016.

[112] A Batalov, C Zierl, T Gaebel, P Neumann, I-Y Chan, G Balasubramanian, PR Hemmer, F Jelezko, and J Wrachtrup. Temporal coherence of photons emitted by single nitrogen-vacancy defect centers in diamond using optical rabi-oscillations. *Physical review letters*, 100(7):077401, 2008.

[113] Jonas Nils Becker, Johannes Görlitz, Carsten Arend, Matthew Markham, and Christoph Becher. Ultrafast all-optical coherent control of single silicon vacancy colour centres in diamond. *Nature communications*, 7(1):1–6, 2016.

[114] Antonio Acín, Serge Massar, and Stefano Pironio. Randomness versus nonlocality and entanglement. *Physical review letters*, 108(10):100402, 2012.

[115] Donald E Knuth. *Art of computer programming, volume 2: Seminumerical algorithms*. Addison-Wesley Professional, 2014.

[116] Miguel Herrero-Collantes and Juan Carlos Garcia-Escartin. Quantum random number generators. *Reviews of Modern Physics*, 89(1):015004, 2017.

[117] Xiongfeng Ma, Xiao Yuan, Zhu Cao, Bing Qi, and Zhen Zhang. Quantum random number generation. *npj Quantum Information*, 2(1):1–9, 2016.

[118] Helmut Schmidt. Quantum-mechanical random-number generator. *Journal of Applied Physics*, 41(2):462–468, 1970.

[119] Christian Gabriel, Christoffer Wittmann, Denis Sych, Ruifang Dong, Wolfgang Mauerer, Ulrik L Andersen, Christoph Marquardt, and Gerd Leuchs. A generator for unique quantum random numbers based on vacuum states. *Nature Photonics*, 4(10):711–715, 2010.

[120] Thomas Roger, Taofiq Paraiso, Innocenzo De Marco, Davide G Marangon, Zhiliang Yuan, and Andrew J Shields. Real-time interferometric quantum random number generation on chip. *JOSA B*, 36(3):B137–B142, 2019.

[121] Bing Qi, Yue-Meng Chi, Hoi-Kwong Lo, and Li Qian. High-speed quantum random number generation by measuring phase noise of a single-mode laser. *Optics letters*, 35(3):312–314, 2010.

[122] Markus Gräfe, René Heilmann, Armando Perez-Leija, Robert Keil, Felix Dreisow, Matthias Heinrich, Hector Moya-Cessa, Stefan Nolte, Demetrios N Christodoulides, and Alexander Szameit. On-chip generation of high-order single-photon w-states. *Nature Photonics*, 8(10):791–795, 2014.

[123] Xing Chen, Johannes N Greiner, Jörg Wrachtrup, and Ilja Gerhardt. Single photon randomness based on a defect center in diamond. *Scientific reports*, 9(1):1–10, 2019.

[124] Qing Luo, Zedi Cheng, Junkai Fan, Lijuan Tan, Haizhi Song, Guangwei Deng, You Wang, and Qiang Zhou. Quantum random number generator based on single-photon emitter in gallium nitride. *Optics Letters*, 45(15):4224–4227, 2020.

[125] Yang Liu, Qi Zhao, Ming-Han Li, Jian-Yu Guan, Yanbao Zhang, Bing Bai, Weijun Zhang, Wen-Zhao Liu, Cheng Wu, Xiao Yuan, et al. Device-independent quantum random-number generation. *Nature*, 562(7728):548–551, 2018.

[126] Lukas Oberreiter and Ilja Gerhardt. Light on a beam splitter: More randomness with single photons. *Laser & Photonics Reviews*, 10(1):108–115, 2016.

[127] Pascale Senellart, Glenn Solomon, and Andrew White. High-performance semiconductor quantum-dot single-photon sources. *Nature nanotechnology*, 12(11):1026–1039, 2017.

[128] Brahim Lounis and William E Moerner. Single photons on demand from a single molecule at room temperature. *Nature*, 407(6803):491–493, 2000.

[129] Igor Aharonovich, Dirk Englund, and Milos Toth. Solid-state single-photon emitters. *Nature Photonics*, 10(10):631–641, 2016.

[130] Songyan Hou, Muhammad Danang Birowosuto, Saleem Umar, Maurice Ange Anicet, Roland Yingjie Tay, Philippe Coquet, Beng Kang Tay, Hong Wang, and Edwin Hang Tong Teo. Localized emission from laser-irradiated defects in 2d hexagonal boron nitride. *2D Materials*, 5(1):015010, 2017.

[131] Mehran Kianinia, Simon White, Johannes E. Fröch, Carlo Bradac, and Igor Aharonovich. Generation of spin defects in hexagonal boron nitride. *ACS Photonics*, 7(8):2147–2152, 2020.

[132] Zai-Quan Xu, Christopher Elbadawi, Toan Trong Tran, Mehran Kianinia, Xiuling Li, Daobin Liu, Timothy B Hoffman, Minh Nguyen, Sejeong Kim, James H Edgar, et al. Single photon emission from plasma treated 2d hexagonal boron nitride. *Nanoscale*, 10(17):7957–7965, 2018.

[133] Noah Mendelson, Dipankar Chugh, Jeffrey R. Reimers, Tin S. Cheng, Andreas Gottscholl, Hu Long, Christopher J. Mellor, Alex Zettl, Vladimir Dyakonov, Peter H. Beton, Sergei V. Novikov, Chennupati Jagadish, Hark Hoe Tan, Michael J. Ford, Milos Toth, Carlo Bradac, and Igor Aharonovich. Identifying carbon as the source of visible single-photon emission from hexagonal boron nitride. *Nature Materials*, 20(3):321–328, 3 2021.

[134] Jeffrey R Reimers, Jun Shen, Mehran Kianinia, Carlo Bradac, Igor Aharonovich, Michael J Ford, and Piotr Piecuch. Photoluminescence, photophysics, and photochemistry of the v b- defect in hexagonal boron nitride. *Physical Review B*, 102(14):144105, 2020.

[135] A Sajid and Kristian S Thygesen. VNCB defect as source of single photon emission from hexagonal boron nitride. *2D Materials*, 7(3):031007, jun 2020.

[136] Viktor Ivády, Gergely Barcza, Gergő Thiering, Song Li, Hanen Hamdi, Jyh-Pin Chou, Örs Legeza, and Adam Gali. Ab initio theory of the negatively charged boron vacancy qubit in hexagonal boron nitride. *npj Computational Materials*, 6(1):1–6, 2020.

[137] Andreas Dietrich, M Bürk, Elena S Steiger, Lukas Antoniuk, Trong Toan Tran, Minh Nguyen, Igor Aharonovich, Fedor Jelezko, and Alexander Kubanek. Observation of fourier transform limited lines in hexagonal boron nitride. *Physical Review B*, 98(8):081414, 2018.

[138] Sejeong Kim, Johannes E Fröch, Joe Christian, Marcus Straw, James Bishop, Daniel Totonjian, Kenji Watanabe, Takashi Taniguchi, Milos Toth, and Igor Aharonovich. Photonic crystal cavities from hexagonal boron nitride. *Nature communications*, 9(1):1–8, 2018.

[139] Frédéric Peyskens, Chitraleema Chakraborty, Muhammad Muneeb, Dries Van Thourhout, and Dirk Englund. Integration of single photon emitters in 2d layered materials with a silicon nitride photonic chip. *Nature communications*, 10(1):1–7, 2019.

[140] Tobias Vogl, Yuerui Lu, and Ping Koy Lam. Room temperature single photon source using fiber-integrated hexagonal boron nitride. *Journal of Physics D: Applied Physics*, 50(29):295101, 2017.

[141] Andreas W Schell, Mikael Svedendahl, and Romain Quidant. Quantum emitters in hexagonal boron nitride have spectrally tunable quantum efficiency. *Advanced materials*, 30(14):1704237, 2018.

[142] Toan Trong Tran, Mehran Kianinia, Minh Nguyen, Sejeong Kim, Zai-Quan Xu, Alexander Kubanek, Milos Toth, and Igor Aharonovich. Resonant excitation of quantum emitters in hexagonal boron nitride. *ACS Photonics*, 5(2):295–300, 2018.

[143] Alexander Szameit and Stefan Nolte. Discrete optics in femtosecond-laser-written photonic structures. *Journal of Physics B: Atomic, Molecular and Optical Physics*, 43(16):163001, 2010.

[144] Alexander Szameit, Felix Dreisow, Thomas Pertsch, Stefan Nolte, and Andreas Tünnermann. Control of directional evanescent coupling in fs laser written waveguides. *Optics express*, 15(4):1579–1587, 2007.

[145] Konstantinos Poulios, Robert Keil, Daniel Fry, Jasmin DA Meinecke, Jonathan CF Matthews, Alberto Politi, Mirko Lobino, Markus Gräfe, Matthias Heinrich, Stefan Nolte, et al. Quantum walks of correlated photon pairs in two-dimensional waveguide arrays. *Physical review letters*, 112(14):143604, 2014.

[146] L Bassham, A Rukhin, J Soto, J Nechvatal, M Smid, E Barker, Stefan Leigh, Mark Levenson, Mark Vangel, David Banks, Alan Heckert, James Dray, and San Vo. A statistical test suite for the validation of cryptographic random number generators. Technical report, National Institute of Standards and Technology, 2010. `https://nvlpubs.nist.gov/nistpubs/Legacy/SP/nistspecialpublication800-22r1a.pdf`.

[147] Steven K. Ang. randomness_testsuite. GitHub (2018) [retrieved 3 March 2019], `https://github.com/stevenang/randomness_testsuite`.

[148] F Klauck, Lucas Teuber, Marco Ornigotti, Matthias Heinrich, Stefan Scheel, and Alexander Szameit. Observation of pt-symmetric quantum interference. *Nature Photonics*, pages 1–5, 2019.

[149] Xiaogang Qiang, Xiaoqi Zhou, Jianwei Wang, Callum M Wilkes, Thomas Loke, Sean O'Gara, Laurent Kling, Graham D Marshall, Raffaele Santagati, Timothy C Ralph, et al. Large-scale silicon quantum photonics implementing arbitrary two-qubit processing. *Nature photonics*, 12(9):534–539, 2018.

[150] Tobias Vogl. *Next-generation single-photon sources using two-dimensional hexagonal boron nitride*. PhD thesis, The Australian National University, 2019.

[151] Mehran Kianinia, Carlo Bradac, Bernd Sontheimer, Fan Wang, Toan Trong Tran, Minh Nguyen, Sejeong Kim, Zai-Quan Xu, Dayong Jin, Andreas W Schell, et al. All-optical control and super-resolution imaging of quantum emitters in layered materials. *Nature communications*, 9(1):1–8, 2018.

[152] Disheng Chen, Zhao Mu, Yu Zhou, Johannes E Fröch, Abdullah Rasmit, Carole Diederichs, Nikolay Zheludev, Igor Aharonovich, and Wei-bo Gao. Optical gating of resonance fluorescence from a single germanium vacancy color center in diamond. *Physical review letters*, 123(3):033602, 2019.

[153] Yongliang Chen, Chi Li, Tieshan Yang, Evgeny A. Ekimov, Carlo Bradac, Son Tung Ha, Milos Toth, Igor Aharonovich, and Toan Trong Tran. Real-time ratiometric optical nanoscale thermometry. *ACS Nano*, 2023. PMID: 36661346.

[154] Andreas Gottscholl, Mehran Kianinia, Victor Soltamov, Sergei Orlinskii, Georgy Mamin, Carlo Bradac, Christian Kasper, Klaus Krambrock, Andreas Sperlich, Milos Toth, Igor Aharonovich, and Vladimir Dyakonov. Initialization and read-out of intrinsic spin defects in a van der Waals crystal at room temperature. *Nature Materials*, 19(5):540–545, 5 2020.

[155] Mehdi Abdi, Jyh-Pin Chou, Adam Gali, and Martin B Plenio. Color centers in hexagonal boron nitride monolayers: a group theory and ab initio analysis. *ACS Photonics*, 5(5):1967–1976, 2018.

[156] Ruffin E Evans, Mihir K Bhaskar, Denis D Sukachev, Christian T Nguyen, Alp Sipahigil, Michael J Burek, Bartholomeus Machielse, Grace H Zhang, Alexander S Zibrov, Edward Bielejec, et al. Photon-mediated interactions between quantum emitters in a diamond nanocavity. *Science*, 362(6415):662–665, 2018.

[157] Marina Radulaski, Matthias Widmann, Matthias Niethammer, Jingyuan Linda Zhang, Sang-Yun Lee, Torsten Rendler, Konstantinos G Lagoudakis, Nguyen Tien Son, Erik Janzen, Takeshi Ohshima, et al. Scalable quantum photonics with single color centers in silicon carbide. *Nano letters*, 17(3):1782–1786, 2017.

[158] AM Dibos, Mouktik Raha, CM Phenicie, and Jeffrey Douglas Thompson. Atomic source of single photons in the telecom band. *Physical review letters*, 120(24):243601, 2018.

[159] Tian Zhong, Jonathan M Kindem, Evan Miyazono, and Andrei Faraon. Nanophotonic coherent light–matter interfaces based on rare-earth-doped crystals. *Nature communications*, 6(1):1–6, 2015.

[160] CT Nguyen, DD Sukachev, MK Bhaskar, Bartholomeus Machielse, DS Levonian, EN Knall, Pavel Stroganov, Ralf Riedinger, Hongkun Park, M Lončar, et al. Quantum network nodes based on diamond qubits with an efficient nanophotonic interface. *Physical review letters*, 123(18):183602, 2019.

[161] Milos Toth and Igor Aharonovich. Single photon sources in atomically thin materials. *Annual review of physical chemistry*, 70:123–142, 2019.

[162] J Klein, M Lorke, M Florian, F Sigger, L Sigl, S Rey, J Wierzbowski, J Cerne, K Müller, E Mitterreiter, et al. Site-selectively generated photon emitters in monolayer mos2 via local helium ion irradiation. *Nature communications*, 10(1):1–8, 2019.

[163] Carlos Errando-Herranz, Eva Schöll, Raphaël Picard, Micaela Laini, Samuel Gyger, Ali W Elshaari, Art Branny, Ulrika Wennberg, Sebastien Barbat, Thibaut Renaud, et al. Resonance fluorescence from waveguide-coupled, strain-localized, two-dimensional quantum emitters. *ACS photonics*, 8(4):1069–1076, 2021.

[164] Toan Trong Tran, Kerem Bray, Michael J. Ford, Milos Toth, and Igor Aharonovich. Quantum emission from hexagonal boron nitride monolayers. *Nature Nanotechnology*, 11(1):37–41, 1 2016.

[165] Annemarie L. Exarhos, David A. Hopper, Richard R. Grote, Audrius Alkauskas, and Lee C. Bassett. Optical Signatures of Quantum Emitters in Suspended Hexagonal Boron Nitride. *ACS Nano*, 11(3):3328–3336, 3 2017.

[166] Nicholas V Proscia, Zav Shotan, Harishankar Jayakumar, Prithvi Reddy, Charles Cohen, Michael Dollar, Audrius Alkauskas, Marcus Doherty, Carlos A Meriles, and Vinod M Menon. Near-deterministic activation of room-temperature quantum emitters in hexagonal boron nitride. *Optica*, 5(9):1128–1134, 2018.

[167] Nicholas R Jungwirth and Gregory D Fuchs. Optical Absorption and Emission Mechanisms of Single Defects in Hexagonal Boron Nitride. *Physical Review Letters*, 119(5):057401, 7 2017.

[168] Matthew A Feldman, Alex Puretzky, Lucas Lindsay, Ethan Tucker, Dayrl P Briggs, Philip G Evans, Richard F Haglund, and Benjamin J Lawrie. Phonon-induced multicolor correlations in hbn single-photon emitters. *Physical Review B*, 99(2):020101, 2019.

[169] Jean Comtet, Evgenii Glushkov, Vytautas Navikas, Jiandong Feng, Vitaliy Babenko, Stephan Hofmann, Kenji Watanabe, Takashi Taniguchi, and Aleksandra Radenovic. Wide-field spectral super-resolution mapping of optically active defects in hexagonal boron nitride. *Nano letters*, 19(4):2516–2523, 2019.

[170] Prince Khatri, Andrew J Ramsay, Ralph Nicholas Edward Malein, Harold MH Chong, and Isaac J Luxmoore. Optical gating of photoluminescence from color centers in hexagonal boron nitride. *Nano letters*, 20(6):4256–4263, 2020.

[171] Mads K Boll, Ilya P Radko, Alexander Huck, and Ulrik L Andersen. Photophysics of quantum emitters in hexagonal boron-nitride nano-flakes. *Optics Express*, 28(5):7475–7487, 2020.

[172] Niko Nikolay, Noah Mendelson, Nikola Sadzak, Florian Böhm, Toan Trong Tran, Bernd Sontheimer, Igor Aharonovich, and Oliver Benson. Very Large and Reversible Stark-Shift Tuning of Single Emitters in Layered Hexagonal Boron Nitride. *Physical Review Applied*, 11(4):041001, 4 2019.

[173] Gichang Noh, Daebok Choi, Jin-Hun Kim, Dong-Gil Im, Yoon-Ho Kim, Hosung Seo, and Jieun Lee. Stark Tuning of Single-Photon Emitters in Hexagonal Boron Nitride. *Nano Letters*, 18(8):4710–4715, 8 2018.

[174] Toan Trong Tran, Mehran Kianinia, Minh Nguyen, Sejeong Kim, Zai-Quan Xu, Alexander Kubanek, Milos Toth, and Igor Aharonovich. Resonant Excitation of Quantum Emitters in Hexagonal Boron Nitride. *ACS Photonics*, 5(2):295–300, 2 2018.

[175] Hai-Son Nguyen, Gregory Sallen, Christophe Voisin, Ph Roussignol, Carole Diederichs, and Guillaume Cassabois. Optically gated resonant emission of single quantum dots. *Physical review letters*, 108(5):057401, 2012.

[176] Jack Hansom, Carsten HH Schulte, Clemens Matthiesen, Megan J Stanley, and Mete Atatüre. Frequency stabilization of the zero-phonon line of a quantum dot via phonon-assisted active feedback. *Applied Physics Letters*, 105(17):172107, 2014.

[177] P Siyushev, H Pinto, M Vörös, A Gali, Fedor Jelezko, and J Wrachtrup. Optically controlled switching of the charge state of a single nitrogen-vacancy center in diamond at cryogenic temperatures. *Physical review letters*, 110(16):167402, 2013.

[178] V M Acosta, C Santori, A Faraon, Z Huang, K.-M. C. Fu, A Stacey, D A Simpson, K Ganesan, S Tomljenovic-Hanic, A D Greentree, S Prawer, and R G Beausoleil. Dynamic Stabilization of the Optical Resonances of Single Nitrogen-Vacancy Centers in Diamond. *Physical Review Letters*, 108(20):206401, 5 2012.

[179] Bernd Sontheimer, Merle Braun, Niko Nikolay, Nikola Sadzak, Igor Aharonovich, and Oliver Benson. Photodynamics of quantum emitters in hexagonal boron nitride revealed by low-temperature spectroscopy. *Physical Review B*, 96(12):121202, 2017.

[180] Oliver Neitzke, Anthony Morfa, Janik Wolters, Andreas W Schell, Günter Kewes, and Oliver Benson. Investigation of line width narrowing and spectral jumps of single stable defect centers in zno at cryogenic temperature. *Nano letters*, 15(5):3024–3029, 2015.

[181] Janik Wolters, Nikola Sadzak, Andreas W Schell, Tim Schröder, and Oliver Benson. Measurement of the ultrafast spectral diffusion of the optical transition of nitrogen vacancy centers in nano-size diamond using correlation interferometry. *Physical review letters*, 110(2):027401, 2013.

[182] Christopher P. Anderson, Alexandre Bourassa, Kevin C. Miao, Gary Wolfowicz, Peter J. Mintun, Alexander L. Crook, Hiroshi Abe, Jawad Ul Hassan, Nguyen T. Son, Takeshi Ohshima, and David D. Awschalom. Electrical and optical control of single spins integrated in scalable semiconductor devices. *Science*, 366(6470):1225–1230, 12 2019.

[183] Lucio Robledo, Hannes Bernien, Ilse Van Weperen, and Ronald Hanson. Control and coherence of the optical transition of single nitrogen vacancy centers in diamond. *Physical review letters*, 105(17):177403, 2010.

[184] Disheng Chen, Johannes E Fröch, Shihao Ru, Hongbing Cai, Naizhou Wang, Giorgio Adamo, John Scott, Fuli Li, Nikolay Zheludev, Igor Aharonovich, et al. Quantum interference of resonance fluorescence from germanium-vacancy color centers in diamond. *Nano Letters*, 2022.

[185] Ali W. Elshaari, Wolfram Pernice, Kartik Srinivasan, Oliver Benson, and Val Zwiller. Hybrid integrated quantum photonic circuits. *Nature Photonics*, 14(5):285–298, 5 2020.

[186] Mete Atatüre, Dirk Englund, Nick Vamivakas, Sang-Yun Lee, and Joerg Wrachtrup. Material platforms for spin-based photonic quantum technologies. *Nature Reviews Materials*, 3(5):38–51, 5 2018.

[187] Chi Li, Noah Mendelson, Ritika Ritika, YongLiang Chen, Zai-Quan Xu, Milos Toth, and Igor Aharonovich. Scalable and deterministic fabrication of quantum emitter arrays from hexagonal boron nitride. *Nano Letters*, 21(8):3626–3632, 2021.

[188] Matthew A Feldman, Claire E Marvinney, Alexander A Puretzky, and Benjamin J Lawrie. Evidence of photochromism in a hexagonal boron nitride single-photon emitter. *Optica*, 8(1):1–5, 2021.

[189] S Alex Breitweiser, Annemarie L Exarhos, Raj N Patel, Jennifer Saouaf, Benjamin Porat, David A Hopper, and Lee C Bassett. Efficient optical quantification of heterogeneous emitter ensembles. *ACS Photonics*, 7(1):288–295, 2019.

[190] Joshua Ziegler, Rachael Klaiss, Andrew Blaikie, David Miller, Viva R Horowitz, and Benjamín J Alemán. Deterministic quantum emitter formation in hexagonal boron nitride via controlled edge creation. *Nano letters*, 19(3):2121–2127, 2019.

[191] Fariah Hayee, Leo Yu, Jingyuan Linda Zhang, Christopher J Ciccarino, Minh Nguyen, Ann F Marshall, Igor Aharonovich, Jelena Vučković, Prineha Narang, Tony F Heinz, et al. Revealing multiple classes of stable quantum emitters in hexagonal boron nitride with correlated optical and electron microscopy. *Nature materials*, 19(5):534–539, 2020.

[192] Cesar Jara, Tomas Rauch, Silvana Botti, Miguel A.L. Marques, Ariel Norambuena, Raul Coto, J. E. Castellanos-Aguila, Jeronimo R. Maze, and Francisco Munoz. First-principles identification of single photon emitters based on carbon clusters in hexagonal boron nitride. *Journal of Physical Chemistry A*, 125(6):1325–1335, 2 2021.

[193] Nathan Chejanovsky, Amlan Mukherjee, Jianpei Geng, Yu-Chen Chen, Youngwook Kim, Andrej Denisenko, Amit Finkler, Takashi Taniguchi, Kenji Watanabe, Durga Bhaktavatsala Rao Dasari, Philipp Auburger, Adam Gali, Jurgen H. Smet, and Jörg Wrachtrup. Single-spin resonance in a van der Waals embedded paramagnetic defect. *Nature Materials*, 20(8):1079–1084, 8 2021.

[194] Hannah L Stern, Qiushi Gu, John Jarman, Simone Eizagirre Barker, Noah Mendelson, Dipankar Chugh, Sam Schott, Hoe H Tan, Henning Sirringhaus, Igor Aharonovich, et al. Room-temperature optically detected magnetic resonance of single defects in hexagonal boron nitride. *Nature communications*, 13(1):1–9, 2022.

[195] Jin Liu, Rongbin Su, Yuming Wei, Beimeng Yao, Saimon Filipe Covre da Silva, Ying Yu, Jake Iles-Smith, Kartik Srinivasan, Armando Rastelli, Juntao Li, et al. A solid-state source of strongly entangled photon pairs with high brightness and indistinguishability. *Nature nanotechnology*, 14(6):586–593, 2019.

[196] Xing Ding, Yu He, Z-C Duan, Niels Gregersen, M-C Chen, S Unsleber, Sebastian Maier, Christian Schneider, Martin Kamp, Sven Höfling, et al. On-demand single photons with high extraction efficiency and near-unity indistinguishability from a resonantly driven quantum dot in a micropillar. *Physical review letters*, 116(2):020401, 2016.

[197] Stephanie Wehner, David Elkouss, and Ronald Hanson. Quantum internet: A vision for the road ahead. *Science*, 362(6412):eaam9288, 2018.

[198] Chloe Clear, Ross C Schofield, Kyle D Major, Jake Iles-Smith, Alex S Clark, and Dara PS McCutcheon. Phonon-induced optical dephasing in single organic molecules. *Physical review letters*, 124(15):153602, 2020.

[199] Joanna M Zajac and Sigurdur I Erlingsson. Temperature dependency of resonance fluorescence from inas/gaas quantum dots: Dephasing mechanisms. *Physical Review B*, 94(3):035432, 2016.

[200] Boris Spokoyny, Hendrik Utzat, Hyowon Moon, Gabriele Grosso, Dirk Englund, and Moungi G Bawendi. Effect of Spectral Diffusion on the Coherence Properties of a Single Quantum Emitter in Hexagonal Boron Nitride. *The Journal of Physical Chemistry Letters*, 11(4):1330–1335, 2 2020.

[201] Hamidreza Akbari, Wei-Hsiang Lin, Benjamin Vest, Pankaj K Jha, and Harry A Atwater. Temperature-dependent Spectral Emission of Hexagonal Boron Nitride Quantum Emitters on Conductive and Dielectric Substrates. *Physical Review Applied*, 15(1):014036, 1 2021.

[202] Simon J.U. White, Ngoc My Hanh Duong, Alexander S Solntsev, Je-Hyung Kim, Mehran Kianinia, and Igor Aharonovich. Optical Repumping of Resonantly Excited Quantum Emitters in Hexagonal Boron Nitride. *Physical Review Applied*, 14(4):044017, 10 2020.

[203] Norbert Kalb, Andreas A Reiserer, Peter C Humphreys, Jacob JW Bakermans, Sten J Kamerling, Naomi H Nickerson, Simon C Benjamin, Daniel J Twitchen, Matthew Markham, and Ronald Hanson. Entanglement distillation between solid-state quantum network nodes. *Science*, 356(6341):928–932, 2017.

[204] Lachlan J Rogers, Kay D Jahnke, Tokuyuki Teraji, Luca Marseglia, Christoph Müller, Boris Naydenov, Hardy Schauffert, Christine Kranz, Junichi Isoya, Liam P McGuinness, et al. Multiple intrinsically identical single-photon emitters in the solid state. *Nature communications*, 5(1):1–6, 2014.

[205] Kay D. Jahnke, Alp Sipahigil, Jan M. Binder, Marcus W. Doherty, Mathias Metsch, Lachlan J. Rogers, Neil B. Manson, Mikhail D. Lukin, and Fedor Jelezko. Electron–phonon processes of the silicon-vacancy centre in diamond. *New Journal of Physics*, 17(4):043011, 4 2015.

[206] Meryem Benelajla, Elena Kammann, Bernhard Urbaszek, and Khaled Karrai. Physical origins of extreme cross-polarization extinction in confocal microscopy. *Physical Review X*, 11(2):021007, 2021.

[207] T Müller, I Aharonovich, Z Wang, X Yuan, S Castelletto, S Prawer, and M Atatüre. Phonon-induced dephasing of chromium color centers in diamond. *Physical Review B*, 86(19):195210, 11 2012.

[208] V Hizhnyakov and P Reineker. Optical dephasing in defect-rich crystals. *The Journal of Chemical Physics*, 111(17):8131–8135, 11 1999.

[209] Elke Neu, Christian Hepp, Michael Hauschild, Stefan Gsell, Martin Fischer, Hadwig Sternschulte, Doris Steinmüller-Nethl, Matthias Schreck, and Christoph Becher. Low-temperature investigations of single silicon vacancy colour centres in diamond. *New Journal of Physics*, 15(4):043005, 4 2013.

[210] Carsten Arend, Jonas Nils Becker, Hadwig Sternschulte, Doris Steinmüller-Nethl, and Christoph Becher. Photoluminescence excitation and spectral hole burning spectroscopy of silicon vacancy centers in diamond. *Physical Review B*, 94(4):045203, 7 2016.

[211] V Hizhnyakov, V Boltrushko, H Kaasik, and I Sildos. Strong Jahn–Teller effect in the excited state: Anomalous temperature dependence of the zero-phonon line. *The Journal of Chemical Physics*, 119(12):6290–6295, 9 2003.

[212] S Ates, S M Ulrich, S Reitzenstein, A Löffler, A Forchel, and P Michler. Post-Selected Indistinguishable Photons from the Resonance Fluorescence of a Single Quantum Dot in a Microcavity. *Physical Review Letters*, 103(16):167402, 10 2009.

[213] Sebastien Boissier, Ross C Schofield, Lin Jin, Anna Ovvyan, Salahuddin Nur, Frank HL Koppens, Costanza Toninelli, Wolfram HP Pernice, Kyle D Major, EA Hinds, et al. Coherent characterisation of a single molecule in a photonic black box. *Nature communications*, 12(1):1–8, 2021.

[214] Raphael Proux, Maria Maragkou, Emmanuel Baudin, Christophe Voisin, Philippe Roussignol, and Carole Diederichs. Measuring the photon coalescence time window in the continuous-wave regime for resonantly driven semiconductor quantum dots. *Physical Review Letters*, 114(6):067401, 2015.

[215] Chang-Min Lee, Mustafa Atabey Buyukkaya, Samuel Harper, Shahriar Aghaeimeibodi, Christopher JK Richardson, and Edo Waks. Bright telecom-wavelength single photons based on a tapered nanobeam. *Nano letters*, 21(1):323–329, 2020.

[216] Leo J. McGilly, Alexander Kerelsky, Nathan R. Finney, Konstantin Shapovalov, En-Min Shih, Augusto Ghiotto, Yihang Zeng, Samuel L. Moore, Wenjing Wu, Yusong Bai, Kenji Watanabe, Takashi Taniguchi, Massimiliano Stengel, Lin Zhou, James Hone, Xiaoyang Zhu, Dmitri N. Basov, Cory Dean, Cyrus E. Dreyer, and Abhay N. Pasupathy. Visualization of moiré superlattices. *Nature Nanotechnology*, 15(7):580–584, 7 2020.

[217] Kyle Hwangbo, Qi Zhang, Qianni Jiang, Yong Wang, Jordan Fonseca, Chong Wang, Geoffrey M. Diederich, Daniel R. Gamelin, Di Xiao, Jiun-Haw Chu, Wang Yao, and Xiaodong Xu. Highly anisotropic excitons and multiple phonon bound states in a van der Waals antiferromagnetic insulator. *Nature Nanotechnology*, 16(6):655–660, 6 2021.

[218] A. K. Geim and I. V. Grigorieva. Van der Waals heterostructures. *Nature*, 499(7459):419–425, 7 2013.

[219] Ying Jiang, Shula Chen, Weihao Zheng, Biyuan Zheng, and Anlian Pan. Interlayer exciton formation, relaxation, and transport in TMD van der Waals heterostructures. *Light: Science & Applications*, 10(1):72, 12 2021.

[220] Yuan Cao, Valla Fatemi, Shiang Fang, Kenji Watanabe, Takashi Taniguchi, Efthimios Kaxiras, and Pablo Jarillo-Herrero. Unconventional superconductivity in magic-angle graphene superlattices. *Nature*, 556(7699):43–50, 4 2018.

[221] Alejandro R.P. Montblanch, Dhiren M. Kara, Ioannis Paradisanos, Carola M. Purser, Matthew S. G. Feuer, Evgeny M. Alexeev, Lucio Stefan, Ying Qin, Mark Blei, Gang Wang, Alisson R. Cadore, Pawel Latawiec, Marko Lončar, Sefaattin Tongay, Andrea C. Ferrari, and Mete Atatüre. Confinement of long-lived interlayer excitons in WS2/WSe2 heterostructures. *Communications Physics*, 4(1):119, 12 2021.

[222] H. Baek, M. Brotons-Gisbert, Z. X. Koong, A. Campbell, M. Rambach, K. Watanabe, T. Taniguchi, and B. D. Gerardot. Highly energy-tunable quantum light from moiré-trapped excitons. *Science Advances*, 6(37), 9 2020.

[223] Lei Wang, En-Min Shih, Augusto Ghiotto, Lede Xian, Daniel A. Rhodes, Cheng Tan, Martin Claassen, Dante M. Kennes, Yusong Bai, Bumho Kim, Kenji Watanabe, Takashi Taniguchi, Xiaoyang Zhu, James Hone, Angel Rubio, Abhay N. Pasupathy, and Cory R. Dean. Correlated electronic phases in twisted bilayer transition metal dichalcogenides. *Nature Materials*, 19(8):861–866, 8 2020.

[224] Jianye Fu, Meng Qiu, Wenzhong Bao, and Han Zhang. Frontiers in Electronic and Optoelectronic Devices Based on 2D Materials. *Advanced Electronic Materials*, 7(7):2100444, 7 2021.

[225] Nils Lundt, Sebastian Klembt, Evgeniia Cherotchenko, Simon Betzold, Oliver Iff, Anton V. Nalitov, Martin Klaas, Christof P. Dietrich, Alexey V. Kavokin, Sven Höfling, and Christian Schneider. Room-temperature Tamm-plasmon exciton-polaritons with a WSe2 monolayer. *Nature Communications*, 7(1):13328, 12 2016.

[226] Jie Gu, Biswanath Chakraborty, Mandeep Khatoniar, and Vinod M. Menon. A room-temperature polariton light-emitting diode based on monolayer WS2. *Nature Nanotechnology*, 14(11):1024–1028, 11 2019.

[227] Liuyang Sun, Chun-Yuan Wang, Alex Krasnok, Junho Choi, Jinwei Shi, Juan Sebastian Gomez-Diaz, André Zepeda, Shangjr Gwo, Chih-Kang Shih, Andrea Alù, and Xiaoqin Li. Separation of valley excitons in a MoS2 monolayer using a subwavelength asymmetric groove array. *Nature Photonics*, 13(3):180–184, 3 2019.

[228] Kyle L. Seyler, Pasqual Rivera, Hongyi Yu, Nathan P. Wilson, Essance L. Ray, David G. Mandrus, Jiaqiang Yan, Wang Yao, and Xiaodong Xu. Signatures of moiré-trapped valley excitons in MoSe2/WSe2 heterobilayers. *Nature 2019 567:7746*, 567(7746):66–70, 2 2019.

[229] James Callum Stewart, Ye Fan, John S. H. Danial, Alexander Goetz, Adarsh S. Prasad, Oliver J. Burton, Jack A. Alexander-Webber, Steven F. Lee, Sarah M. Skoff, Vitaliy Babenko, and Stephan Hofmann. Quantum Emitter Localization in Layer-Engineered Hexagonal Boron Nitride. *ACS Nano*, 15(8):13591–13603, 8 2021.

[230] Clarisse Fournier, Alexandre Plaud, Sébastien Roux, Aurélie Pierret, Michael Rosticher, Kenji Watanabe, Takashi Taniguchi, Stéphanie Buil, Xavier Quélin, Julien Barjon, Jean-Pierre Hermier, and Aymeric Delteil. Position-controlled quantum emitters with reproducible emission wavelength in hexagonal boron nitride. *Nature Communications*, 12(1):3779, 12 2021.

[231] N. Mizuochi, T. Makino, H. Kato, D. Takeuchi, M. Ogura, H. Okushi, M. Nothaft, P. Neumann, A. Gali, F. Jelezko, J. Wrachtrup, and S. Yamasaki. Electrically driven single-photon source at room temperature in diamond. *Nature Photonics*, 6(5):299–303, 5 2012.

[232] A. Lohrmann, N. Iwamoto, Z. Bodrog, S. Castelletto, T. Ohshima, T.J. Karle, A. Gali, S. Prawer, J.C. McCallum, and B.C. Johnson. Single-photon emitting diode in silicon carbide. *Nature Communications*, 6(1):7783, 11 2015.

[233] Bernhard Grotz, moritz V Hauf, Markus Dankerl, Boris Naydenov, Sébastien Pezzagna, Jan Meijer, Fedor Jelezko, Jörg Wrachtrup, Martin Stutzmann, Friedemann Reinhard, and Jose A Garrido. Charge state manipulation of qubits in diamond. *Nature Communications*, 3(1):729, 1 2012.

[234] Matthias Widmann, Matthias Niethammer, Dmitry Yu Fedyanin, Igor A. Khramtsov, Torsten Rendler, Ian D. Booker, Jawad Ul Hassan, Naoya Morioka, Yu-Chen Chen, Ivan G. Ivanov, Nguyen Tien Son, Takeshi Ohshima, Michel Bockstedte, Adam Gali, Cristian Bonato, Sang-Yun Lee, and Jörg Wrachtrup. Electrical Charge State Manipulation of Single Silicon Vacancies in a Silicon Carbide Quantum Optoelectronic Device. *Nano Letters*, 19(10):7173–7180, 10 2019.

[235] Andreas Brenneis, Louis Gaudreau, Max Seifert, Helmut Karl, Martin S. Brandt, Hans Huebl, Jose A. Garrido, Frank H. L. Koppens, and Alexander W. Holleitner. Ultrafast electronic readout of diamond nitrogen–vacancy centres coupled to graphene. *Nature Nanotechnology*, 10(2):135–139, 2 2015.

[236] Jiang-Bin Wu, Miao-Ling Lin, Xin Cong, He-Nan Liu, and Ping-Heng Tan. Raman spectroscopy of graphene-based materials and its applications in related devices. *Chemical Society Reviews*, 47(5):1822–1873, 3 2018.

[237] Hong Kyw Choi, Jaesung Park, Nojoon Myoung, Ho-Jong Kim, Jin Sik Choi, Young Kyu Choi, Chi-Young Chanyong Hwang, Jin Tae Kim, Serin Park, Yoonsik Yi, Soo Kyung Chang, Hee Chul Park, Chi-Young Chanyong Hwang, Choon-Gi Choi, and Young-Jun Yu. Gas molecule sensing of van der Waals tunnel field effect transistors. *Nanoscale*, 9(47):18644–18650, 12 2017.

[238] Zai-Quan Xu, Noah Mendelson, John A Scott, Chi Li, Irfan H Abidi, Hongwei Liu, Zhengtang Luo, Igor Aharonovich, and Milos Toth. Charge and energy transfer of quantum emitters in 2d heterostructures. *2D Materials*, 7(3):031001, 2020.

[239] Daniel Cano, Alban Ferrier, Karuppasamy Soundarapandian, Antoine Reserbat-Plantey, Marion Scarafagio, Alexandre Tallaire, Antoine Seyeux, Philippe Marcus, Hugues de Riedmatten, Philippe Goldner, Frank H. L. Koppens, and Klaas-Jan Tielrooij. Fast electrical modulation of strong near-field interactions between erbium emitters and graphene. *Nature Communications*, 11(1):4094, 12 2020.

[240] Y. Doi, T. Makino, H. Kato, D. Takeuchi, M. Ogura, H. Okushi, H. Morishita, T. Tashima, S. Miwa, S. Yamasaki, P. Neumann, J. Wrachtrup, Y. Suzuki, and N. Mizuochi. Deterministic Electrical Charge-State Initialization of Single Nitrogen-Vacancy Center in Diamond. *Physical Review X*, 4(1):011057, 3 2014.

[241] Rusen Yan, Qin Zhang, Wei Li, Irene Calizo, Tian Shen, Curt A Richter, Angela R Hight-Walker, Xuelei Liang, Alan Seabaugh, Debdeep Jena, et al. Determination of graphene work function and graphene-insulator-semiconductor band alignment by internal photoemission spectroscopy. *Applied Physics Letters*, 101(2):022105, 2012.

[242] Philipp Auburger and Adam Gali. Towards ab initio identification of paramagnetic substitutional carbon defects in hexagonal boron nitride acting as quantum bits. *Physical Review B*, 104(7):075410, 8 2021.

[243] Angus Gale, Chi Li, Yongliang Chen, Kenji Watanabe, Takashi Taniguchi, Igor Aharonovich, and Milos Toth. Site-specific fabrication of blue quantum emitters in hexagonal boron nitride. *ACS Photonics*, 9(6):2170–2177, 2022.

[244] Hamidreza Akbari, Souvik Biswas, Pankaj Kumar Jha, Joeson Wong, Benjamin Vest, and Harry A. Atwater. Lifetime-limited and tunable quantum light emission in h-bn via electric field modulation. *Nano Letters*, 22(19):7798–7803, 2022.